Methods and Apparatuses for Producing Ultra-strong Magnetic Fields

(Brian Faircloth)

Note: Apologies for the lack of fancy and beautiful formatting throughout this document. It was meant to be a working document. It is an intermediate draft on the way to filing patents on the technology described herein. It was never meant for public eyes. There are a few typos and errata here and there, but for the most part it is complete and has all the necessary information for understanding the ultra-magnet technology and how it can be used. It contains more detail than the patents themselves and may provide a deeper understanding of the technology.

Cross-reference to related applications

This application is related to U.S. Provisional Patent Application No. 62/162,137, the entire contents of which are incorporated by reference herein.

Background

It is well known that current moving through a wire produces a magnetic field. The magnetic field can be concentrated or shaped by shaping the geometry of the wire. For instance, the wire can be shaped into a coil, a common practice, to help focus and concentrate the field inside the coil, see figure 0.

Powerful resistive magnets are capable of producing fields in the 1 Tesla range, whereas a typical magnetic resonance imaging machine using superconducting super magnets may be on the order of 5-10 Tesla. At the time of this writing, the strongest magnet in the world boasts a field of 45.5 Tesla, a magnet at the National High Magnetic Field Laboratory at Florida State University.

The technology provided herein may produce magnetic fields stronger than the most powerful manmade magnets in existence today without the use of superconductors. This is an important advancement as the need for cryogenic cooling of the superconductors presents a great number of challenges and limitations of conventional strong magnetic field generation.

Such powerful magnetic fields will no doubt open new unconceived branches of new science and engineering applications, such as nuclear fusion, exotic states of matter, atomic and molecular manipulations, plasma physics, propulsion, magnetic imaging, energy storage, energy production, and any number of other applications and fields.

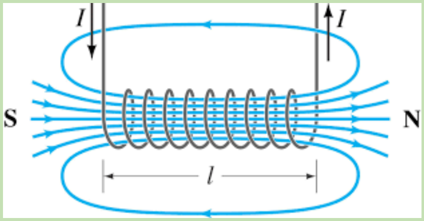

Figure 0

Background

At the most fundamental level, moving charges produce magnetic fields. When an electric field is applied to a conducting wire, electrons move in that wire and those moving electrons produce a measurable magnetic field.

What may be surprising to the layperson is the speed at which those electrons travel in the wire. The net velocity of the electrons in a wire are best measured in mm/min speeds. For instance, a wire with a cross sectional area of 3.0×10^{-6} m^2 (~2 mm diameter) carrying 10 Amps of current has a net electron velocity of 2.5×10^{-4} m/s. Most species of snails move at faster velocities (0.013 – 0.0028 m/s) than the aforementioned electrons.

The present inventor has recognized that if one could maintain very high charge densities, such as those found in the wire, and achieve much higher charge velocities, the effective currents and thus the effective magnetic fields could be increased by many orders of magnitude. The current application provides such techniques to achieve these ultra-strong magnetic fields without the use of superconductors.

Base Concept

The present application provides rotationally symmetric, mechanically dynamic, super-capacitors which collect extreme charge amounts on their electrodes and then rotating those charged electrodes at high angular velocities. Three common rotationally symmetric geometries and the equations of their corresponding capacitance are shown in figure 1 – parallel plate, concentric spheres, and concentric cylinder capacitors.

The capacitors shown do not have dielectrics between the plates as shown, correspondingly in the equations shown ε_0 is the permittivity of free space. In the case of a dielectric being inserted between the plates, ε_0 can be replaced by k ε_0, where k is the dielectric constant of the material in question. This means the capacitance will increase by a factor of k as can be seen from the capacitance equations by replacing ε_0 with k ε_0. Since the charge, Q, is given by Q = C*V, the amount of charge that can be collected on the plates is likewise increased by a factor of k.

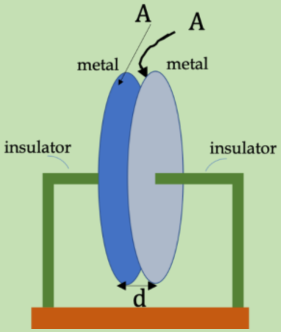

$$C = \frac{\varepsilon_0 A}{d}$$

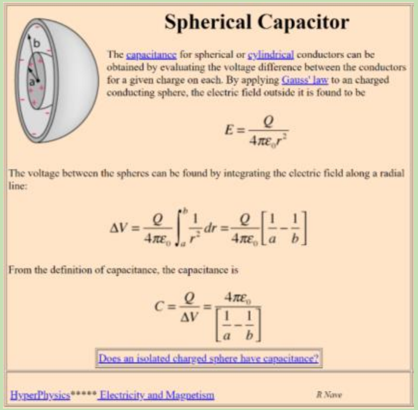

Spherical Capacitor

The capacitance for spherical or cylindrical conductors can be obtained by evaluating the voltage difference between the conductors for a given charge on each. By applying Gauss' law to an charged conducting sphere, the electric field outside it is found to be

$$E = \frac{Q}{4\pi\varepsilon_0 r^2}$$

The voltage between the spheres can be found by integrating the electric field along a radial line:

$$\Delta V = \frac{Q}{4\pi\varepsilon_0}\int_a^b \frac{1}{r^2}dr = \frac{Q}{4\pi\varepsilon_0}\left[\frac{1}{a} - \frac{1}{b}\right]$$

From the definition of capacitance, the capacitance is

$$C = \frac{Q}{\Delta V} = \frac{4\pi\varepsilon_0}{\left[\frac{1}{a} - \frac{1}{b}\right]}$$

Does an isolated charged sphere have capacitance?

HyperPhysics***** Electricity and Magnetism R Nave

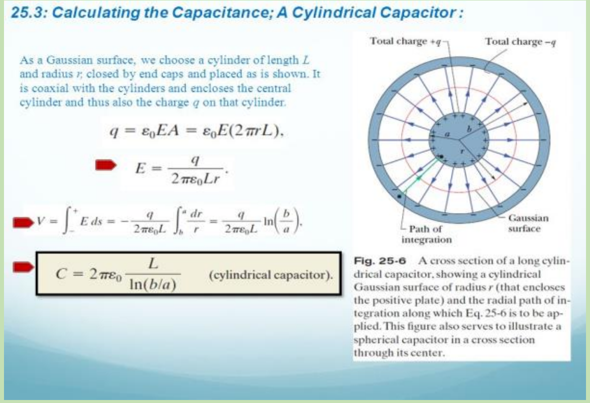

25.3: Calculating the Capacitance; A Cylindrical Capacitor :

As a Gaussian surface, we choose a cylinder of length L and radius r, closed by end caps and placed as is shown. It is coaxial with the cylinders and encloses the central cylinder and thus also the charge q on that cylinder.

$$q = \varepsilon_0 EA = \varepsilon_0 E(2\pi rL),$$

$$E = \frac{q}{2\pi\varepsilon_0 Lr}.$$

$$V = \int_-^+ E\,ds = -\frac{q}{2\pi\varepsilon_0 L}\int_b^a \frac{dr}{r} = \frac{q}{2\pi\varepsilon_0 L}\ln\left(\frac{b}{a}\right).$$

$$\boxed{C = 2\pi\varepsilon_0 \frac{L}{\ln(b/a)} \qquad \text{(cylindrical capacitor).}}$$

Fig. 25-6 A cross section of a long cylindrical capacitor, showing a cylindrical Gaussian surface of radius r (that encloses the positive plate) and the radial path of integration along which Eq. 25-6 is to be applied. This figure also serves to illustrate a spherical capacitor in a cross section through its center.

Figure 1. Capacitances of rotationally symmetric geometries.

Super Dielectrics

Super dielectrics are a very active area of research as the race is on to develop super capacitors to store energy for intermittent power sources such as wind and solar farms and to replace batteries in electric vehicles with cheaper, safer, smaller, and faster charging technology.

A super dielectric is defined as any material with a dielectric constant, k, greater than 10^5 (dielectric constants being a unitless quantity). Currently graphene oxides[1], porous alumina with boric acid or salts[2,3], and electrolytic filled nanotubes[4] are popular choices. At the time of this writing, dielectric constants on the order of 1×10^9 with a 2 V degradation voltage are achievable[2,3,4]. The degradation voltage being important as the charge (Q) a capacitor will accumulate is proportional to both the capacitance (C), which is directly proportional to the dielectric constant, and the voltage (V), $Q = C*V$. While the aforementioned k and V values will be used as representative values in calculations that follow, it is highly likely that these values will be improved in the future as the super capacitor race produces ever better super dielectric materials with improved breakdown voltages and higher dielectric constants.

Analytic Derivation of Magnetic Field Strength

Simple undergraduate physics using Ampere's law will show that the approximate magnetic field (B) at the center of a solenoid (Figure 0) is given by

$$B = \mu_0 n I \qquad (1)$$

where μ_0 is the permeability of free space, *n* is the number of coils per unit length, and *I* is the electrical current. Electrical current is defined as the amount of charge passing a point or area per unit time, *I = dQ/dt* (Coulombs/second in SI units).

A cylindrical shaped supercapacitor with rotating charged plates is analogous to the aforementioned solenoid. In this case, n = 1, since there is only a single distributed coil (i.e., the cylindrical shell plate of the capacitor). The electrical current can be defined as

$$I = Q * RPS \qquad (2)$$

where RPS is the rotations per second of the plates of the rotating cylindrical capacitor. One plate having a charge of +Q and the other plate a charge of –Q. Equation (2) is for a single plate rotating and one plate remaining stationary. If both plates where counter-rotating, a factor of 2 would appear out front.

The equation for the capacitance of a cylindrical capacitor is well known to be (from figure 1)

$$C = 2\pi k \varepsilon_0 \frac{L}{ln\frac{b}{a}} \qquad (3)$$

where *L* is the length of the cylindrical capacitor, *a* is the inner radius (i.e., inner plate location), and *b* is the outer radius (i.e., outer plate location).

With Q = C*V, equation (3) becomes

$$Q = 2\pi k \varepsilon_0 \frac{L*V}{ln\frac{b}{a}} \qquad (4)$$

Putting equation (4) into equation (2), and then substituting equation (2) into equation (1). The magnitude of the magnetic field can be solved

$$\boldsymbol{B = 2\pi k \varepsilon_0 \mu_0 \frac{L*V*RPS}{ln\frac{b}{a}}} \qquad (5)$$

Analytic Derivation of Magnetic Field Strength

As an example, using a k = 1 x 10^9, V = 2 volts, and a geometry of a 10 cm diameter cylindrical capacitor that is 1 meter long and has a dielectric spacing of 10 um between the plates, one calculates a magnetic field strength (B) of 2.30 Tesla. Figure 2 shows how the magnetic field strength varies as a function of the spacing between the plates, i.e., the dielectric gap thickness. A rotational speed of 100,000 rotations per minute (RPM) is used as the angular speed of the rotating cylinder for reference. Turbo-molecular vacuum pumps achieve rotational speeds of this order of magnitude so this angular speed is not unreasonable from an angular velocity standpoint. As can be seen from equation (5), increasing or decreasing the rotational speed will proportionally increase or decrease the strength of the magnetic field.

The cylinder example was worked out analytically because the field strength at the center of a solenoid is a well-known example that is analogous to the rotating cylindrical supercapacitor.

Technically, the Biot-Savart law could be used to calculate the magnetic field for any geometry

$$\vec{B}(r) = \frac{\mu_0}{4\pi} \iiint_V \frac{(\vec{J} dV) \times \vec{r\prime}}{|r\prime|^3} \qquad \text{(5a)} \quad \text{(Biot-Savart Law)}$$

Where *J* is the current density, *dV* is the volume element, and *r'* is the distance vector from *dV* to the point of observation (i.e., the point at which the magnetic field, *B,* is to be calculated) at observational point *r*.

However, as the geometries involved become complex the calculations can become intractable. Therefore, moving forward, finite element analysis (FEA or FEM) will be used to provide exemplary results.

Figure 3 shows the results of the aforementioned supercylinder field problem analyzed using QuickField^{TM} FEA software package. As can be seen, the magnetic field results inside the solenoid (cylinder) agree well with the analytical calculations, showing a 2.30 Tesla field at the center of the rotating cylinder, in agreement with the analytical solution.

Analytic Derivation of Magnetic Field Strength

Figure 2. Magnetic field strength vs dielectric gap thickness for a supercylinder

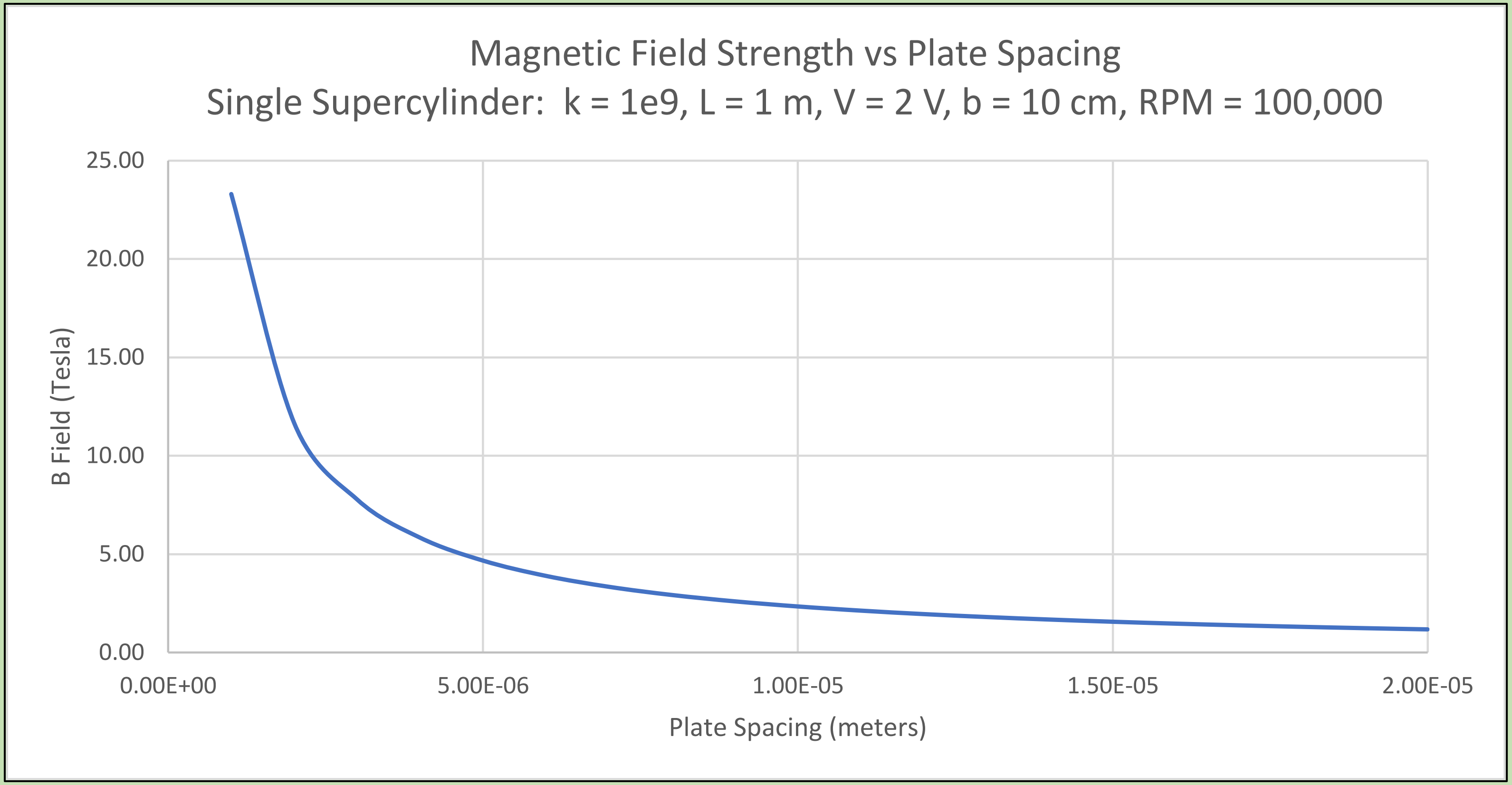

Analytic Derivation of Magnetic Field Strength

Figure 3. FEA model of a 100 cm long by 10 cm diameter supercylinder (10 um dielectric gap, 2 V potential, k = $1\text{x}10^9$, RPM = 100,000). *Figure updated*

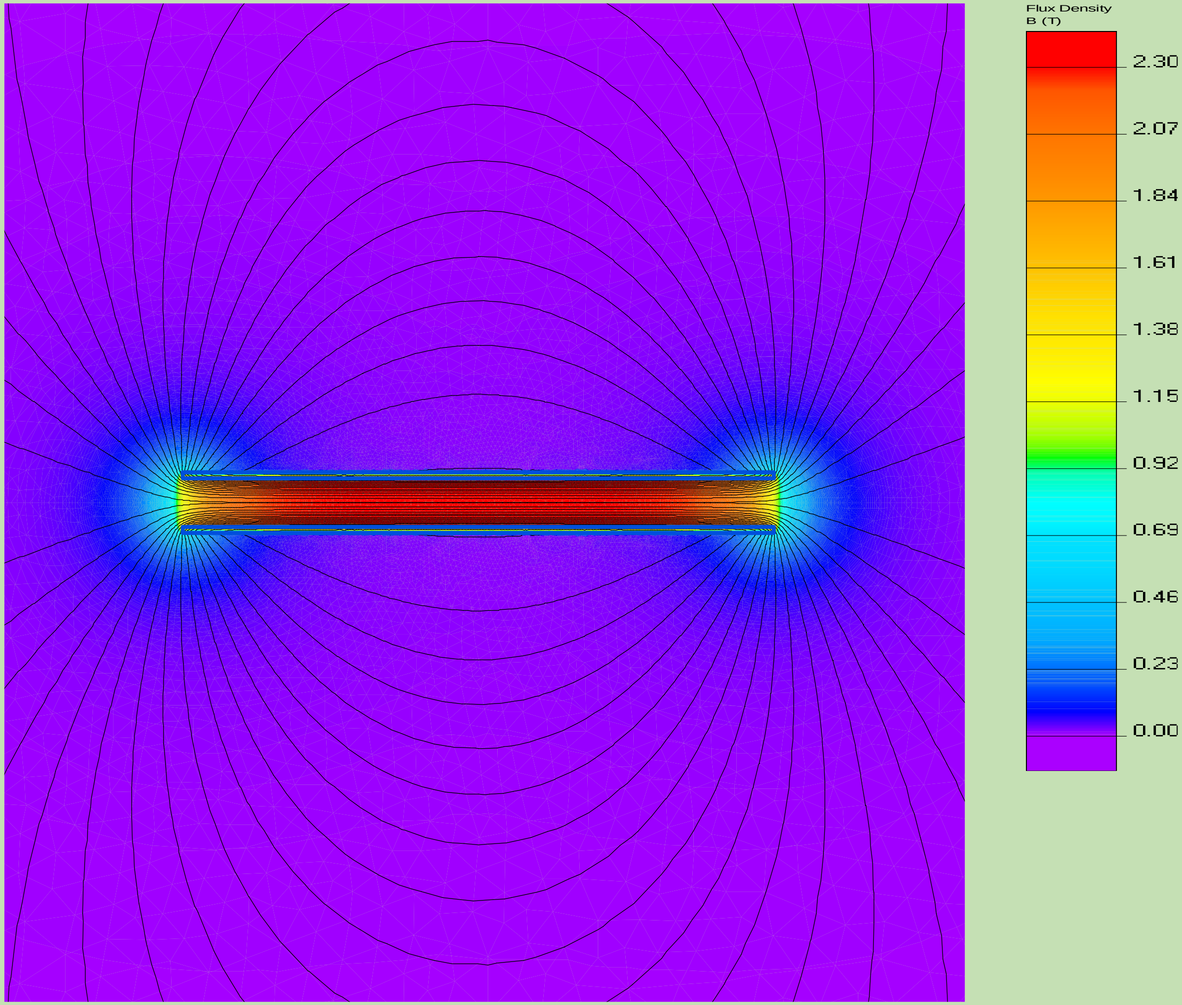

In the preceding calculations and simulation results, it was assumed only one electrode plate of the cylinder is rotating. In some examples, it may be desirable to have both plates rotating in a counter-rotating fashion. If the magnet were attached to a structure that were not affixed to a rigid object (e.g., a ship on the ocean or a spacecraft in flight), this will help balance and control any reactionary torque the structure would experience. Additionally, since one plate is positively charged and the other plate negatively charged, counter rotating the plates can double the amount of effective current used to produce the magnetic field.

The mechanically bearing and rotational assemblies should be non-magnetic (i.e., non-ferrous) and in some examples non-conductive. For instance, bearings, races, shafts, struts, etc. may be or include polymers, glasses, crystals, non-conductive composites, or ceramics with permeabilities as close to unity as practicable. This may reduce unintended forces/flexures due to the strong magnetic fields produced as well as protect against potential eddy currents induced by stray or varying magnetic fields. Exemplary materials will be covered later.

Dielectric Gap

It is well known that to maximize the charge a capacitor holds, the dielectric gap between the plates should be minimized – see the equations for capacitance in figure 1. A higher rotating charge density naturally results in a stronger magnetic field, which is highly desirable in producing an ultra-strong magnetic field, thus the dielectric gap should be as small as possible.

It may be difficult to maintain micron or sub-micron width gaps in capacitors that are large and undergoing rotational forces; trying to hold a one-micron gap between two one-meter diameter plates that are spinning may be difficult.

Some examples of the present devices and methods solve this problem by allowing one of the plates of the capacitor to be non-rigid, preferably a conductive fluid.

Interface

The solution involves applying the super dielectric in the desired thickness to a rigid electrode as shown in Figure 4. The super dielectric is then coated with a thin film of a non-stick insulating substance. The second plate/electrode of the capacitor is then composed of an amount of a liquid conductor preferably capped by a second rigid conductor. The terms electrode and plate may be used interchangeably throughout.

In fluid mechanics it is common practice to assume that the fluid is stationary at the contact point between the fluid and a solid surface, here the non-stick film shown in Figure 4 and the conductive fluid. This is not a desirable situation as the charge that accumulates on the conductive fluid surface interface may be dragged along with the moving/rotating surface. Having both the positive and negative charges moving in the same direction, i.e. having the same rotational velocity vector, will diminish the effective current, and thus, the strength of the magnetic field. To mitigate this, it is important that the charged fluid surface 'slip' and does not stick to the rotating assembly (solid electrode, super dielectric, optional non-stick film).

An illustrative example of the materials involved would be platinum (or a platinum coated material) for the conductors; mercury (the preferred embodiment of the conductive fluid) is reactive and is known to react/form amalgams with a large number of metals, so it is important to choose a conductor that is in contact with the mercury that is non-reactive with the mercury, such as platinum though other metals or conductors are possible. A further illustrative example would include electrolyte or salt filled nanotubes for the super dielectric since the length of the nanotubes can be precisely controlled, polytetrafluoroethylene (PTFE) for the non-stick layer since PTFE is a common sputter target and can be deposited in very thin (10's to 100's of nm) and precise thicknesses using sputtering or vapor deposition. Finally, liquid mercury is used as the conductive fluid to form the slip joint. Liquid mercury has high surface tension (i.e. cohesion) which makes it ideal for not adhering to the PTFE or other materials. Liquid mercury also has low viscosity which makes it ideal for minimizing drag while the plate(s) are in motion. Additionally, mercury is a metal, which gives it good conductivity and charge density limits. And mercury is liquid at room temperature. It should be noted that while this is an example embodiment, there are other materials and combinations of materials that may render similar results and are encompassed within the present methods and devices. For instance, any metal or conductive alloy can be heated to its melting point and form a conductive fluid. Additionally, liquids with high conductivities that are not metallic could be used. Doped mercury should not be excluded as a possibility as mercury's physical or electrical properties may be enhanced with dopants or additives, however, pure mercury will be used as the exemplary example. Mercury is a cheap, convenient, readily available material with desirable properties, thus, is the preferred embodiment described herein.

While the shown embodiment includes a non-stick thin film, it should be understood that in the present devices and methods, the absence of a non-stick film is also a possibility and may be preferred. This is especially the case when the matrix material of the super-dielectric is a low adhesion material itself, such as is the case with a number of ceramics (e.g., doped alumina [12], doped zirconia [12], Tungsten Disulfide [13]), and most metal oxides, metal chlorides, metal fluorides, metal sulphides, and metal nitrides. This list should not be considered exhaustive as there are a wide choice of low adhesion/stick materials which are suitable for the matrix material of the super-dielectric as well as the non-stick film. To wit, Tungsten Disulfide has a coefficient of friction of 0.03-0.09 [13] while polytetrafluoroethylene (PTFE), the de facto standard of low adhesion materials, has a coefficient of friction of 0.05-0.10 [14]. There are a great number of other materials and formulations within the families mentioned that possess similar or better low-adhesion properties.

Interface continued

Another alternative for producing the rotating slip joint is to have the fluid between the plates (electrodes) as shown in Figure 5a. The super-dielectric material itself may be the fluid. Or a layer of fluid, preferably a super-dielectric fluid, may be inserted into the gaps between the plates/electrodes in addition to a solid or semi-solid super-dielectric.

This method has the advantage that the moving charges are affixed to the solid plates (electrodes), thus, there is no concern the charges will be dragged along with the conducting fluid as aforementioned. The charges in the dielectric itself are composed of electric dipoles which have net zero electric charge and do not contribute on the macroscale to the magnetic field. This method has the disadvantage that it is desirable to have the gap between the plates (electrodes) to be as small as possible, to get the highest capacitance and hence charge density possible. Very small gaps may present tolerancing problems during manufacture as well as challenges with flexing and distortion of the system under dynamic motion/rotation, especially when the system in question may be large (i.e. d <<< D where d is the gap between electrodes and D is the order of the size of the electrodes such as radius of the cylinders in a cylindrical supercapacitor or the radius of the plates in a circular parallel plate supercapacitor or the radius of the spheres in a spherical supercapacitor). A small amount of flexure/strain could damage the dielectric layer by causing the plates (electrodes) to come into contact while in motion or exert destructive forces on the interface layer assembly. These are some of the reasons for introduction of the conductive slip joint fluid previously mentioned, i.e. mercury, however the fluid concepts of figure 5a should not be ruled out and are included as part of the scope of the present devices and methods. It is possible to meet these kind of tolerancing numbers, especially when the devices in question may be smaller.

At the time of this writing a super-dielectric fluid is not believed to exist, however, it is likely a super-dielectric fluid could be engineered for this purpose.

If the thin fluid layer between the super-dielectric and the electrode is not a super-dielectric fluid, the fluid should be chosen to minimize friction as much as possible while being electrically and chemically inert, with the super-dielectric fluid aforementioned being the exception. If the fluid is not a super-dielectric fluid, Perfluoropolyether fluids (PFPE Oils) and silicone oils are good choices due to their lubricating and non-reactive properties, however, any number of fluids with desirable lubrication and inertness properties are possible.

Interface

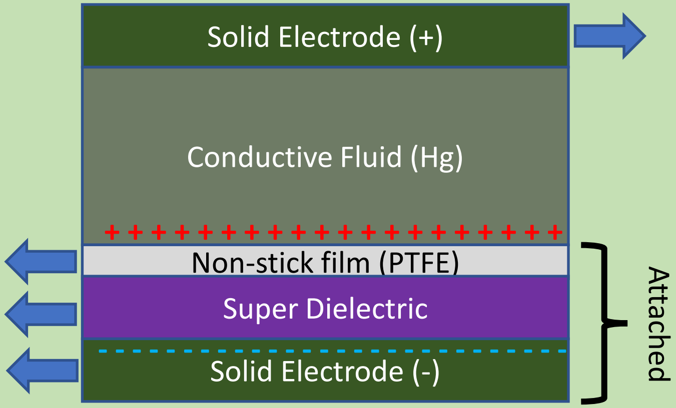

Figure 4. Schematic of interface geometry. Slip joint is one of the electrodes.

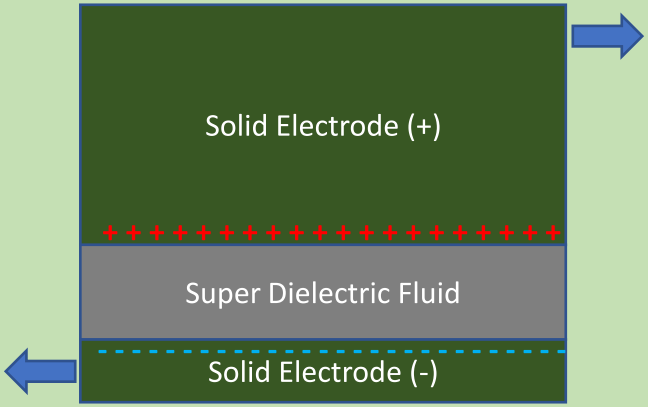

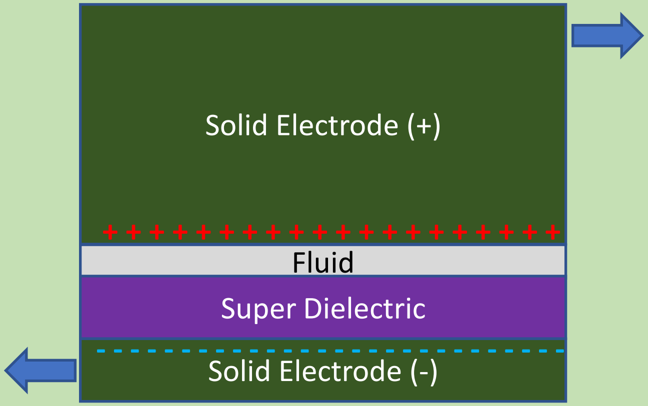

Figure 5a. Schematic of interface geometry. Slip joint is fluid between electrodes.

Interface continued

It may be advantageous for each electrode to have individual super-dielectric layers as shown in Figure 5b.

As shown, both the positive electrode and the negative electrode receive a super-dielectric layer that is in contact with a grounded conductive slip joint fluid. In the single super-dielectric electrode case, the maximum voltage that can be applied between the electrodes is two volts, in the current example. With both electrodes coated with super-dielectric, the voltage potential between the two electrodes is essentially doubled; 2 V between the positive electrode and the grounded conductive slip-joint fluid, and 2 V between the negative electrode and the grounded slip-joint fluid, thus a 4 V potential between the two oppositely polarized electrode plates.

Referring to the design in figure 4, in the best case, the charge that builds up in the slip-joint fluid side of the electrode is stationary and does not contribute to the magnetic field. In this single electrode super-dielectric layer situation, only the charges on one of the electrodes contributes to the magnetic field even if the electrodes are counter-rotating. In the dual electrode super-dielectric layer design shown in Figure 5b, both solid, moving, electrodes hold charge, one being positive and one being negative, and contribute equally to the magnetic field; essentially doubling the magnetic field strength compared to the single electrode super-dielectric case from figure 4. It is also worth noting, there is little packing density penalty for adding the second super-dielectric layer as the super-dielectric layer is only microns thick and is negligible compared to the thickness of the electrode itself in most cases.

Additionally, the shear forces created in the counter-rotating charged electrodes also produce opposing shear momentums in the fluid, thus helping further mitigate charge movement in the conductive fluid at the super-dielectric conductive slip-joint fluid interface.

It should be noted that the use of a thin non-super dielectric fluid layer or non-stick film is shown in figure 5a and 5b, and which has been discussed. These inclusions will have a detrimental effect on the charge capacity of the electrodes even when these layers are very thin. Therefore, the preferred embodiment is to produce the super-dielectric matrix material out of a low adhesion, low stick material as previously discussed to which many ceramics and materials mentioned previously naturally possess, and to forgo the use of the fluid and/or non-stick layers except under extreme circumstances such as extending the life of the device under high rotational speeds. While figures 4, 5a, and 5b show these fluid (non-super dielectric fluid case) and non-slip layers, they are optional layers and not generally preferred.

Interface continued

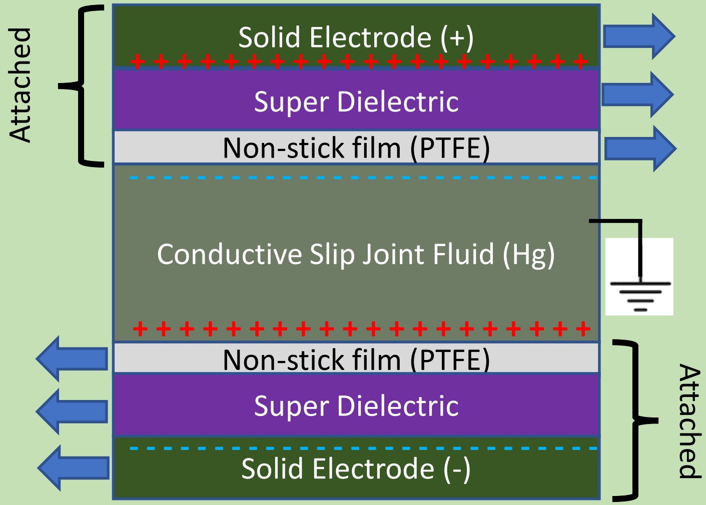

Figure 5b. Schematic of interface geometry. Individual electrode super-dielectric layers. Both positive and negative electrodes possesses a super-dielectric coating.

Super-dielectric (SD)

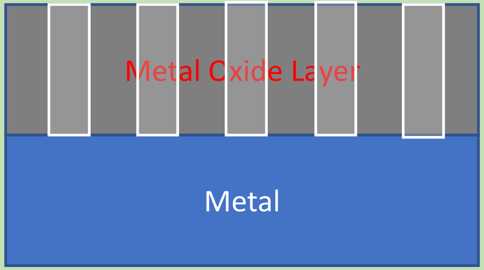

While the present application is not specifically about the super-dielectric (SD) utilized, the super-dielectric (SD) can be useful for creating ultra-strong magnetic fields.

Sufficiently high dielectric materials are in existence at the time of this writing[1-4]; however, it is expected that great strides will continue to be made in this area as the race to high energy density storage devices continues.

While the exemplary example given for the super-dielectric material given is that of Cortes and Phillips, Nano-tube super dielectric materials[4], it would be remiss to not suggest alternatives that do not appear in the current literature.

One manufacturing method that could be employed to produce the super dielectric for the present devices and methods to grow a metal oxide, metal fluoride, metal chloride, metal sulfide, or metal nitride on top of a conductor/metal to be used as one of the electrodes in question. While metal fluorides, chlorides, sulfides, and nitrides are viable materials, metal oxides will only be mentioned primarily for brevity. These oxide layers can be grown and controlled to precise thicknesses, typically 10's of nm, using chemical vapor deposition, thermal evaporation, hydrothermal, and laser ablation[5]. More recently metal oxide nanostructures on metal have been produced using hot water[5].

The metal oxide, as well as the other materials mentioned, is insulating and typically chemically inert. Photolithography, electron beam lithography, or imprint lithography can be used to pattern the oxide as desired, a honeycomb pattern for instance, and the pattern etched into the oxide to a desired depth using plasma etching (e.g., reactive ion etching, inductively coupled plasma etching) or chemical etching, see figure 6. The patterning and etching of semiconductors, conductors, insulators, and oxides on the sub-micron scale is well known to anyone in the art of microchip fabrication or nanotechnology. The patterns can then be filled with salts, acids, bases, or other ionic or electrolytic solutions or materials to produce the super-dielectric in question. In this way the thickness, geometry, composition, and therefore the performance of the super-dielectric layer can be precisely produced and controlled. The porous or patterned material which will host the aforementioned solutions is known as the super-dielectric matrix material throughout this application. Once the acid, base, salt, ionic, or electrolytic solution has been added to the matrix the final product is known as the super-dielectric as it now has a dielectric constant in the super-dielectric range ($k>10^5$).

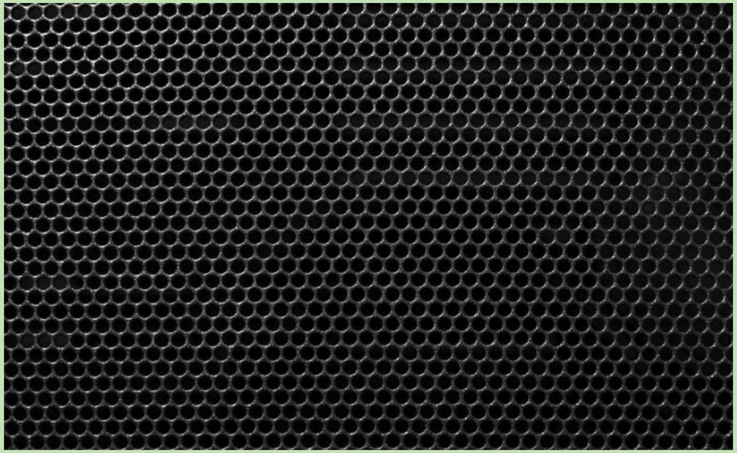

Figure 6. Patterned metal oxide nano-layer for creation of the super-dielectric. *Figure updated*

Multi-electrode Cylindrical Ultra-magnet

Figure 2 and 3 show the results for a super-cylinder magnet with a single contributing electrode. In order to achieve very large magnetic fields, more than a single cylinder (electrode) may be employed. Shown in figure 7 is a conceptual schematic of how this might be accomplished.

In this example, one electrode includes a series of concentric cylindrical shells connected at a common base. The other electrode is of similar design, but is the complement of the first electrode, with some space redacted to accommodate a conducting fluid for the slip joint (mercury being shown here as the conducting fluid) between the two multi-cylindrical shell electrodes and the super-dielectric layer. A positive voltage is applied to one electrode and a negative voltage is applied to the complementary electrode. The conducting fluid between them is held at an intermediate potential, here ground or 0 Volts.

The cylindrical shells of both electrodes are constructed with a thin super dielectric layer as previously discussed. This allows for a large negative charge to build on the negative electrode and a large positive charge to build on the positive electrode. The electrodes are then counter spun to one another at a high rotational speed. The moving charge creates an analogous effective current which in turn produces a powerful magnetic field.

The shells can be manufactured of sufficient thickness and tolerancing to be rigid under rotation, not requiring bearings or spacers. However, if it is desired to have a dense design of shells (i.e. large number of electrode shells per radial distance and thus large volumetric charge), the electrode cylindrical shells may become thin and flex or break due to the centrifugal force of rotation. In this case elements that insure spacing is maintained between the oppositely charged electrode shells can be incorporated, here is shown radial bearings at the end of the negative cylindrical shells. Additional bearings or spacers can be incorporated along the length if loading on the bearings or spacers is a concern or if deformation or sagging would otherwise be an issue along the length of the electrode shell. Rotary seals are shown to keep the mercury contained in the inner cavity; however, these seals are optional if the electrodes assembly is kept inside a static mercury volume itself and the electrodes insulated from the mercury.

Thicker shells can be incorporated periodically or as needed to provide structural support in the cylindrical shell assembly when spacers or bearings are used. Figure 7 shows these thicker shells as the outside shells of the positive electrode and the other shells as uniform in thickness. However, the structural support shells (thicker shells) can be incorporated anywhere and as often as is needed to provide structural support – densely packed thin shells, thick structural shell, densely packed thin shells, thick structural shell, and so on. Additionally, the cylindrical shells do not need to be of uniform thickness throughout the radius. The centrifugal force is weaker the closer to the axis of rotation one gets and stronger the farther away from the axis of rotation one gets – the shells may be thinner, and therefore more densely packed, towards the center and thicker the farther one gets from the center of rotation. To state it a different way, the cylindrical shells require less structural support closer to the axis of rotation and more structural support the farther one goes from the center of rotation due to the centrifugal forces involved, $F_{cent} = m\omega^2 r$, where *m* is a mass at distance from center, *r,* rotating at an angular velocity of ω.

Multi-electrode Cylindrical Ultra-magnet

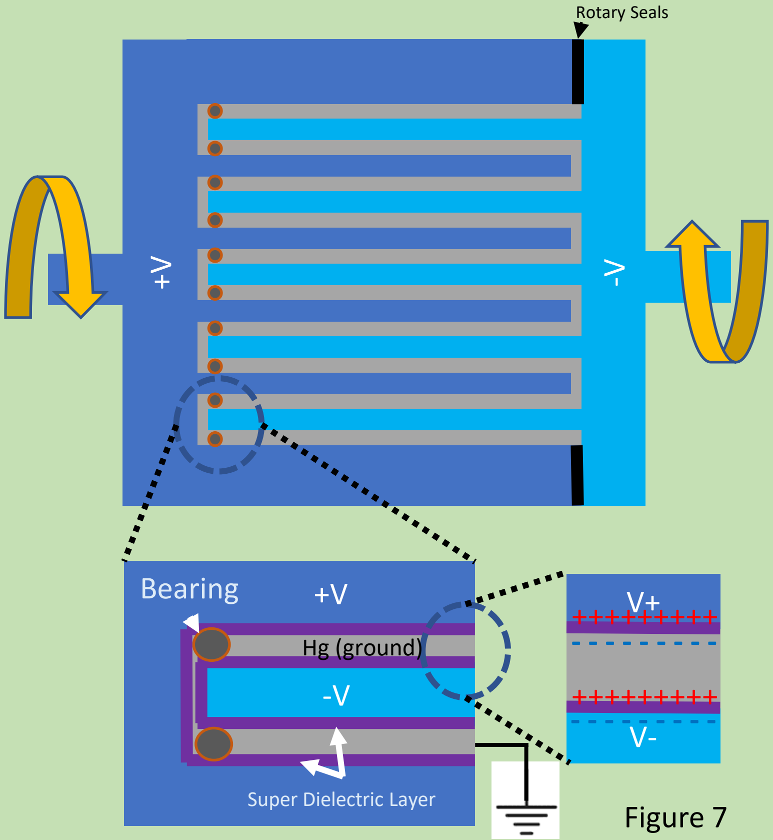

Figure 7

Multi-electrode Cylindrical Ultra-magnet

While it is previously shown in the blown-up section of figure 7 that, if bearings are included, the bearings are in contact with the super dielectric, the super dielectric is likely to be thin and may wear quickly.

As an alternative, the bearing contact surfaces can be made of a hard non-conductive material such as composites or ceramics as shown in the zoomed in section of figure 8.

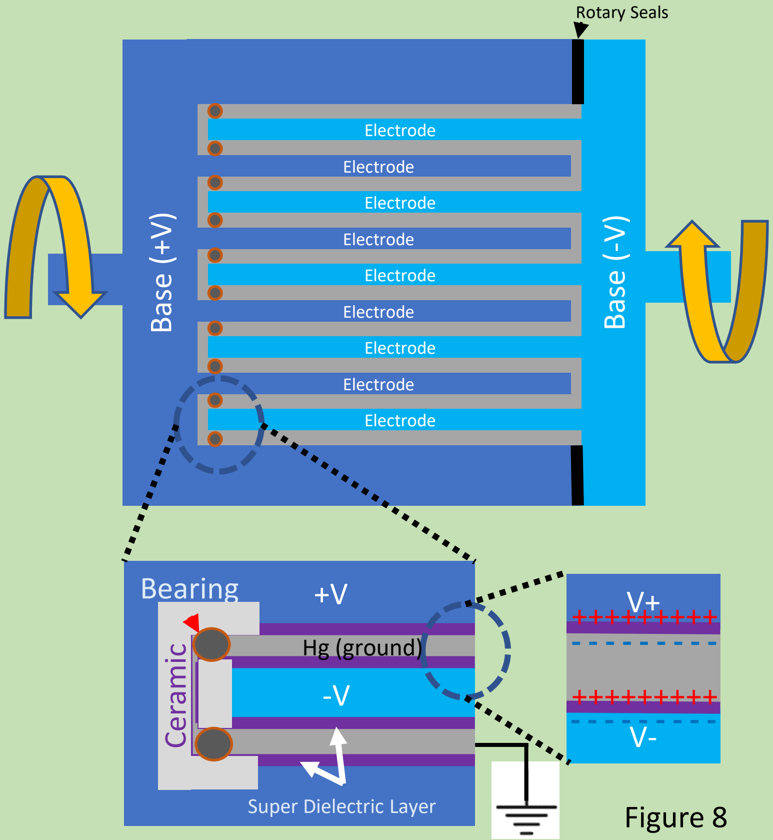

Figure 8

Multi-electrode Cylindrical Ultra-magnet

As a further alternative, for strength and weight considerations, the electrodes themselves can be made of strong, lightweight, non-conductive materials, such as composites, glass, plastics, crystals, or ceramics, with Silicon Carbide (SiC) ceramic being an exemplary example, figure 9. A thin metal film can be deposited on the SiC electrodes through a number of means, such as sputter coating or thermal or e-beam evaporation for example. The dielectric and metal coating can then be removed in the area of interest through a number of selective etching processes, such as photolithography and acid etching, though any number of other processes are possible. Alternatively, the ceramic can be masked during the metal and dielectric deposition process such that no metal or super dielectric is deposited in those areas during construction.

Figure 9 shows what the thin film configuration would look like on the SiC electrode substrate. A metal layer is deposited onto the SiC substrate. The metal layer can be as thin as 10’s of nanometers or hundreds of microns thick depending on the amount of charge density and electrical conductivity that is desired. The super dielectric (SD) is then deposited or grown (as a metal oxide) on top of the metal layer as previously discussed. A non-stick layer can be deposited on top of the super-dielectric (SD) layer if needed or desired. An insulating material, such as polyacrylate or polycarbonate, is applied with a syringe, or masking and depositing, or silkscreening, to the interface between the multilayer film and the area of the SiC that has been exposed. The insulating material prevents shorting of the charged metal to the conducting slip joint fluid, in this case mercury (Hg). It should also be noted that since the metal layer is isolated from the mercury and chemical or metallurgical reactions with the mercury are not a concern, any metal or conductor can be used, such as gold, silver, or copper, for better conductivity and charge density potential. As advances in graphene and high temperature super-conductors are proceeding rapidly, these should not be ruled out as alternatives to metals in this situation.

It should also be noted, while it is possible to manufacture the positive and negative electrode assemblies as monolithic pieces, it is more convenient to manufacture and process the electrodes as separate cylindrical shells that are then attached to the base. This allows easier processing (e.g. masking, coating, etching, etc.) than would be allowed with a monolithic electrode with blind pockets.

Also, as a reminder, exposing the ceramic as a hard bearing surface may be particularly useful if there are bearings or spacers present. If the electrodes are designed and manufactured such that sufficient tolerancing exists for manufacturing, alignment, and flexure during operation, the mercury can take up these tolerances. In this case, no bearings or spacers are needed, therefore, the electrodes can be substantially or fully encapsulated in the multilayer film (metal, SD, optional non-stick film). Again, the inclusion of a non-stick film is not the preferred embodiment but is included for completeness.

Multi-electrode Cylindrical Ultra-magnet

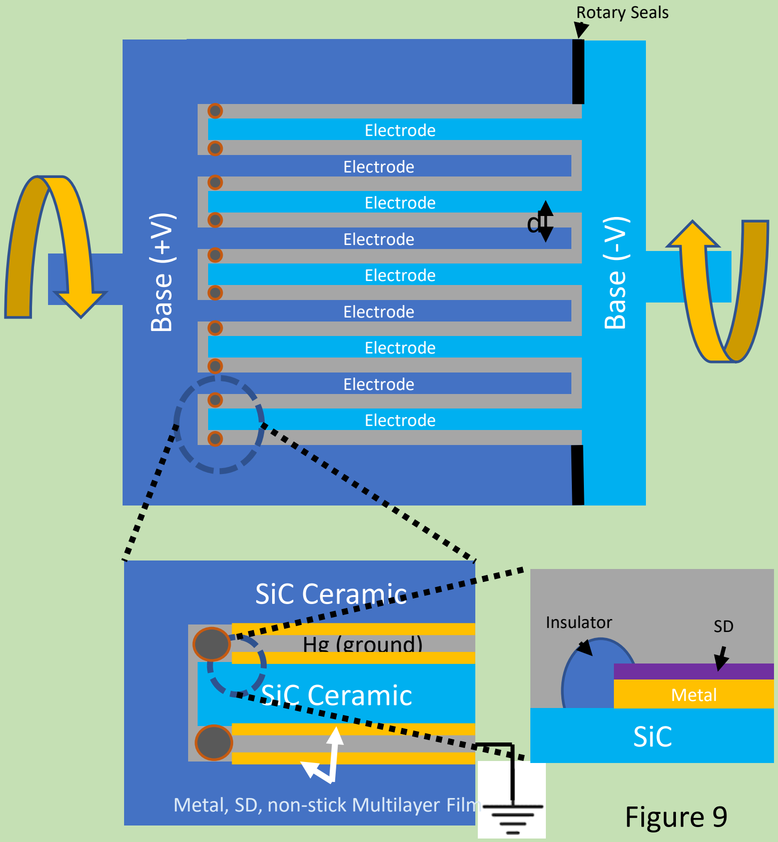

Figure 9

Multi-electrode Cylinder Ultra-magnet (MCU) Performance

With the dynamic cylinder super-capacitor geometry discussed, massive charges can build within the device. When these charges are set into motion, they can produce extremely strong magnetic fields.

Finite Element Analysis with QuickField^{TM} was used to simulate the strength of the magnetic fields of the described Multi-electrode Cylindrical Ultra-Magnet from figures 7-9 , hereafter known as the MCU, design for a number of design configurations.

Figure 10 shows two configurations, one is a smaller version, 20 cm long, 10 cm in diameter, with electrode spacings of 1.0 mm, where electrode spacing is defined as the distance from the center of one charge polarity electrode to the center of the next oppositely charge polarized electrode (labeled ‘d’ in figure 9). The SD thickness is 5 microns, and the rotation velocity is 100,000 RPM. This version of the MCU can produce magnetic fields of more then 110 Tesla.

The second configuration consists of a large MCU that is two meters long and one meter in diameter with 1.0 cm electrode spacings, and 5 microns thick super-dielectric layers, counter-spinning at 100,000 rotations per minute. This configuration can produce a magnetic field in excess of 1100 Tesla at this rotation rate.

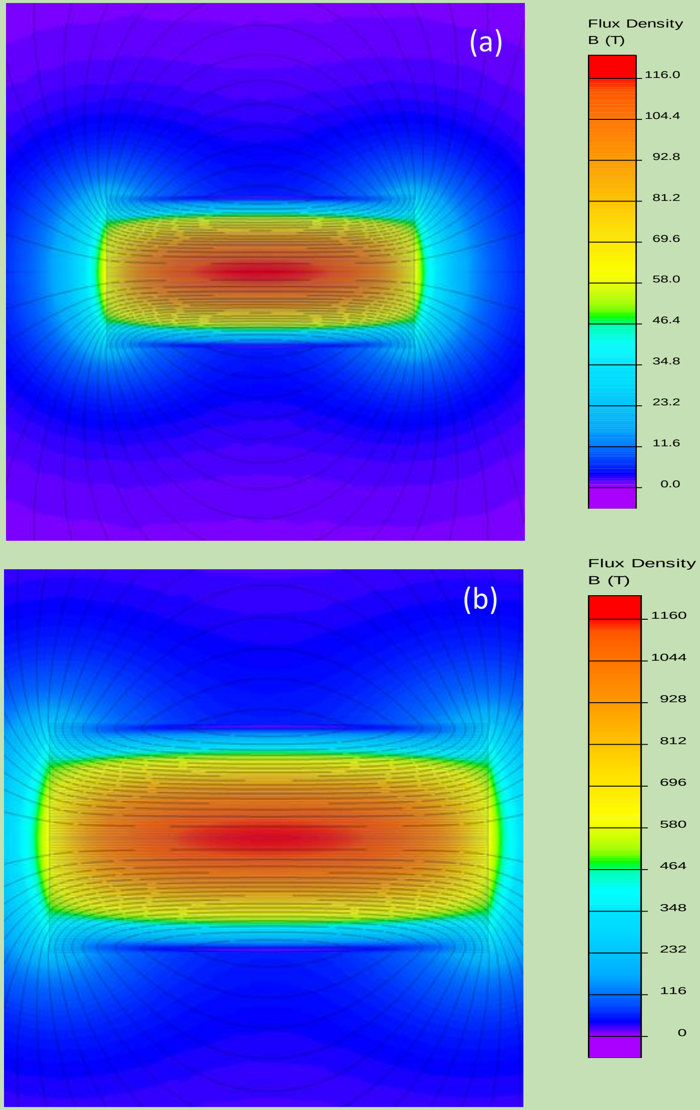

Figure 10. Multi-electrode Cylindrical Ultra-magnet (MCU); (a) Length = 20 cm, Diameter = 10 cm, SD thickness = 5 microns, electrode spacing = 1.0 mm, RPM = 100,000; (b) Length = 2 meters, Diameter = 1 meter, SD thickness = 5 microns, electrode spacings = 1.0 cm, RPM = 100,000. Both cases k = 1x10^{9}, Voltage = 2 V. *Figure updated*

MCU Performance Cont.

As can be seen from equation 5, performance can be improved by improving on a number of factors. A higher dielectric constant will enhance the performance, however, in these analysis, super dielectric constants that can be produced at this writing will be used, to wit $k = 1 \times 10^9$. The thickness of the dielectric layer can be reduced to improve performance, the rotation speed of the electrodes can be increased to improve performance. And the voltage on the electrodes can be increased to hold more charge, and thus, improve performance. However, the super dielectrics in the exemplary example have a maximum voltage potential of two volts before the super dielectric experiences a degradation in performance, therefore, 2 volts is used throughout. Another performance improvement is to pack as many electrodes as is practical into a given space, to maximize the volumetric charge. This means small spacings between the electrodes in the radial direction is desirable.

Figure 11 shows the performance of a small MCU, 20 cm long by 10 cm in diameter, with a number of different electrode spacings and dielectric thicknesses simulated. Here the effect of these two parameters on the peak magnetic field achievable can be seen, where the peak occurs at the center point of the device (i.e., at the origin). Table 1 lists the corresponding values for reference. Expectedly, a power series provides an excellent fit to the data as can be seen in the one-micron dielectric thickness case in Figure 11.

Even such a small MCU unit possesses the potential to produce peak magnetic fields on the order of tens or hundreds of Tesla.

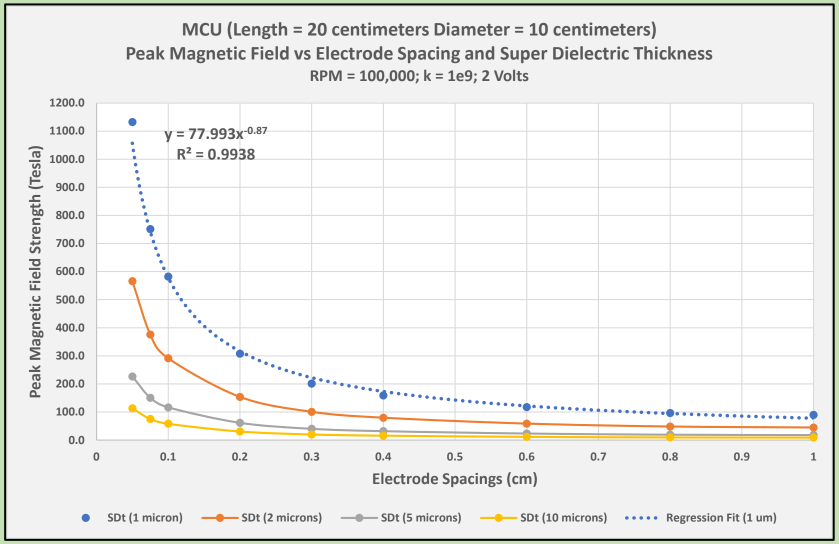

Figure 11. 20 cm x 10 cm MCU peak magnetic fields in Tesla. QuickField^{TM} simulation results.

Electrode Spacing (cm)	SDt (1 micron)	SDt (2 microns)	SDt (5 microns)	SDt (10 microns)
1	89.6	44.8	17.9	9.0
0.8	96.6	48.3	19.3	9.7
0.6	117.4	58.7	23.5	11.7
0.4	159.2	79.6	31.8	15.9
0.3	201.4	100.7	40.3	20.1
0.2	307.6	153.8	61.5	30.8
0.1	582.4	291.2	116.5	58.2
0.075	751.5	375.8	150.3	75.1
0.05	1132.3	566.1	226.4	113.2

Table 1. 20 cm x 10 cm MCU peak magnetic fields in Tesla. QuickField^{TM} simulation results. (SDt = super-dielectric layer thickness).

MCU Performance Cont.

Figure 12, and corresponding Table 2, show the simulated results for a larger MCU; 2.0 meters in length by 1.0 meter in diameter.

In an extreme example, the 2.0 meter x 1.0 meter MCU with a super dielectric layer thickness of one micron and a 1.0 mm electrode spacing reaches a peak magnetic field strength in excess of 50,000 Tesla; this magnetic field is roughly one billion times stronger than that of the Earth's (~30 x 10^{-6} Tesla close to the equator, ~50 x 10^{-6} Tesla at the poles).

While such an extreme example may benefit from highly meticulous engineering to construct and may be complicated to build, it does demonstrate the incredible potential of the technology.

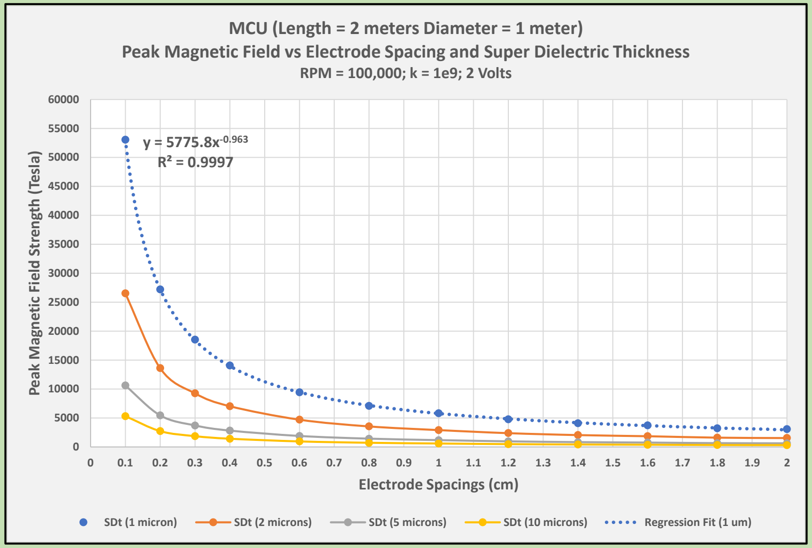

Figure 12. 2 meter x 1 meter MCU peak magnetic fields. QuickField^{TM} simulation results.

Electrode Spacing (cm)	SDt (1 micron)	SDt (2 microns)	SDt (5 microns)	SDt (10 microns)
2	3076	1538	615	308
1.8	3213	1606	643	321
1.6	3708	1854	742	371
1.4	4100	2050	820	410
1.2	4765	2383	953	477
1	5824	2912	1165	582
0.8	7092	3546	1418	709
0.6	9419	4710	1884	942
0.4	14073	7037	2815	1407
0.3	18517	9259	3703	1852
0.2	27210	13608	5442	2720
0.1	53041	26520	10605	5306

Table 2. 2 meter x 1 meter MCU peak magnetic fields in Tesla. QuickField^{TM} simulation results. (SDt = super-dielectric layer thickness).

MCU Construction

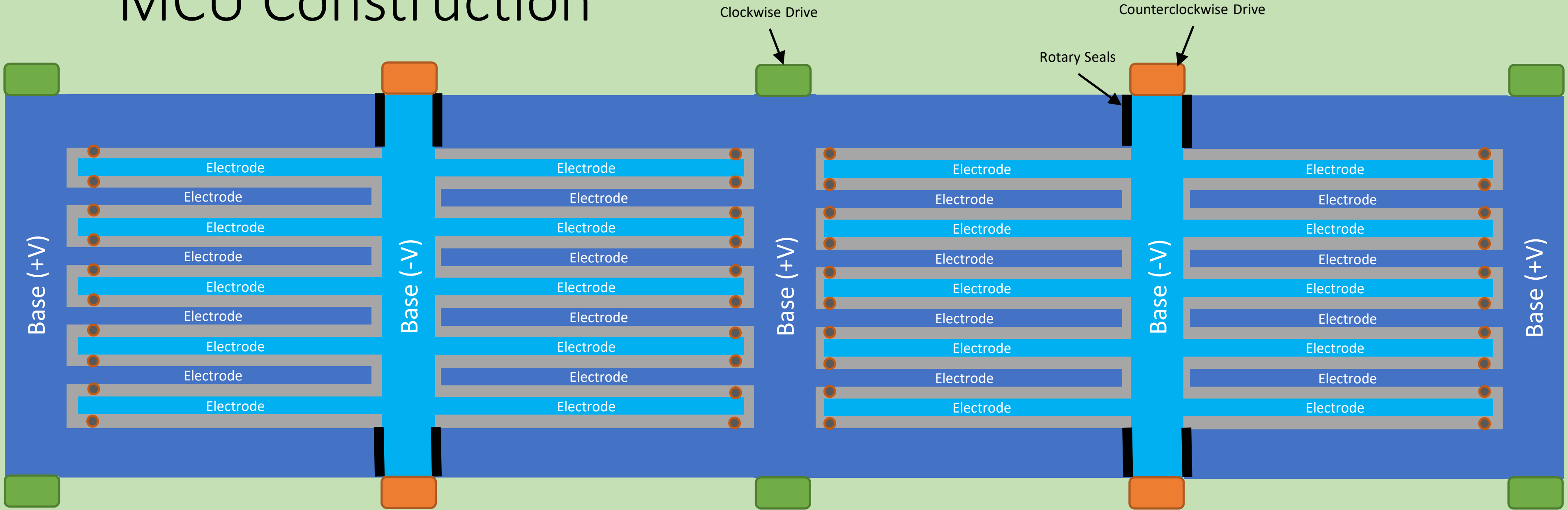

Figure 12a

In order to make construction of long MCU's easier, the long MCU can be assembled from modular, shorter MCUs which can be placed side by side individually or attached and driven by a common driveshaft.

Shown in Figure 12a is one embodiment of a segment of a side-by-side design. In this case, the negative and positive electrodes are counter-rotated by an external mechanism instead of a central driveshaft.

It should be noted that it is not technically essential for both charges of electrodes (positive and negative) to rotate. One charged electrode(s) can be held stationery as the oppositely charged electrode(s) rotate. The advantage to counter-rotating both charges of the electrodes is the magnetic field is essentially doubled. Additionally, opposite torque moments are canceled out. Additionally, the counter rotation keeps opposing shear forces in the slip-joint fluid that helps prevent the conductive slip-joint fluid from sticking to the walls of the SD layered electrodes.

See MUMs designs later for more on connecting devices in series.

Circular Electrode Ultra-magnets

Cylindrical electrodes present some challenges in the construction of an ultra-magnet. Some processes, such as lithography, material deposition, etching, etc. can be more difficult on a curved surface. And, as a general rule, tighter tolerances can be maintained on a flat surface; flatness, wedge, thickness, surface quality, etc..

To this end, it is desirable to use flat, circular electrodes as opposed to cylindrical shell electrodes as previously described, see figure 13.

The basic design incorporates similar elements of the MCU. Counter-rotating electrodes are employed with a super-dielectric film as outlined previously. The electrodes can be made of metal, composites, or ceramics as covered earlier with the MCU and all of the design elements covered under the MCU should be included by inference.

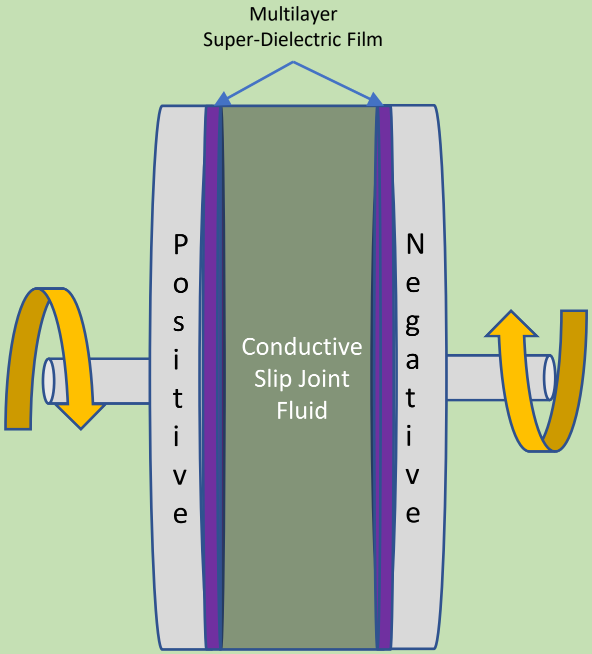

Figure 13. Base Circular Electrode Ultra-magnet design schematic concept.

Circular Electrode Ultra-magnets

It is well known that the capacitance between two closely spaced circular disc is approximately C = kϵ_0A/d, where k is the dielectric constant of the material between the two discs, ϵ_0 is the permittivity of free space, A is the area of a disc, and d is the separation between the two discs. The charge contained on each disc is simply Q = CV, where Q is the total charge, C is the capacitance, and V is the voltage between the two discs. In this way, the surface charge density, σ, is easily computed, σ = Q/A, where A is the area of one of the discs, A = πR^2.

Using the Biot-Savart Law (also see equation 5a for the integral form),

$$d\vec{B} = \frac{d\vec{J}\times\hat{r}}{4\pi\mu r^2} \qquad (6),$$

where $d\vec{J}$ is an infinitesimal current volume element, $\hat{r}$ is the unit vector pointing from the current element to the point of evaluation of the field, μ is the permeability of the material the field exists in, and r^2 is the distance from the current element to the point of evaluation. Understanding that charges in motion represent current, the magnetic field, $\vec{B}$, can be calculated at any point in space. It can be shown that the magnetic field along the axis of rotation at a distance of z from a rotating uniformly charged disc, figure 14, is

$$B_z(z) = \frac{\mu\sigma\omega}{2}\left(\frac{R^2+2z^2}{\sqrt{R^2+z^2}} - 2z\right) \qquad (7),$$

where B_z is the magnetic field component along the axis of rotation, and ω is the angular velocity of the disc in radians per second.

Using equation (7), calculating the B field at z = 10 cm from a 1-meter diameter disc rotating at 100,000 rpm, holding a charge of 1000 Coulombs, and assuming free space as the medium, one calculates a B field of 2.76 Tesla. Running an axisymmetric finite element model of the charged disc set up, again with the rotational axis of symmetry being the horizontal axis, produces a result of B(z = 10 cm) of 2.79 Tesla (figure 15), in reasonable agreement with the analytical calculation.

While analytical calculations are feasible for simple geometries, analytical calculations for complex geometries become intractable and computer simulation is required. As with the MCU, Finite Element Analysis (FEA or FEM) will be used hereafter for the spinning disc geometries discussed.

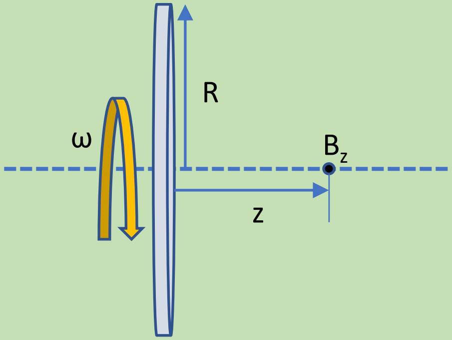

Figure 14. Rotating charged disc.

Circular Electrode Ultra-magnets

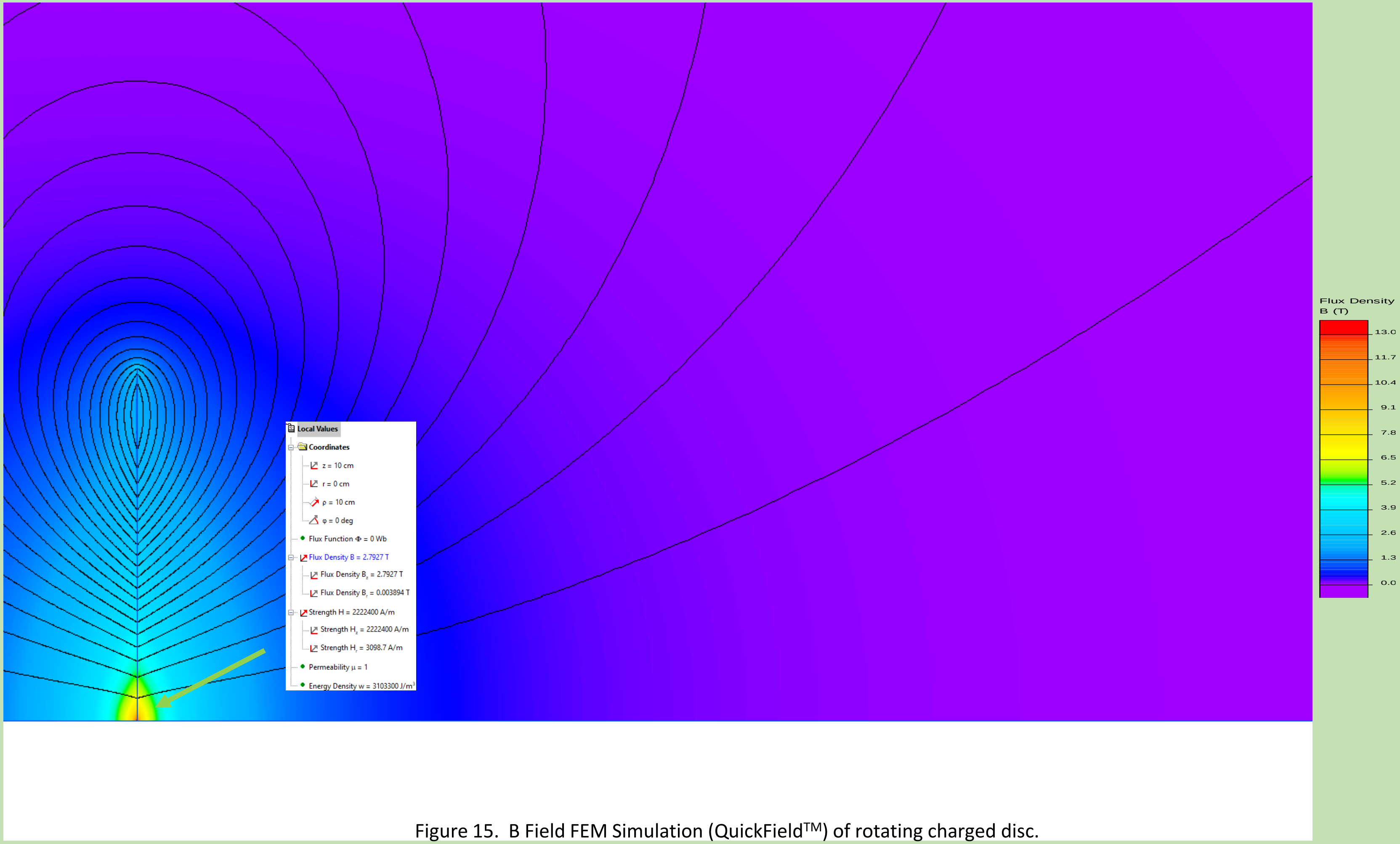

- z = 10 cm
- r = 0 cm
- ρ = 10 cm
- φ = 0 deg
- Flux Function Φ = 0 Wb
- Flux Density B = 2.7927 T
  - Flux Density B_z = 2.7927 T
  - Flux Density B_r = 0.003894 T
- Strength H = 2222400 A/m
  - Strength H_z = 2222400 A/m
  - Strength H_r = 3098.7 A/m
- Permeability μ = 1
- Energy Density w = 3103300 J/m^3

Figure 15. B Field FEM Simulation (QuickField^{TM}) of rotating charged disc.
Charge = 1000 Coulombs; RPM = 100,000; Diameter = 1-meter.
Rotationally symmetric around the horizontal axis.

Multi-Disc Ultra-Magnets

As with the cylindrical ultra-magnets, the rotating disc ultra-magnet can be greatly enhanced by increasing the number of rotating discs in an assembly.

All the electrode/super-dielectric interface methods and geometries described previously apply to the rotating disc electrode geometries as well and are included herein by inference.

The preferred embodiment is the dual super-dielectric interface layer, i.e., each charge of electrode possessing its own super-dielectric layer on both sides of the disc electrode, multi-layer film implied if the design calls for it.

As with the MCUs, the electrodes/discs may be constructed from a number of materials including metal or one of the strong, lightweight, materials stated earlier; composites, glass, plastics, crystals, ceramics, etc..

Multi-disc Ultra-magnets shall afterwards be referenced as MDUs.

Figure 16 shows one embodiment of the design. N disc electrodes are encapsulated in the slip-joint conductive fluid. A central driveshaft connects all of the discs and provides the rotational drive to the discs. The discs are held at one potential and the conductive slip-joint fluid is held at another potential, thus, allowing the needed charge to build on the surface of the discs. The voltage can be easily supplied to the discs through the central driveshaft. The discs themselves are coated with a super-dielectric layer or multi-layer as the case may be, see earlier discussion regarding MCU's and Interface. This allows charge to build-up on both sides of the disc. If the discs have sufficient thickness and it is desired, the edges of the discs may likewise be coated with super-dielectric to further enhance the magnetic field strength. Note, in the simulations that follow, this edge charge is not considered, only the charges on the top and bottom surfaces of the discs are considered. The outside casing is only structural and does not contribute to the magnetic field in this embodiment. Rotary bearings are shown, however, in rotation, only a tensile stress is experienced along the plane of the disc due to the centrifugal forces of rotation. The discs are unlikely to strain in the radial direction sufficiently to cause issue; there is no off-axis flexure moment due to centrifugal forces unlike the MCU case. The rotary bearings may be needed if the apparatus is not in a vertical position, i.e., driveshaft not aligned to gravity, and the driveshaft experiences some flexure due to gravity, though in general the rotary bearings should not be required.

The advantages to this design include; 1. a single rotary driveshaft is simpler to construct, using fewer rotary seals or bearings that can also be smaller in diameter around the shaft; 2. the discs can be very tightly packed into the assembly. The major disadvantage is, due to there only being one torque moment in the system, the slip joint fluid will experience a shear stress torque that will eventually build an amount of angular momentum in the slip joint fluid. The angular momentum will be such that the charge in the fluid close to the electrode will experience some angular velocity in the same direction as the charged electrode, thus, diminishing the magnetic field somewhat. This effect can be mitigated by counter-rotating the outside casing and providing a counter-acting torque; however, this is not as optimal as having two electrodes of opposite charge in close proximity counter-rotating to one another.

As with the MCU, the rotary seals are not required if it is not a requirement to contain the mercury inside the device, such as device submersion in mercury or recirculating the mercury back into the device as it leaks out.

Multi-Disc Ultra-Magnets

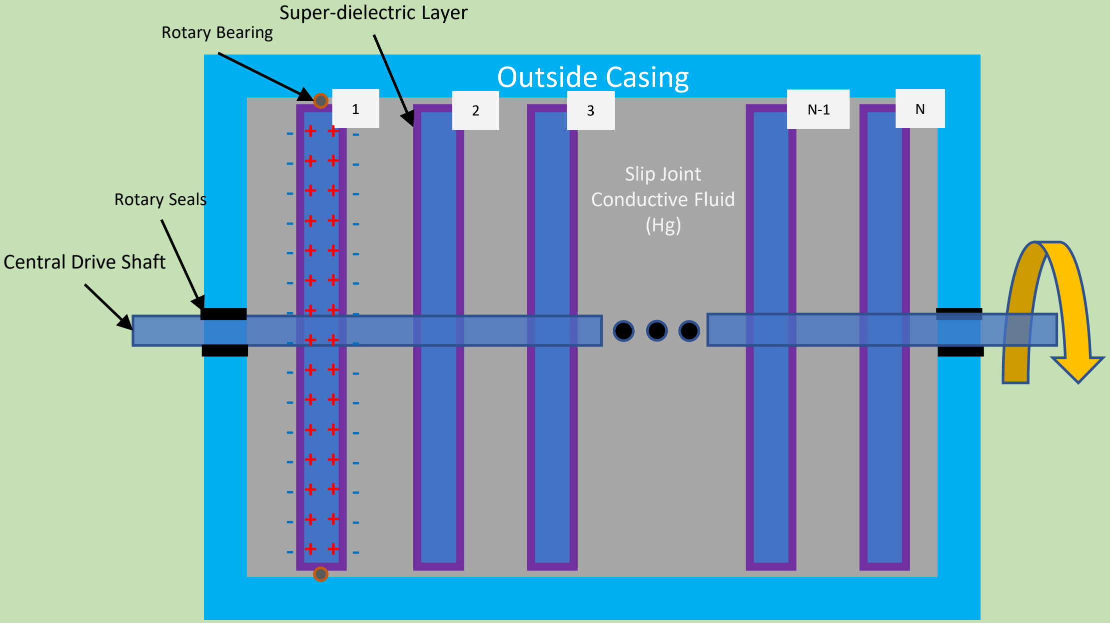

Figure 16. Multi-disc Ultra-magnet (MDU) single central shaft, single charge rotation schematic design. Charge is only shown on first disc for simplicity. Rotary bearing is only shown on first electrode for simplicity as well. Choice of charge polarity is arbitrary (depends on direction of rotation and desired polarity of magnet).

Multi-Disc Ultra-Magnets

Figure 17 shows a schematic diagram of the dual polarity counter-rotating MDU design with N sets of rotating discs. A series of discs is attached to the inner drive shaft which also serves as the electrode to provide voltage potential and charge to those discs. The discs are coated with the super-dielectric layer as described previously. These discs are referred to as the inner discs.

The other polarity discs are attached to a cylindrical body, the outside casing, that also serves as the supply electrode for those discs; to deliver voltage potential and charge. These discs are referred to as the outer discs. These outer discs are also coated with super-dielectric layer as described previously. The cylindrical body is attached to an outer driveshaft. The outer driveshaft is hollow to allow the inner driveshaft to pass through and rotationally drive the inner discs independently of the outer discs. The outer discs have a hole in their center to allow the inner drive shaft to pass through.

A conductive slip joint fluid, in the exemplary example mercury (Hg), encapsulates both inner and outer discs. One electrode is powered to +2 V and the other electrode is powered to -2 V, and the mercury is held at an intermediate potential, here zero volts or ground. This allows charge to build on the inner and outer discs, in figure 17 the outer discs are at positive potential and the inner discs are at negative potential, though this choice is arbitrary. The inner and outer discs are then spun at high angular velocity in opposite directions.

If rotatory bearings are used, the rotary bearing can be placed between the inner shaft and one or more of the outer discs and/or the outer drive shaft (as shown in figure 17). If outer discs are used, these support discs can be modified such as being thicker to provide structural support. Smaller diameter rotary bearings and rotary seals have the advantage of being more conducive to higher rotation speeds, and thus more powerful magnetic fields; as the strength of the magnetic field is directly proportional to the rotation speed of the discs.

Additionally, it should be pointed out, the outside casing/electrode is insulated from the mercury slip-joint fluid as to not electrically short the casing to the slip-joint fluid. This can be done by either depositing a film insulator on the inner diameter of the outside casing, masked where the outer discs attach to the casing; or using a non-conductive, strong, lightweight material (as covered earlier) for the outside casing and selectively applying metal coatings to the areas that need conduction paths, masking those areas that are wetted by the mercury; or metal coating the inside of a non-conductive casing and etching the metal away in the areas that would be wetted by the mercury. It should be noted that, while not shown in the figure, the inner walls of the outside casing electrode can likewise be coated by the super-dielectric layer to act as the separation barrier between the electrode and the slip-joint fluid. This will build up a strong charge on the cylindrical inner diameter (ID) part of the outside electrode which is a rotating member, further enhancing the magnetic field when the apparatus is in rotational motion. Similar insulating processing could be taken with the inner electrode/shaft, although due to its small radius, only a small additional advantage would be gained by coating it with a super-dielectric layer. In the simulation results that follow, it is assumed that neither the ID of the outer cylinder nor the inner drive shaft are charged.

Locally, the mercury holds an equal and opposite charge to the electrodes near to the super-dielectric layer. However, due to the mercury having high surface tension, the super-dielectric matrix being constructed of a low adhesive material and optionally being capped with a non-stick thin film, combined with the two electrodes being counter-rotated which creates opposite, cancelling, shear torques in the fluid, those parasitic charge motions are greatly mitigated. The thinner the mercury fluid (i.e., the closer the inner and outer counter-rotating electrode plates are to one another) the greater the mitigation effect will be. In addition to mitigating parasitic charge motion, having high electrode densities also equates to higher amps/unit volume which result in stronger magnetic fields; a win-win situation.

While Figure 17 shows the shafts extending from both sides of the apparatus, it is possible to have the shafts drive the discs from one side and have the other side of the apparatus closed.

Multi-Disc Ultra-Magnets

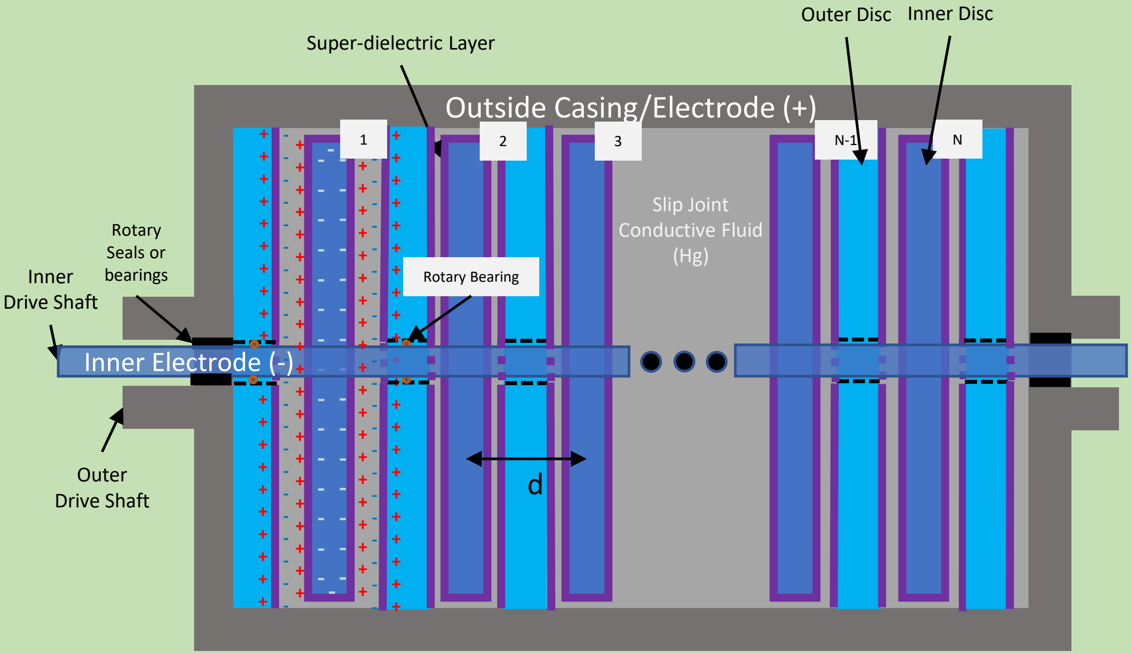

Figure 17. Multi-disc Ultra-magnet (MDU) inner and outer counter-rotating shafts, doubly charged rotation schematic design. Charge is only shown on first disc pair for simplicity. Choice of charge polarity is arbitrary (depends on direction of rotations and desired polarity of magnet).

Multi-Disc Ultra-Magnets

Decades of manufacturing experience teaches us that producing large numbers of a single item results in better quality, tolerancing, and yield; quality engineering tools like statistical process control (SPC) and process optimization can be utilized. To this end, the MDU inner and outer shafts as well as the outside casing can be designed such that the shafts attach in series in a lock and key or interlocking castellations geometry, though any number of mechanical joints can be used. This allows for building a base MDU and then attaching those base MDUs in series to produce a much longer, larger ultra-magnet. This allows one to focus on and perfect a simpler, smaller base design and then build on that design to achieve the overall desired magnetic field strength MDU in the desired length. See the Micro-Ultra Magnet (MUM) discussed later for more detail on a similar design.

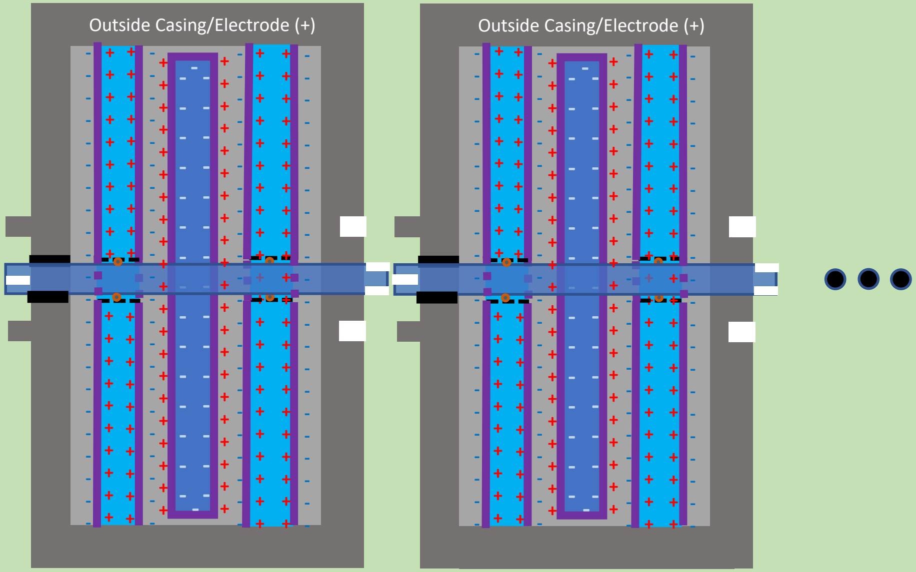

Figure 18. Modular approach to building long MDUs.

Multi-electrode Disc Ultra-magnet (MDU)

Performance

The MDUs produce similar performance to the MCUs as can be seen by comparing the magnets in Figure 10 with Figure 19.

The advantages to using discs over cylinders comes in the manufacturability of the disc magnets. It is not unusual to manufacture flats (disc shape) with optical flatness of λ/10 where λ is usually referenced to a He-Ne laser wavelength; 632.8 nm. It is also easier to pattern, coat, and selectively etch flat surfaces as opposed to curved surfaces. Additionally, as was pointed out previously, during rotation, the discs do not experience off-axis rotational moments as all centrifugal forces are directed in the plane of the discs themselves.

Figure 19 shows two configurations of MDUs, one is a smaller version, 20 cm long, 10 cm in diameter, with electrode spacings of 1.0 mm, where electrode spacing is defined as the distance from the center of one charge polarity electrode to the center of the next same polarity electrode (labeled ‘d’ in figure 17). The SD thickness is 5 microns, and the rotation velocity is 100,000 RPM. This version of the MDU can produce magnetic fields of more then 110 Tesla.

The second configuration consists of a MDU that is two meters long and one meter in diameter with 1.0 cm electrode spacings, and 5 microns thick super-dielectric layers, spinning at 100,000 rotations per minute. This configuration has the potential to produce a magnetic field in excess of 1100 Tesla.

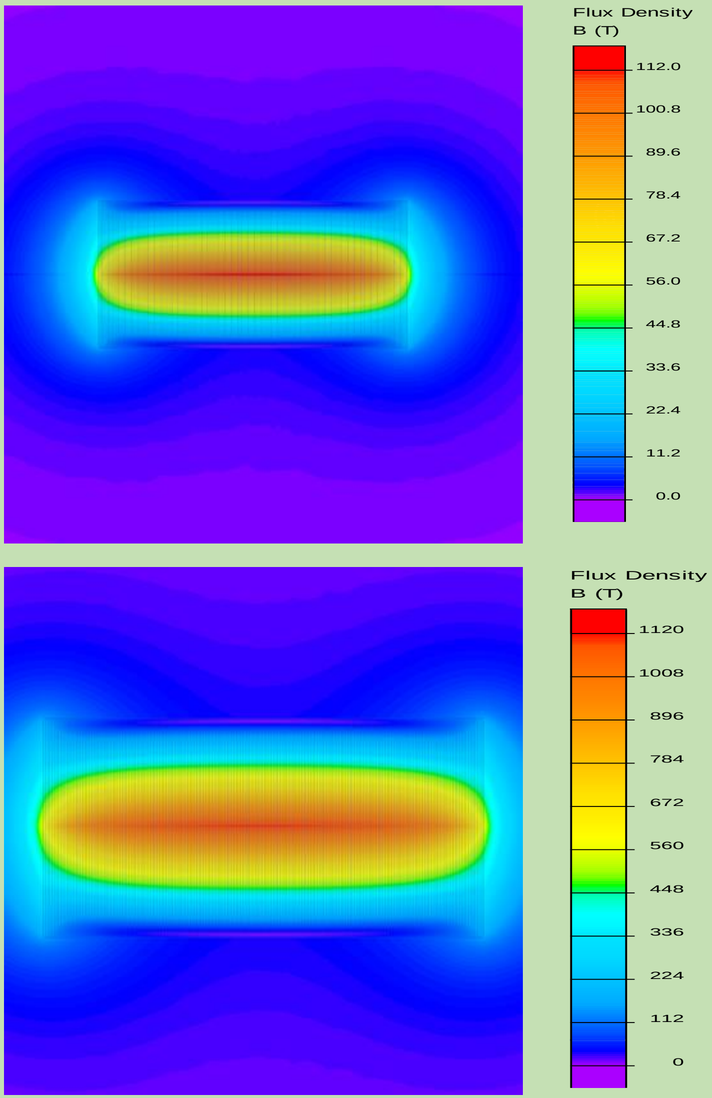

Figure 19. Multi-electrode Disc Ultra-magnet (MDU); (a) Length = 20 cm, Diameter = 10 cm, SD thickness = 5 microns, electrode spacing = 1.0 mm, RPM = 100,000; (b) Length = 2 meters, Diameter = 1 meter, SD thickness = 5 microns, electrode spacings = 1.0 cm, RPM = 100,000. Both cases k = 1e9, Voltage = 2 V. *Figure updated*

MDU Performance Cont.

Performance of the MDU can be improved by improving on a number of factors. A higher dielectric constant will enhance the performance, however, in these analysis, super dielectric constants that can be produced at this writing will be used. The thickness of the dielectric layer can be reduced to improve performance, the rotation speed of the electrodes can be increased to improve performance. And the voltage on the electrodes can be increased to hold more charge, and thus, improve performance. However, the super dielectrics in the exemplary example have a maximum voltage potential of two volts before the super dielectric experiences a degradation in performance, therefore, 2 Volts is used here. Another performance improvement is to pack as many electrodes as is practical into a given space. This means small spacings between the disc electrodes in the axial direction is desirable.

Figure 20 shows a small MCU, 20 cm long by 10 cm in diameter, with a number of different electrode spacings and dielectric thicknesses simulated. Here it can be seen the effect of these two parameters on the peak magnetic field achievable, where the peak occurs at the center point of the device (i.e., at the origin). Table 3 lists the corresponding values for reference. As expected, a power series provides an excellent fit to the data as can be seen in the one-micron dielectric thickness case in Figure 20.

Even such a small MCU unit possesses the potential to produce peak magnetic fields on the order of tens or hundreds of Tesla.

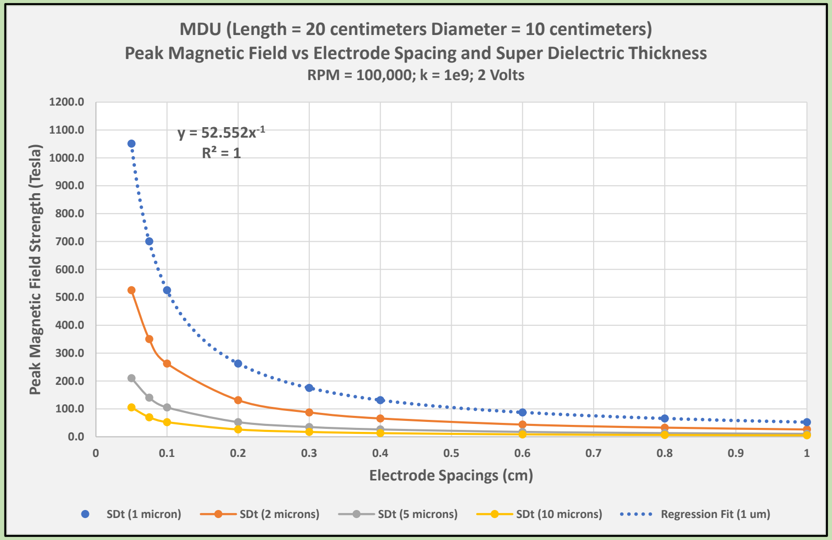

Figure 20. 20 cm x 10 cm MDU peak magnetic fields. QuickField$^{\text{TM}}$ simulation results.

Electrode Spacing (cm)	SDt (1 micron)	SDt (2 microns)	SDt (5 microns)	SDt (10 microns)
1	52.6	26.3	10.5	5.3
0.8	65.7	32.8	13.1	6.6
0.6	87.6	43.8	17.5	8.8
0.4	131.4	65.7	26.3	13.1
0.3	175.2	87.6	35.0	17.5
0.2	262.8	131.4	52.6	26.3
0.1	525.5	262.8	105.1	52.6
0.075	700.7	350.3	140.1	70.1
0.05	1051.0	525.5	210.2	105.1

Table 3. 20 cm x 10 cm MDU peak magnetic fields in Tesla. QuickField$^{\text{TM}}$ simulation results.

MDU Performance Cont.

Figure 21, and corresponding Table 4, show the simulated results for a larger MDU – 2.0 meters in length by 1.0 meter in diameter.

In an extreme example, the 2.0 meter x 1.0 meter MDU with a super-dielectric layer thickness of one micron and a 1.0 mm electrode spacing reaches a peak magnetic field strength in excess of 50,000 Tesla. Such an extreme example involves a number of engineering challenges but demonstrates the potential of the technology.

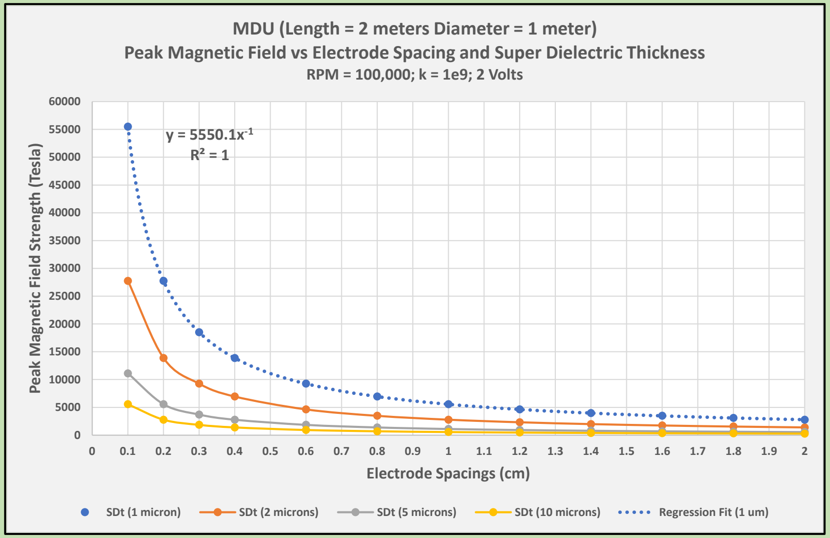

Figure 21. 2 meter x 1 meter MDU peak magnetic fields. QuickField^{TM} simulation results.

Electrode Spacing (cm)	SDt (1 micron)	SDt (2 microns)	SDt (5 microns)	SDt (10 microns)
2	2775	1388	555	278
1.8	3083	1542	617	308
1.6	3469	1734	694	347
1.4	3964	1982	793	396
1.2	4625	2313	925	463
1	5550	2775	1110	555
0.8	6938	3469	1388	694
0.6	9250	4625	1850	925
0.4	13875	6938	2775	1388
0.3	18500	9250	3700	1850
0.2	27750	13875	5550	2775
0.1	55501	27750	11100	5550

Table 4. 2 meter x 1 meter MDU peak magnetic fields in Tesla. QuickField^{TM} simulation results.

Multi-electrode Spherical Ultra-magnet (MSU)

It should be clear that a multi-electrode spherical ultra-magnet (MSU) can be similarly constructed to the MCUs and MDUs.

Figure 22 shows one such MSU one meter in diameter with electrode spacings of 1 cm, with 5 um super-dielectric layer thickness, and rotation rate of 100,000 rpm.

The MSU performs similarly to the MCU and MDU units, however, from a practical standpoint it may be more difficult to construct. The MSU is included in the spirit of the current subject matter.

The magnetic field shape does have a different distribution than the MCU and MDU which could be advantageous in some applications.

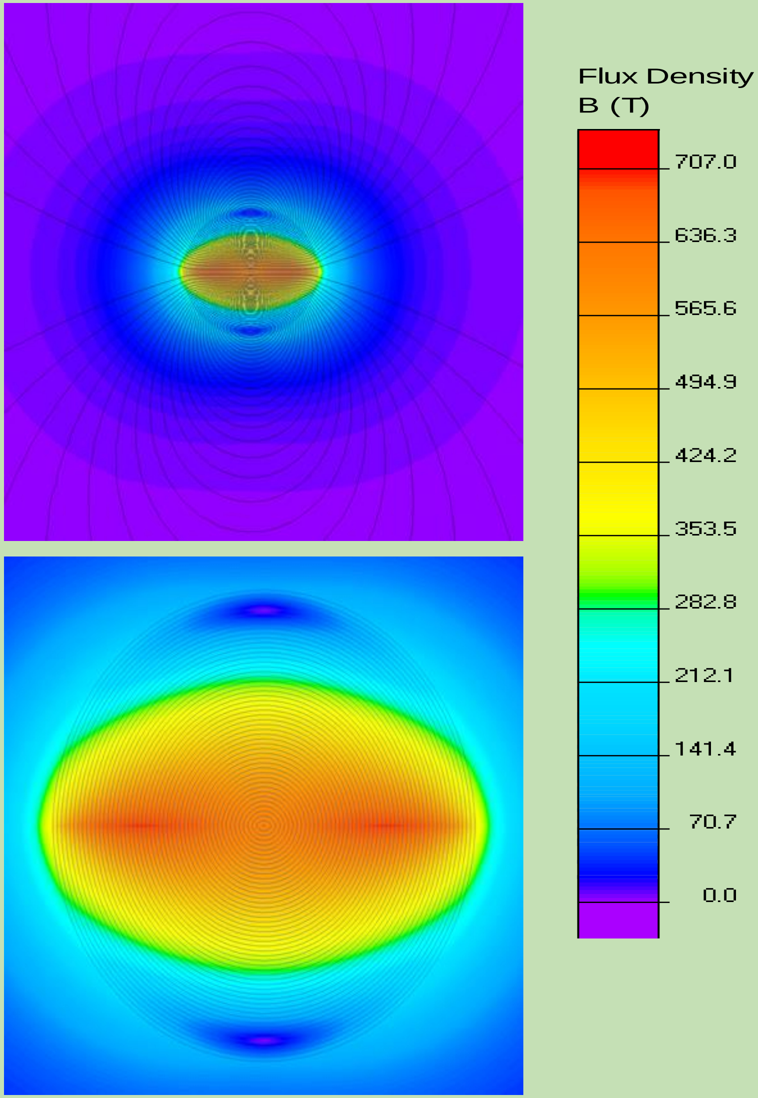

Figure 22. Multi-electrode Spherical Ultra-magnet (MSU). Diameter = 1 meter, electrode spacings = 1 cm, k = 1 x 10^9, super dielectric thickness = 5 microns, rotation = 100,000 RPM. *Figure updated*

Working Area

The magnetic field strengths stated so far have been at the center of the ultra-magnet; with the magnet being a solid unit. This configuration is not ideal since the maximum strength magnetic field, which could act on the desired materials, is buried within the magnet.

Figure 23 shows a 2 meter x 1 meter MCU with the center 10 cm being hollow. The hollow area can be an area for acting on any desired materials by the magnetic field where the field is at maximum strength.

The field strength at the center of the magnetic hollow remains in excess of 1100 Tesla. As can be seen in Table 5, the field strength is only slightly diminished from the non-hollow MCU performances. The MDU produces nearly identical results where the inner shaft now has a hollow area at its center as the working area. This result follows from the fact that the charges on the plates have their highest velocity on the outer edges resulting in the highest effective current as one goes out in radius, see figure 23a, meaning the inner parts of the disc do not contribute strongly to the production of the magnetic field and can be excluded without much penalty.

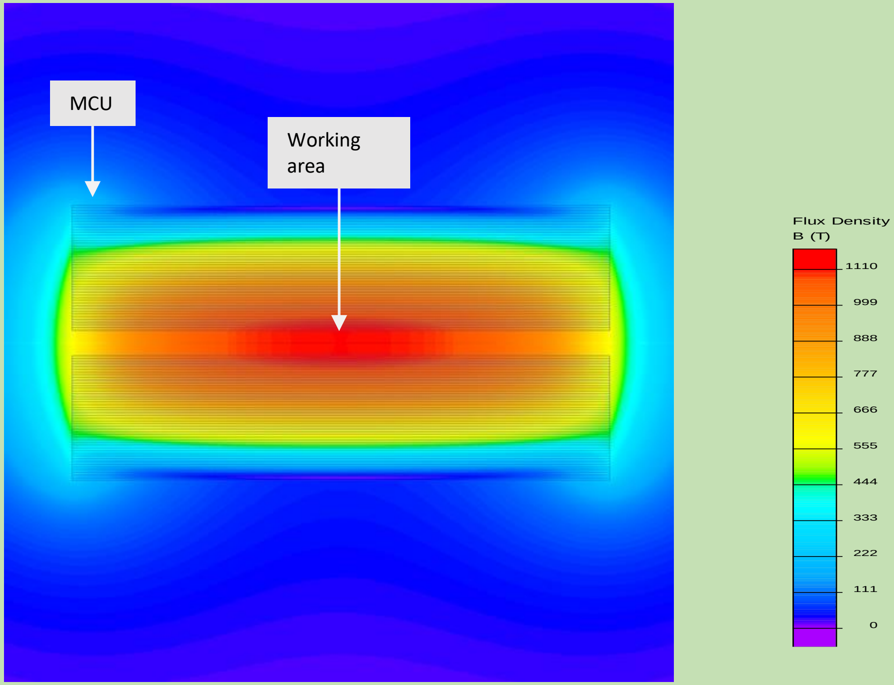

Figure 23. Multi-electrode Cylinder Ultra-magnet (MCU) with 10 cm hollow center; Length = 2 meters, Diameter = 1 meter, SD thickness = 5 microns, electrode spacings = 1.0 cm, RPM = 100,000 , k = 1e9, Voltage = 2 V. Axisymmetric model with the horizontal axis being the axis of symmetry. *Figure updated*

Electrode Spacing (cm)	SDt (1 micron)	SDt (2 microns)	SDt (5 microns)	SDt (10 microns)
2	2724	1362	545	272
1.8	3131	1565	626	313
1.6	3482	1741	696	348
1.4	3965	1982	793	396
1.2	4538	2269	908	454
1	5550	2775	1110	555
0.8	6858	3429	1372	686
0.6	9178	4589	1836	918
0.4	13609	6805	2722	1361
0.3	18249	9124	3650	1825
0.2	25933	13608	5445	2720
0.1	50515	27065	10825	5410

Table 5. 2 meter x 1 meter hollow MCU magnetic field strength at center in Tesla. QuickFieldTM simulation results.

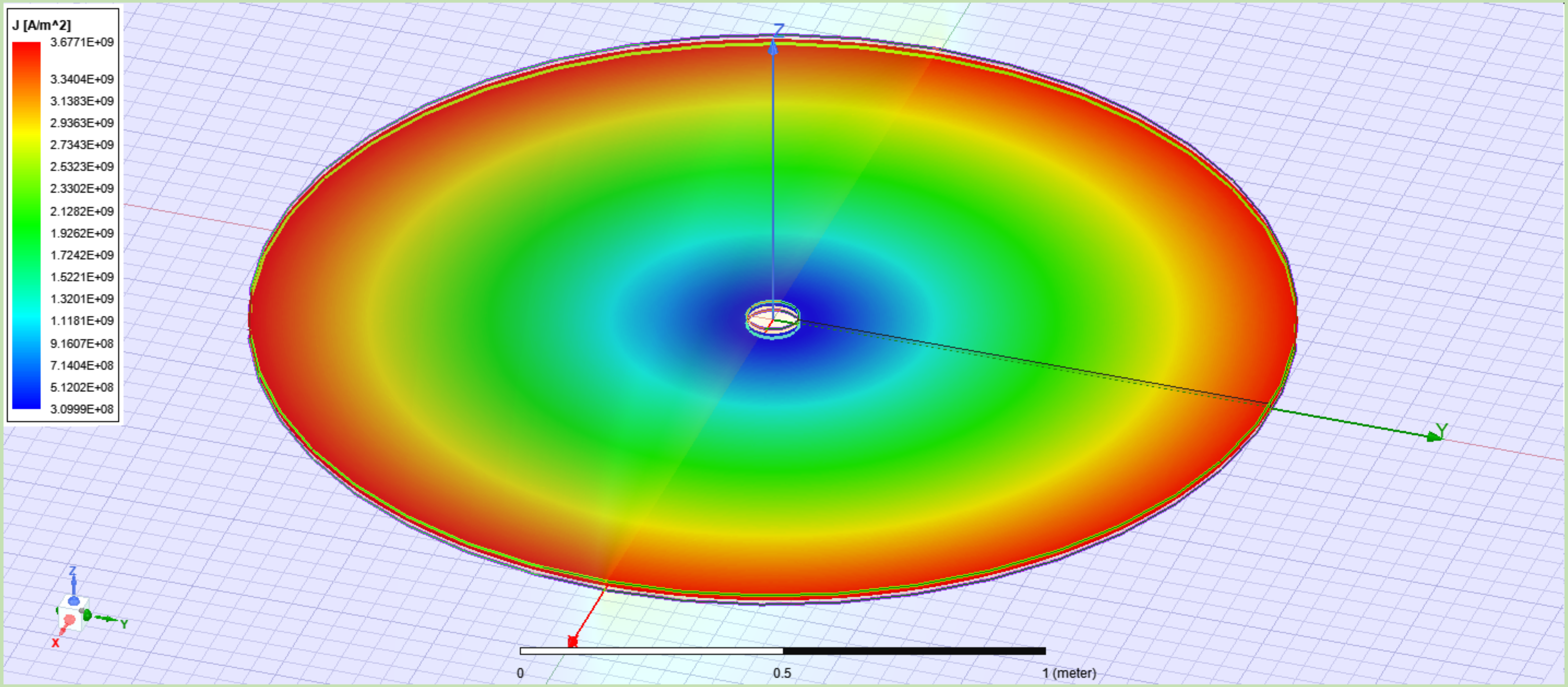

Figure 23a. The effective current distribution for a 2-meter diameter disc, with counter rotating electrodes; d = 2 microns; k = 1×10^9; RPM = 100,000; V = 2 volts; thickness = 2 cm.

Working Area

Additionally, ultra-magnets can be placed in close proximity with a gap between them; where the field will bridge the gap and create a working space outside the magnets. Shown in Figure 24 are two MDUs side by side with a 10 cm gap between them. The resulting magnetic field strengths, at the origin between the two magnets, are shown in Table 6.

While only two geometries have been shown here, any number of geometries and configurations can be used; as the application and orientation of the magnetic field requires.

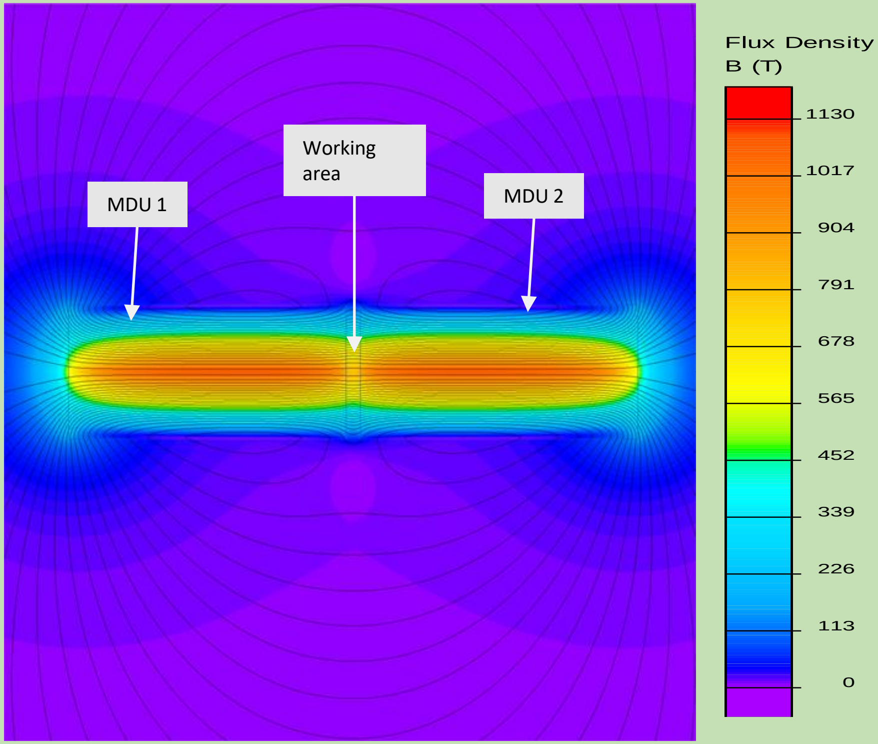

Figure 24. Side by side Multi-electrode Disc Ultra-magnets (MDUs) with 10 cm separation; Lengths = 2 meters, Diameters = 1 meter, SD thickness = 5 microns, electrode spacings = 1.0 cm, RPM = 100,000 , k = 1e9, Voltage = 2 V. Axisymmetric model with the horizontal axis being the axis of symmetry. *Figure updated*

Electrode Spacing (cm)	SDt (1 micron)	SDt (2 microns)	SDt (5 microns)	SDt (10 microns)
2	2014	1007	403	201
1.8	2237	1119	447	224
1.6	2517	1259	503	252
1.4	2877	1438	575	288
1.2	3356	1678	671	336
1	4027	2014	805	403
0.8	5034	2517	1007	503
0.6	6712	3356	1342	671
0.4	10068	5034	2014	1007
0.3	13425	6712	2685	1342
0.2	20137	10068	4027	2014
0.1	40274	20137	8055	4027

Table 6. 2 meter x 1 meter side by side MDUs magnetic field strength at center between MDUs in Tesla. QuickFieldTM simulation results.

Micro Ultra-Magnet (MUM)

Strong magnetic field miniature ultra-magnets can be manufactured. The basic construction is similar to that of the MDUs, but on a much smaller, more compact scale. All of the design considerations aforementioned with MDUs should be included and referenced with the MUMs as well and vice versa. Figure 25 shows the basic anatomy of the magnetic core of an example Micro Ultra-Magnet (MUM).

The design consists of a series of inner plates attached to a central shaft and a series of interspaced (between the inner plates) outer plates attached to the outer cylinder, also known as the outer casing. The central shaft is attached to the ID (inner race) of a rotary bearing and the outer cylinder is mated to the OD (outer race) of the same rotary bearing. Note the visible gap between the inner discs and the outer cylinder. Also, in the zoomed in perspective in figure 26, it can be seen that there is a small gap between the outer plates and the inner shaft. The central shaft and inner plates are intended to rotate in one rotational direction, and the outer cylinder, endcaps, and outer plates are intended to rotate in the opposite rotational direction, thus the outer plates should not contact the central shaft. It should be understood that it is possible to have only one of the inner or outer sub-assemblies rotate and still produce large magnetic fields, however, as pointed out previously there are advantages to having both sub-assemblies counter-rotate.

Figure 25 shows a preferred embodiment of a MUMs core, the outer discs are 10 mm in diameter as is the inner diameter (ID) of the outer cylinder. The drawing is not to scale as, in reality, the inner discs would be only a hundred microns or less in diameter than the outer disc diameters, and the axial spacing between the inner and outer discs would be tens of microns or less to achieve maximum packing density of the charge carrying discs. The details would not otherwise be discernable in the drawing, therefore, those drawing dimensions are distorted here for clarity.

The rotary bearing is somewhat notional, though a commercially available rotary ball bearing is used here. It should be understood that rotational bearing elements is an established field of engineering and any number of rotational bearing members can be used here. The small size of the MUM allows for very large rotational speeds, from a rotary bearing speed limitation perspective. Ceramic ultra-high-speed rotational rotary bearings with a dmn rating of 2.6 million are currently available at the time of this writing [6]. The bearing shown here has an ID of 1 mm and an OD of 2.5 mm, this translates into a rotational speed limitation of approximately 150,000 rpm based on bearing limitations.

Micro Ultra-Magnet (Magnetic Core unit)

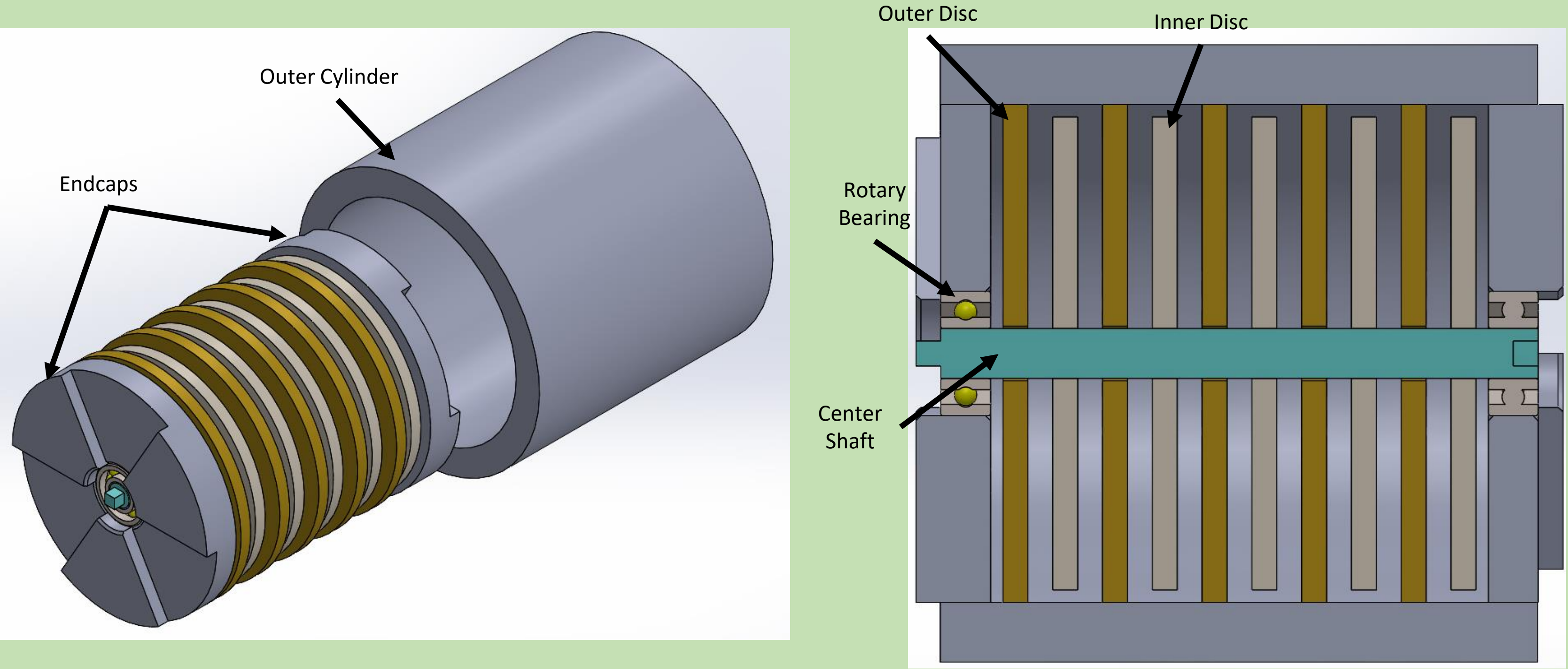

(a)

(b)

Figure 25. Micro Ultra-Magnet (MUM) Core. (a) an exploded view of the MUM core; (b) a cross-sectional view of the MUM core.

Micro Ultra-Magnet Core (continued)

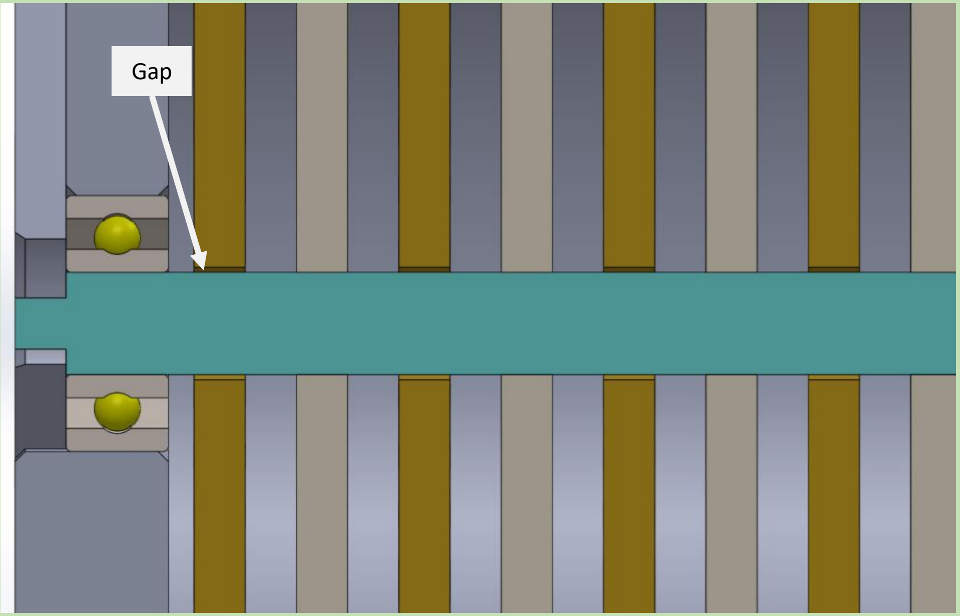

Figure 26. Expanded view of the MUM Core, showing the radial gap between the outer discs and the central shaft.

MUM Core Construction

If larger thicker discs are to be used, the discs, central shaft, and endcaps can be conventionally machined from metal, ceramics, glass, or other materials. However, to achieve extreme packing densities of the discs, and thus, high charge densities, and correspondingly high magnetic field strengths, special construction techniques of the MUM Core need to be considered.

Because of the centrifugal forces generated by the high rotational speeds combined with the preferred thinness of the discs needed to get high packing densities further combined with very strong electromagnetic stresses generated within the device itself, extremely strong materials should be used.

As a preferred embodiment, the outer cylinder is constructed of sapphire, the outer discs are constructed of diamond, the inner discs are constructed of sapphire, and the central shaft is constructed of diamond or fused silica or quartz. The endcaps can also be made of diamond. Silicon carbide (SiC) may be substituted for sapphire and fused silica may be substituted for diamond if structural stresses allow for a particular application.

In addition to their strength, the choice of materials is based upon their thermal expansion coefficients. Table 7 lists the CTE's of the materials listed above as well as a few other candidate materials. When the MUM is assembled it is done at a high temperature. The outer diameter of the central shaft and the inner diameter of the inner discs being very close to the same size at room temperature, the inner shaft being a few microns or more larger than inner diameter (hole) of the inner discs. When assembled at high temperature, the central shaft (fused silica) is able to fit through the inner radius of the inner discs (sapphire). Upon cooling, the sapphire will shrink much more than the fused silica, thus the inner discs clamp down tightly on the central shaft. Additionally, the central shaft and inner discs can be coated with a thin layer of malleable metal such as gold or indium which will cold weld the parts together through the extreme radial contact pressure generated by the CTE mismatch.

The outer discs are similarly attached to the outer cylinder whereas in this case the outer cylinder (sapphire) shrinks down onto the outer diameter of the outer discs (diamond) and is similarly cold welded to the metal coated ID of the outer cylinder and the metal coated OD of the outer discs. The endcaps (diamond) are attached in a similar fashion as the outer discs to the outer cylinder. The rotary bearings can be press fit into the endcaps after the fact or brazed into place.

Sacrificial spacers can be placed between the discs to provide precise spacing between the discs during assembly. The discs and endcaps can be placed onto the central shaft using a flip-chip die bonder. Modern die bonders can allow for sub-micron placement as well as heating the element while they are placing the element. Once the discs and endcaps are on the central shaft, the sapphire outer cylinder can be heated and slid over the outside of the discs and endcap assembly and allowed to cool.

While graphene is not used in the current embodiment, graphene is a rapidly advancing material that has a great number of useful properties. While not at a stage to be useful as a base material at this writing due to size and thickness limitations, workable graphene is likely to become available in the future and is included here for completeness. The listed materials, table 7, are expected to be good choices for the present devices; however, this list is in no way comprehensive as a large number of high strength materials of suitable thermal expansion coefficients exists; these are examples of suitable materials to demonstrate the concept.

Material:	**Thermal Expansion (10e-6 / deg K)**
Diamond	0.7
Sapphire	6.66
Fused Silica	0.55
Silicon Carbide	7.9
Silicon Nitride	3.3
Super Invar	0.63
Zerodur ™	0.0 +/-0.007
Graphene	-3.76

Table 7. Coefficients of Thermal Expansion (CTEs) of some candidate materials.

MUM Core Construction (continued)

To recap the assembly process in more detail,

1. The MUM is assembled vertically to allow gravity to stack the parts.
2. The bottom radial bearing is placed in the bottom endcap and the central shaft inserted into the ID of the bearing.
3. The endcap and central shaft are then brazed or laser welded to the bearing.
4. A sacrificial spacer is placed on top of the bottom endcap.
5. Inner and outer discs, with the super-dielectric matrix already applied to the discs, are alternately placed on the central shaft. The inner discs must be heated to fit over the non-heated central shaft. The outer discs have a larger central hole and do not require heating. Sacrificial spacers are placed between each disc placement to precisely control the spacing between discs.
6. Step 4 is repeated until the MUM disc stack is of the desired height on the central shaft.
7. A sacrificial spacer is placed on the top disc.
8. The top endcap is then placed on the central shaft.
9. The outer cylinder is then heated and slid over the un-heated disc-endcap assembly. Upon cooling the outer cylinder will clamp the outer discs and endcaps into their proper radial position as well as bond them into place on the outer cylinder. Great care must be taken that the clocking features of the upper and bottom endcaps are placed so that they align correctly as they are keyed to one another (this can be accomplished with a jig or assembly fixture).
10. The sacrificial spacers are then selectively dissolved and removed with a chemical process; selective in that the spacers are dissolved and the other components are unaffected.
11. The inner cavity (the cavity containing the discs) is then cleaned with a solvent flush and vacuum dried to remove any liquid remnants from the spacer removal and solvent flush.
12. The inner cavity is then filled with a super-dielectric solution while under ultrasonic agitation. This allows the super-dielectric fluid to enter the nano-structure matrix and create the final super-dielectric layer (being the nano-matrix and super-dielectric fluid combined). This process can be greatly enhanced if the inner cavity is under vacuum at the time of the dielectric fluid introduction; allowing the super dielectric fluid to be pulled into the nano-structure matrix and to minimize the potential for trapped air pockets.
13. The super-dielectric fluid is then drained from the inner cavity. Due to the capillary effect, the super-dielectric fluid will strongly remain in the nano-tube structures while the bulk fluid will drain away.
14. Mercury is injected into the empty space in the inner cavity, filling the cavity.
15. The top radial bearing is inserted into the top endcap and brazed or laser welded into place.

The mercury can be under pressure to minimize any air pockets that may be left behind, though this is not necessary if care is taken to remove air pockets and empty spaces during the mercury filling process, as described. The mercury holds the super-dielectric fluid in place in the nano-structure matrix and prevents it from escaping or drying out, effectively providing a seal. The super-dielectric fluid in most cases will be an acid, a base, an aqueous salt, ionic fluid, or other electrolyte. Mercury does not react with most acids, does not react with alkali bases, and is immiscible with water solutions, thus mercury can be in contact with the super-dielectric fluid without detrimental effects, and thus, provides a good choice for the conductive slip joint fluid in this preferred embodiment.

MUM Component Construction

In order to achieve the dimensions and tolerances needed for the high-density electrode MUM devices with the high strength materials described, special considerations are taken in the construction of the components.

Diamond and Sapphire are common chemical vapor deposition (CVD) and wafer growth materials. Single crystalline diamond can be deposited in large diameters, i.e. >5 cm, with thicknesses in excess of 2 mm [7]. Sapphire can be made in much larger dimensions, indeed sapphire optics over 50 centimeters in diameter of more than 10 cm thick are available commercially [8]. Likewise, these materials can be deposited in very thin layers as low as tens of nano-meters. Fused silica is a very common material used in fiber optics and optical components in general and can be made in nearly any desired shape and size.

In the preferred embodiment the central shaft is made of fused silica 1.0 mm in diameter, this is a common core size for fused silica fiber optics and can be readily obtained commercially. To note, if additional strength is needed of the central shaft, diamond can be used, though fused silica will suffice in most cases. The outer cylinder is simply a tube of sapphire with an ID of 10.0 mm and a wall thickness of 2.0 mm. The outer cylinder can be obtained, with very exact tolerances, by any number of optical component vendors who specialize in sapphire optical components.

The discs and endcap present more of a challenge as they posses some features that must be produced during the manufacturing process, e.g. center holes on the discs and endcap and the raised rotational interlocking castellation features of the endcap, discussed later. Also, the discs must be extremely flat and of an exact thickness and diameter (inner diameter for the inner discs and outer diameter for the outer discs).

The inner discs of sapphire are not difficult to realize as appropriate sized sapphire substrates can be commercially purchased. With the appropriate substrate. the center hole can either be machined, ground, and polished to exact tolerances or if the disc is thin enough, reactive ion etching (RIE) or similar anisotropic plasma etching process can be employed with the remainder of the disc masked off to produce the center hole, see figure 27. Since the mask is typically patterned with photolithography, the hole diameter can be controlled to much better than sub-micron tolerances.

In the case of the diamond outer discs, the substrate used for CVD diamond growth can be patterned beforehand using very typical integrated circuit patterning technology, e.g., photolithography patterning with metal vapor deposition to mask the areas where growth is not required or desired. See figure 28. Again, since the patterns can be made to much better than sub-micron tolerances due to the nature of the micro-chip fabrication technology used. If even better precision were to be required, e-beam or imprint lithography can likewise be used.

The diamond is then grown on the exposed substrate. The thickness of the diamond can also be very precisely controlled to much better than sub-micron tolerances during the CVD process. The mask material and sacrificial substrate can then be etched away leaving only a diamond disc of exact dimensions behind. Patterning, masking, etching, and material deposition on wafers and substrates is well known to anyone in the art of micro-chip fabrication and nano-technology.

If the diamond disc is thin enough, a monolithic disc of exact thickness can be grown and the hole and diameter can be produced to exact dimensions using masking and plasma etching as was discussed with the sapphire discs.

The inner and outer discs can then be coated with metal through vapor deposition, such as sputtering, to make them conductive. Electroplating can then be used to make the metal thicker if desired, such as in the cold weld joint assembly areas for example (i.e., where the inner disc come into contact with the central shaft and the outer disc come into contact with the outer cylinder). A metal oxide, or one of the other super-dielectric matric materials discussed, can then be grown and patterned to produce the super-dielectric nano-structures needed for the super dielectric layer. In the exemplary example, the thickness of the super dielectric matrix pattern would be 1-2 microns in thickness, though other thicknesses are certainly possible.

In this way the thickness of the discs can be made very thin allowing for high packing densities in the MUM. In the exemplary example the thickness of the discs would be tens of microns up to a hundred microns,   though other thicknesses being possible from sub-micron to millimeters or more.

MUM Component Construction

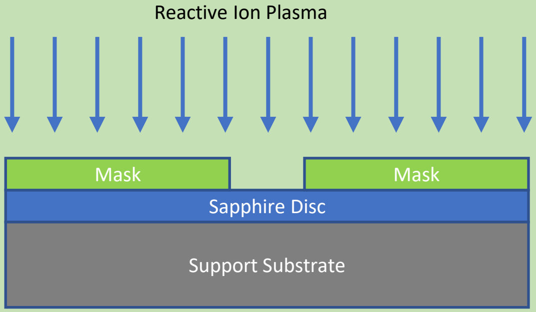

Figure 27. RIE etching of the center hole for the sapphire inner discs.

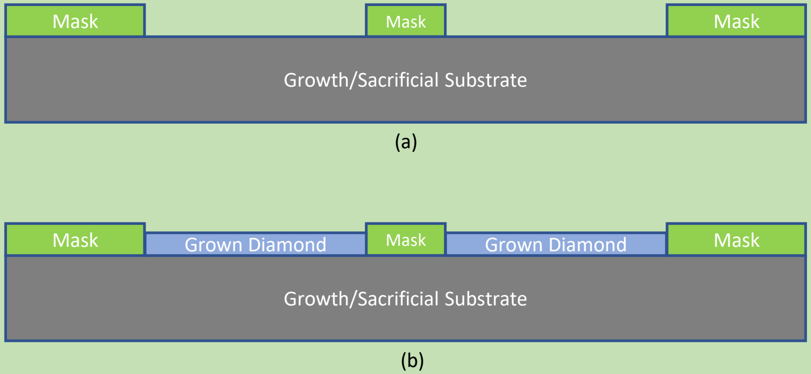

Figure 28. Making of the outer diamond disc; (a) patterning/masking of the growth substrate, (b) CVD grown diamond in the exposed areas.

MUM Component Construction (continued)

As an additional note, when the super-dielectric matrix material is patterned and etched to make the nano-structures, the etching can be done such that the nano-structure ‘pockets’ are at an angle with their tops leaning in towards the central axis and their bottoms away from the central axis. This will help insure the super-dielectric fluid stays in place under the centrifugal forces the fluid may experience under high rotation velocities. Figure 29 shows a basic schematic of the concept. This can be done by simply tilting the substrate relative to the anisotropic ion etching stream.

These concepts can also apply to the construction of the MDU components as well.

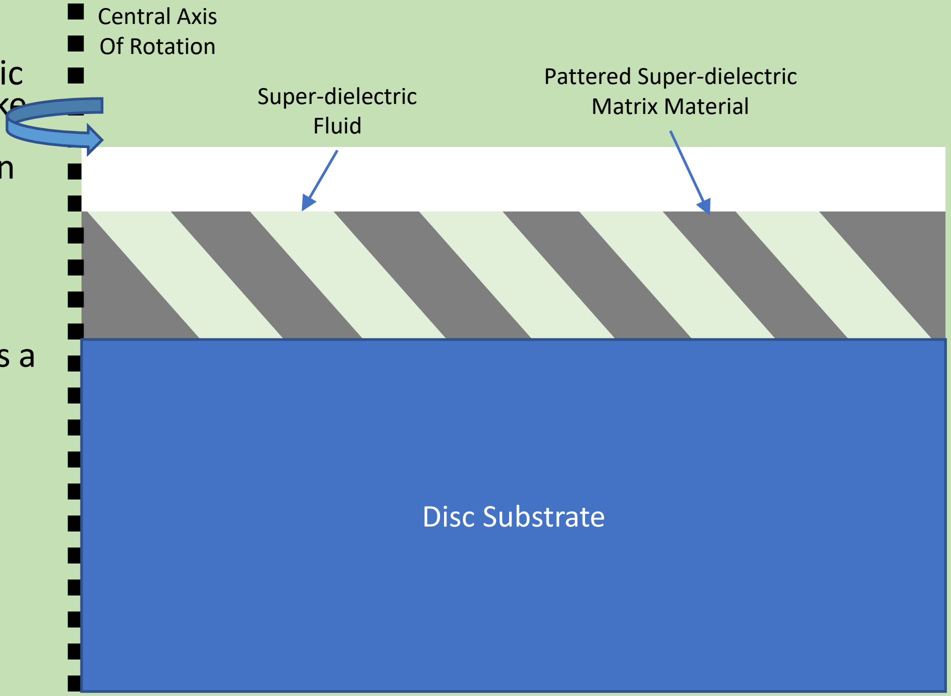

Figure 29. Schematic showing the super-dielectric matrix material patterned and then etched at an angle such that the super-dielectric fluid is held in place during high-speed rotations.

MUM Construction (continued)

If the endcaps are made of fused silica, they can simply be machined using freeform optics machining capabilities currently in use, by companies such as Optimax for example.

If the endcaps are made of diamond, they may be made using a process similar to that of the discs, but with more process steps. Figure 30 illustrates.

The substrate is first masked to provide the appropriate outer diameter and center hole diameter.

The diamond is then grown to the desired thickness on the exposed substrate, in the embodiment shown in figure 25, this is 1.0 mm.

The growth is halted and a secondary mask is added to pattern the clocking/gear features. The diamond growth is continued, thus raising the clocking features on the endcap, in the current embodiment an additional 1.0 mm.

The masks and substrate are removed, leaving only the finished diamond endcap.

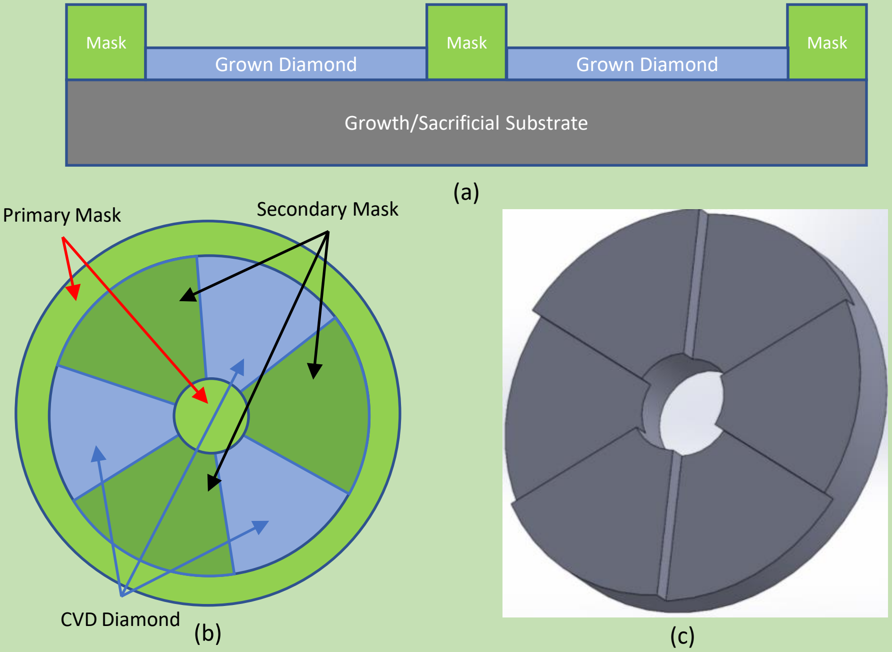

Figure 30. Manufacturing of the diamond endcaps; (a) setting the diameter and inner radius of the endcap [side view], (b) secondary mask to grow the clocking features [top view], (c) finished endcap.

MUM Performance

Figure 31 and Table 8 shows the simulated performance of a 10 mm long x 10 mm diameter MUM core unit. The total size including outer cylinder and endcaps is 12 mm long x 12 mm diameter, not including the clocking teeth on the endcaps since they are buried when the MUMs are interconnected, see discussion later. Including the clocking teeth increases the length to 14 mm.

Other sized MUMs can be produced as well. Figure 32 and Table 9 shows the simulated performance of a 1.0 mm x 1.0 mm core unit constructed in the same fashion as the 10 mm x 10 mm unit.

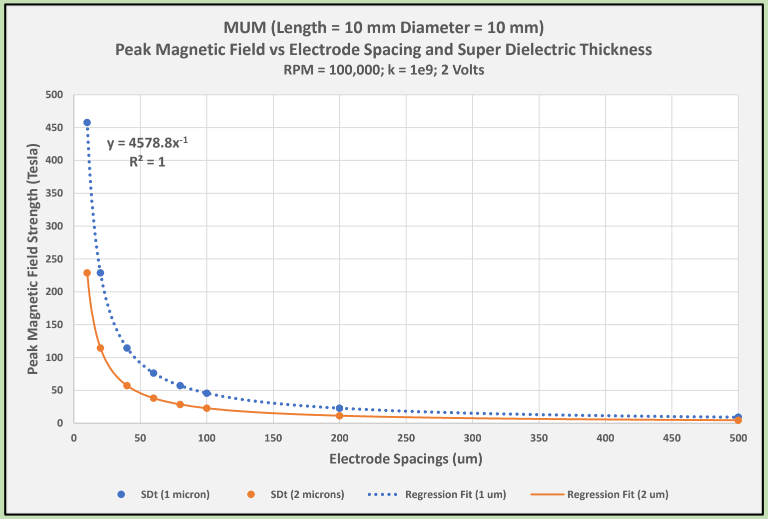

Figure 31. 12 mm x 12 mm MUM performance simulation results (QuickField^{TM}).

Electrode Spacing (um)	SDt (1 micron)	SDt (2 microns)
500	9.2	4.6
200	22.9	11.4
100	45.8	22.9
80	57.2	28.6
60	76.3	38.2
40	114.5	57.2
20	228.9	114.5
10	457.9	228.9

Table 8. 12 mm x 12 mm MUM peak magnetic fields in Tesla. QuickField^{TM} simulation results (SDt = super dielectric layer thickness).

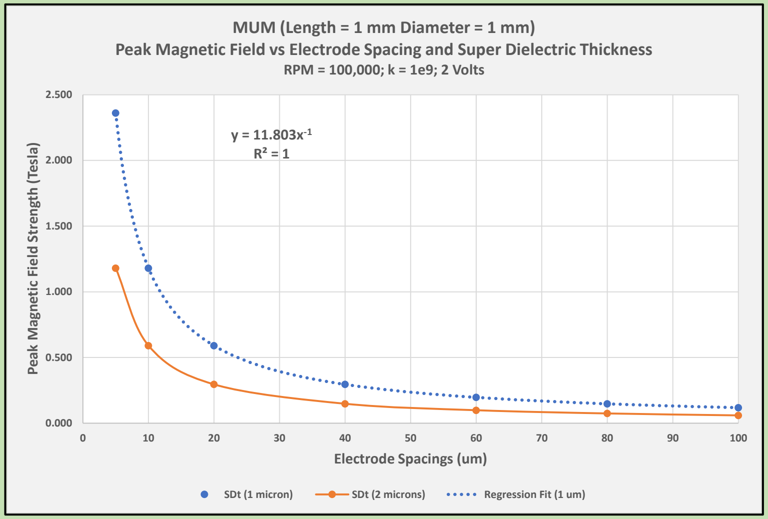

Figure 32. 1 mm x 1 mm MUM performance simulation results (QuickField^{TM}).

Electrode Spacing (um)	SDt (1 micron)	SDt (2 microns)
100	0.118	0.059
80	0.148	0.074
60	0.197	0.098
40	0.295	0.148
20	0.590	0.295
10	1.180	0.590
5	2.361	1.180

Table 9. 1 mm x 1 mm MUM peak magnetic fields in Tesla. QuickField^{TM} simulation results (SDt = super dielectric layer thickness).

MUM Assemblies

As can be seen in figure 33, the central shaft and endcaps have complimentary interlocking features at each axial end such that the MUMs may be interlocked along the lengthwise (axial) axis. This allows for multiple MUMs to be linked together and rotated by a single source, or two sources as the case may be since the central shaft and outer cylinder counter-rotate in the exemplary example.

If desired, the central shafts can be permanently attached using a sodium silicate solution, for fused silica, or ‘spliced’ together using a carbon dioxide laser.

The MUMs can be put into axial compression, for stiffness, and lines of MUMs can be placed side by side in close proximity to produce three dimensional magnetic structures. If large structures are needed or more structural support is beneficial, a linkable exostructure can be placed around the MUM core as shown in figure 34. As can be seen, alignment pins and guide holes are used to link and stack MUMs into three dimensional structures. The body can be made of nearly any desired material, though for avoidance of magnetic stresses and stray eddy currents ferromagnetic and conductive materials should be avoided. A rotary bearing provides support between the exostructure and the rotating outer cylinder of the MUM core. If only the central shaft is rotated, the exostructure rotary bearing is not required as the outer cylinder does not rotate. In this case only a clamp would suffice.

Figure 35 shows the results for a 10 x 10 x 10 MUM array stack without the exostructure. This results in an approximately 12 cm x 12 cm x 12 cm magnetic cube. The maximum magnetic field strength is not increased, being similar to that of an individual MUM, however, the stackable MUMs do allow for increased flexibility of the field shape and increased energy storage as will be discussed shortly.

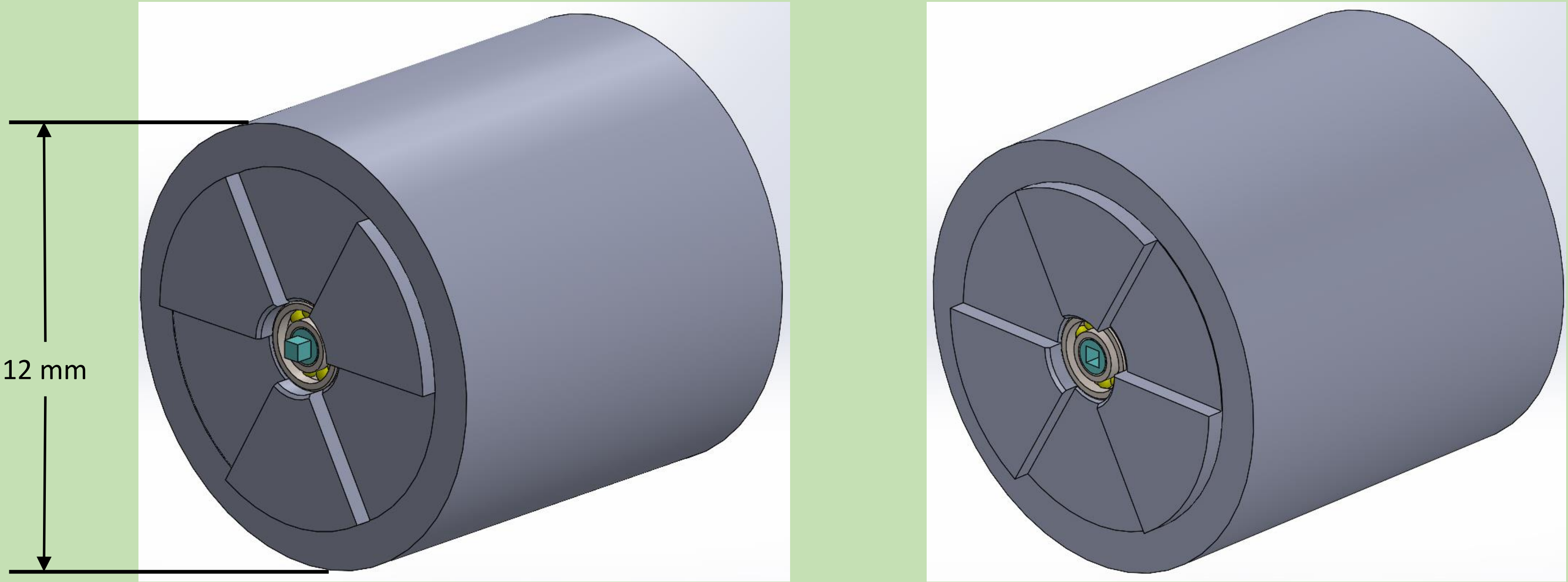

(a)

(b)

Figure 33. (a) Front view of the MUM core. (b) Rear (180 deg rotated) view of the MUM core. As can be seen, the front and rear central shaft and endcaps have complementary interlocking features allowing for the multiple MUMs to be axially linked.

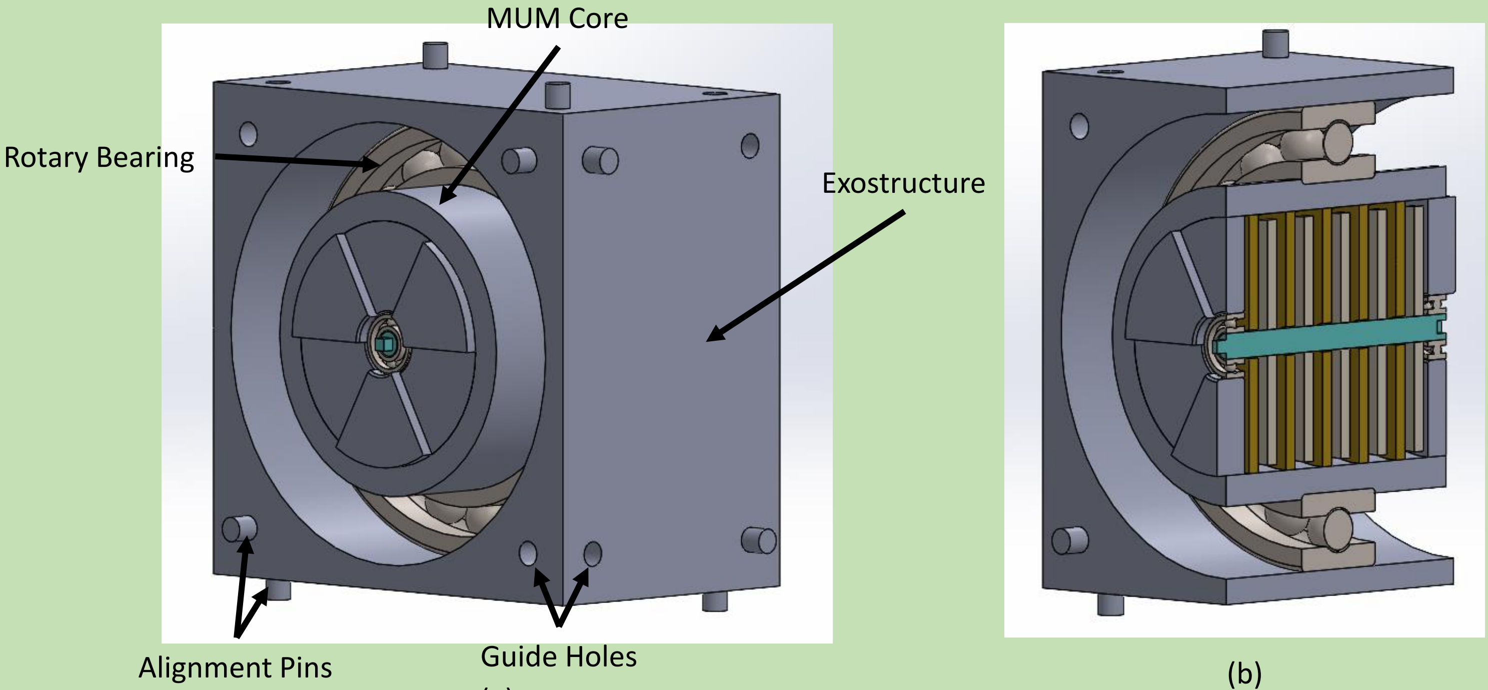

(a)

(b)

Figure 34. Full MUM including core and exostructure. This allows for large three-dimensional stacking of MUMs to create large three-dimensional magnetic structures. (a) full view, (b) cross sectional view.

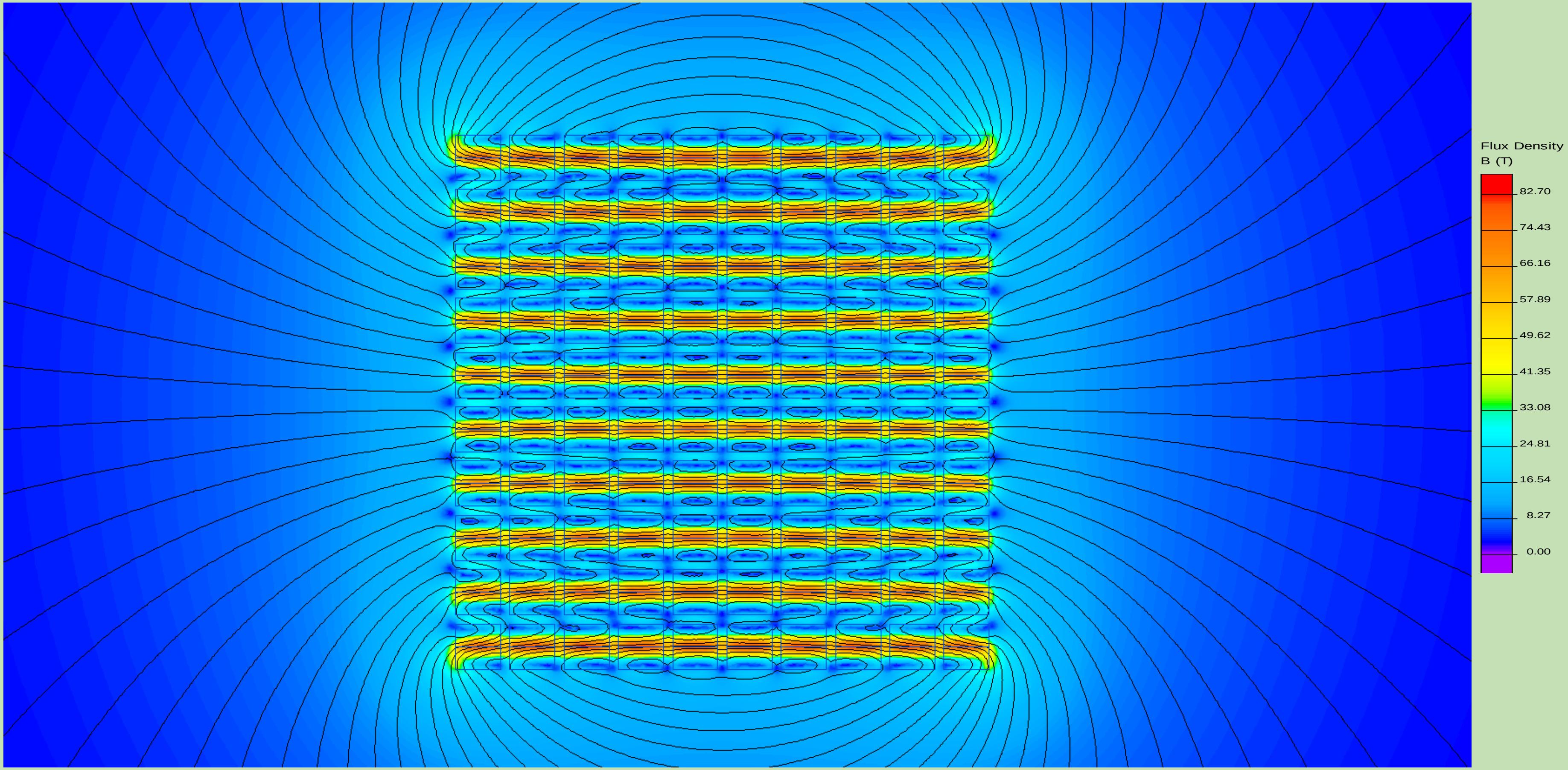

Figure 35. MUM stack simulation results. (a) 10 x 10 x 10 stack of MUMs. Individual MUM unit is 10 mm x 10 mm core with 50-micron disc spacing, 1-micron super-dielectric layer thickness (SDt), $k = 1 \times 10^9$, RPM = 100,000.

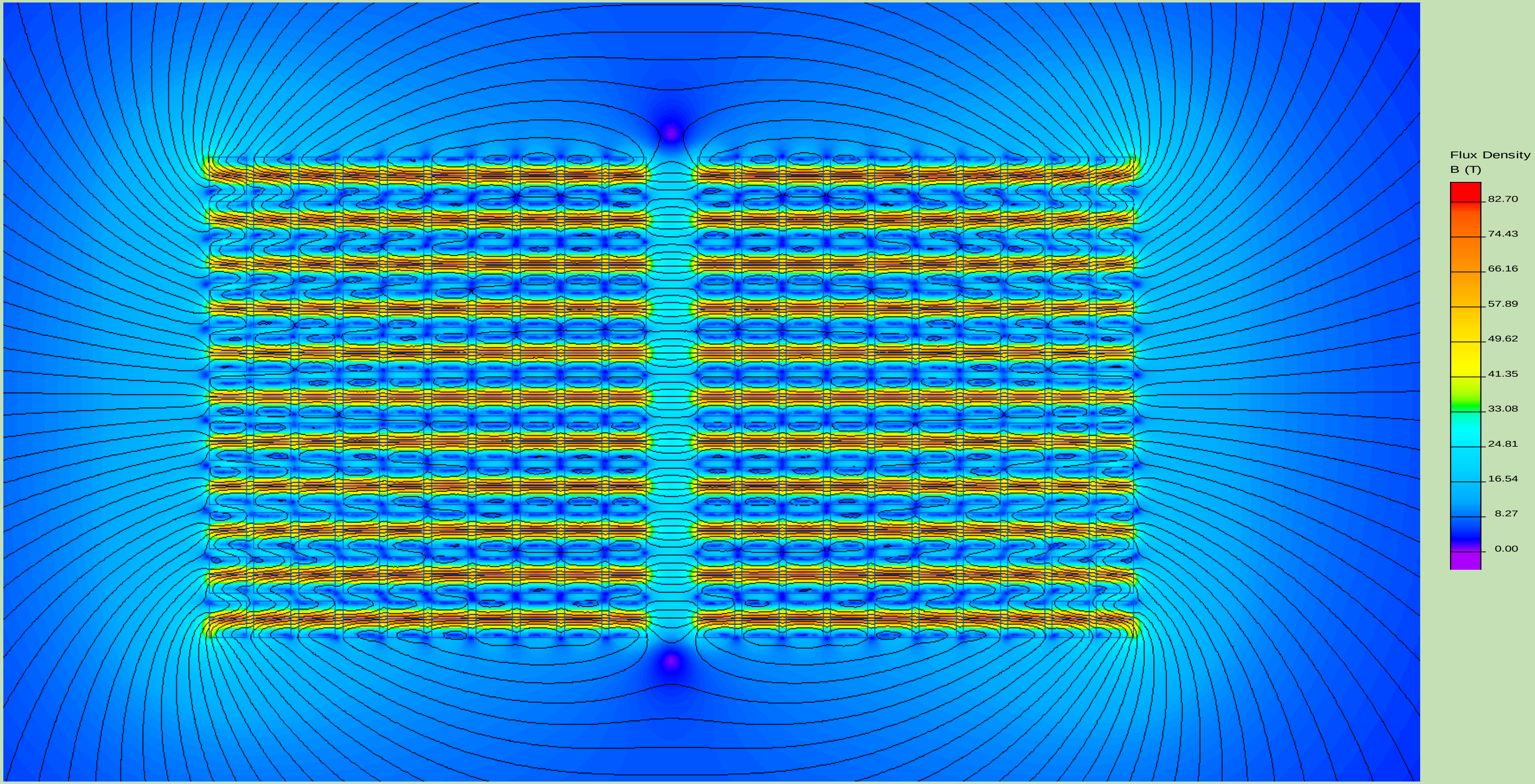

Figure 35. MUM stack simulation results. (b) two side by side 10 x 10 x 10 MUM cubes with a 12 mm spacing between them

Mercury as the Slip Joint Fluid

It is a central tenant of fluid mechanics that the fluid in contact with the wall is at the same velocity as the wall, known as the no-slip condition. This is not an ideal situation since the charge in the conductive fluid will have a similar velocity vector as the opposite charge on the electrodes which will result in a reduced net current and consequently a greatly reduced magnetic field.

As the field of micro-fluidics has grown, deeper research into the no-slip boundary condition has been undertaken. Research has shown that under certain conditions the no-slip assumption is invalid. In fact, the drag from the fluid has been shown to be two to four orders of magnitude less than predicted by the Navier Stokes Dirichlet Boundary Condition (the no-slip boundary condition). The conditions under which the fluid does not obey the no-slip boundary condition are 1) the fluid does not wet the wall material, 2) the wall surface is smooth, and 3) there is a high shear rate [9,10,11].

In some examples of the present methods and devices, mercury is used as the fluid in question. If the cohesive force of the fluid is greater than the adhesive force between the fluid and the wall material then the fluid is non-wettable with respect to the wall. The surface tension of the fluid is proportional to the cohesive forces of the fluid and is an indicator of the liquid’s wettability on surfaces; higher surface tension therefore corresponds to less wettability. Mercury has one of the highest surface tensions of any known liquid; 500 mN/m for mercury, compared to water at 72 mN/m. Mercury has an extremely low wettability factor and wets very few surfaces. Additionally, the super-dielectric matrix material can be made of a material that has low adhesion, such as metal oxides, metal fluorides, metal chlorides, metal sulfides, and so on, thus further reducing the wettability between the mercury and the moving electrodes.

The second condition is the wall surface should have low surface roughness. Due to the methods discussed in the MUM electrode construction, the walls have nano-meter scale surface roughness as a result of the manufacturing processes. This results in an extremely smooth surface. Even the large discs of the MDU can be optically polished to have extremely smooth surfaces and/or the grown or deposited super-dielectric matrix can be made nanometer smooth as well if desired.

The third condition is a high shear rate. This condition is met on multiple levels for the current design. First, it is desirable for the electrodes to be rotating at a high angular speed which results in a high shear rate. Second, it is desirable for the electrodes to be spaced closely in order to get a high packing density which results in a thinner conductive fluid layer which in turn results in a high shear rate. Finally, the electrodes are ideally counter-rotated which further results in an enhanced shear rate as well as providing for counter momentum and shear forces in the fluid velocity profile. The counter-rotation further mitigates what little adhesion there may be between the mercury and the electrode walls.

All of these conditions combined make mercury an ideal choice of slip joint fluid; the mercury does not stick to the rotating electrodes and thus the electrodes slip through the mercury as they rotate.

Manipulating the Mercury Fluid

Because of its fluidic nature and conductivity, the mercury slip joint fluid can be manipulated in the presence of the magnetic field produced by the dynamic super-capacitor (DSC), in other words the mercury can be made to flow in a desired manner using electromagnetic manipulation. One of the challenges presented so far is preventing the mercury fluid from 'sticking' to the rotating electrodes and being dragged along with the electrode rotation, causing parasitic charge motions. If a conventional electron current is flowed through the mercury, the mercury may experience magnetohydrodynamic forces. The electron currents and corresponding Lorentz forces can be configured to mitigate the drag the mercury may experience at the contact between the super-dielectric layer (SD) on the disc electrode and the mercury; further mitigating charges in the mercury close to the mercury-SD interface from being dragged along with the rotating disc - which would diminish the total effective current, i.e., parasitic charge motion. Figure 36 shows the simulated magnetic field vector between two counter-rotating oppositely charged plates, i.e., in the mercury slip-joint fluid layer. As can be seen, for the most part, the magnetic field vector inside the mercury runs perpendicular to the plane of the discs. The electron current used to exert force on the mercury is a conventional electron current as is commonly encountered in any common electrical circuit, e.g., current in a wire. The flow of the electron current can be configured such that magnetohydrodynamic forces can be exerted on the mercury in a controlled and desirable way. Electrical traces can be patterned on the disc(s) and come into contact with the mercury where desired, allowing current to flow through the mercury in a controlled and patterned way. Due to the Lorentz force, equation 8 and 9, a force is locally exerted on the mercury proportional to the perpendicular component of the local magnetic field and electron current density flow, figure 37. The force on moving charged particles in a magnetic field,

$$d\vec{F} = dQ\vec{v} \times \vec{B} \qquad (8)$$

in differential form, where $d\vec{F}$ is the differential force, dQ is a differential charge element, $\vec{v}$ is the velocity of that charge element, and $\vec{B}$ is the external magnetic field vector where dQ exists. The total Lorentz force can be written as

$$\vec{F} = \iiint_V \vec{J}dV \times \vec{B} \qquad (9)$$

in integral form, where V is the volume in which the current is contained and $\vec{J}$ is the electric current density.

The force of equations 8 and 9 is the force exerted on the electrons, the electrons may then transfer their acquired momentum to the fluid through electron-atom collisions. In this way the mercury can be made to experience a force counter to the motion of the rotating disc, or discs if two or more discs are counter-rotated. The mercury fluid can potentially be made to move counter to the rotation of the electrodes or in just about any other motional path desired. In the simulations and calculations of the present disclosure, the charges accumulated in the mercury due to the capacitive nature of the DSC are assumed to be stationary, however, this does not need to be the case as using magnetohydrodynamic forces on the mercury the mercury may be made to move with an angular momentum counter to the rotation of the electrodes.

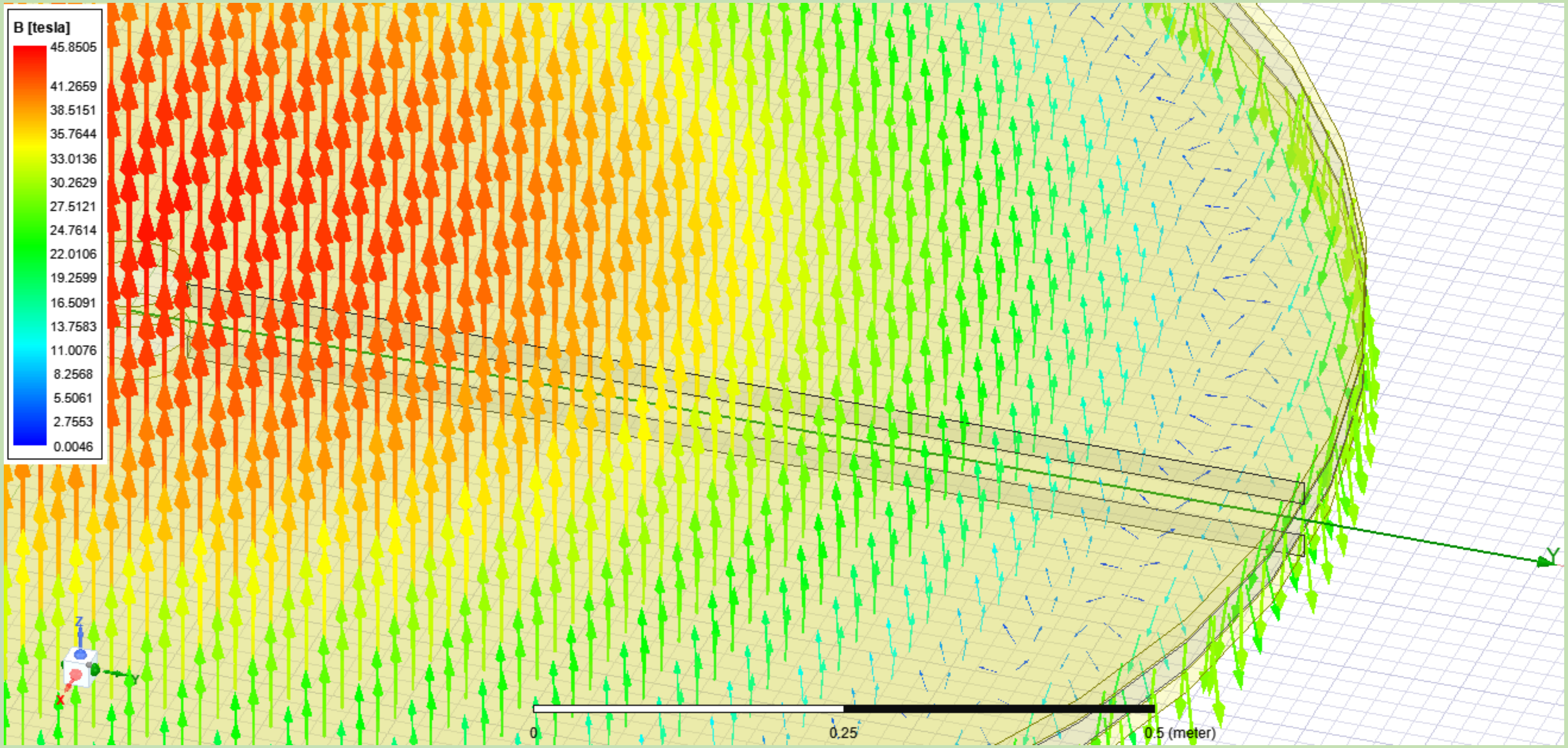

Figure 36. Simulated magnetic field vector in the mercury layer between the two discs in a counter-rotating DSC design, i.e., in the mercury slip-joint layer. ANSYS Maxwell3D^{TM}.

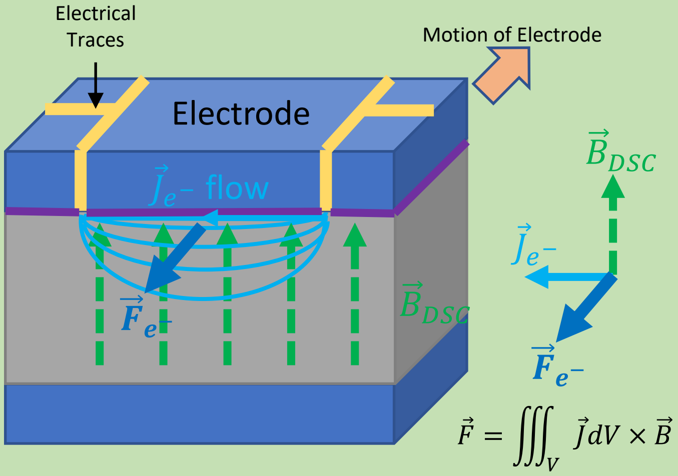

Figure 37. A volumetric segment of electrode and mercury slip layer in the DSC's magnetic field. The electron current, $\vec{J}_{e^-}$, can be configured as to produce a force, and thus motion, in the mercury that is counter to the motion of the electrodes themselves.

Energy Losses

The largest frictional energy losses to the system may be expected to come from the frictional drag between the spinning disc electrodes and the mercury fluid.

Traditionally, the skin friction drag of a fluid on the walls of the spinning plates would be estimated as [15, 16]

$$F_{Hg} = \int_S C_f \frac{\rho v^2}{2} dA \qquad (10),$$

where C_f is the skin friction coefficient, ρ is the fluid density, v is the tangential plate velocity (assumes fluid is stationary far from the plate wall), S is the area of the electrode (disc) in question to be integrated over.

$$C_f = \frac{0.664}{\sqrt{Re}} \text{, for Laminar flows} \qquad (11)$$

$$C_f = \frac{0.027}{(Re)^{1/7}} \text{, for Turbulent flows} \qquad (12)$$

where *Re* is the Reynolds number,

$$Re = \frac{\rho v L}{\mu} \qquad (13)$$

where ρ is the density of the fluid, *L* is the characteristic linear dimension of the system, and μ is the dynamic viscosity of the fluid.

Energy Losses

The power loss due to the frictional drag of the mercury can be written as

$$P_{Hg}(r) = F_{Hg}\,\omega\, r \qquad (14)$$

where *r* is the distance from the axis of rotation.

Integrating over the entire disc, spinning at 100,000 RPM, gives nonsensical results of losses of tens of billions of watts whether turbulent or laminar. Unfortunately, the system operates well outside the validity range of these traditional methods and no method exists today to accurately estimate the drag losses the spinning discs would experience in the mercury. At the heart of these calculations and indeed computational fluid dynamics as a whole is the ‘no-slip’ boundary condition in which the fluid is assumed to stick to the wall boundary. As the field of micro-fluidics has grown, deeper research into the no-slip boundary condition has been undertaken. Research has shown that under certain conditions the no-slip assumption is invalid [9, 10, 11]. In fact, the drag from the fluid has been shown to be two to four orders of magnitude less than predicted by the Navier Stokes Dirichlet Boundary Condition (the no-slip boundary condition) [9, 10, 11]. The conditions under which the fluid does not obey the no-slip boundary condition are 1) the fluid does not wet the wall material, 2) the wall surface is smooth, and 3) there is a high shear rate. All three of these conditions are abundantly met in the current implementation. The mercury may be expected not to wet the super-dielectric matrix material, the walls have nanometer scale smoothness, and due to the counter-rotation nature of the design there may be expected to be very high counter-shear rates in the mercury. The discs may readily slip through the mercury and the fluid drag may be greatly reduced. Additionally, adding a counteracting magnetohydrodynamic force to the mercury, as discussed earlier, may cause the mercury to not only not stick to the super-dielectric coated disc walls, but to move against the natural angular momentum that would otherwise be imparted into the mercury fluid. An accurate picture of the mercury’s interaction with the electrode wall is complex and not fully knowable at this time.

Mercury-less Design

While it is believed the discs may slip through the mercury fluid for the reasons previously stated, due to the uncertainties associated with the mercury-wall interactions, an alternate design will be discussed which eliminates the need for a conductive slip-joint fluid altogether.

One of the major advantages to the use of a liquid conductor, i.e., mercury, as one of the electrodes is the ultra-magnet system components may be constructed and operated with relatively lax tolerances as these tolerances can be taken up in the mercury. If great care is taken with tolerances in the design and operation of the ultra-magnet, the use of mercury may be foregone.

It should be noted that it was later found, empirically, that the super-dielectrics performed much better than expected. This information can be found in the document describing magnetic propulsion. This means that 100,000 rpm is not likely required, something more on the order of <1000 rpm may be possible given the experimental results. This will drastically reduce the friction and drag on the discs from the mercury. Nevertheless, a mercury-free design does have some advantages and disadvantages.

Alternative to the Slip Joint Fluid

While using mercury as a slip joint fluid is expected to be useful in the present devices and methods, it may be desirable to forgo the use of mercury or another conductive slip joint fluid altogether for any number of reasons.

The electrodes, especially those used in the MUMs can be manufactured to exceedingly high tolerances. Concerning the MUMs, the disc electrodes can be manufactured to near nanometer tolerances, including flatness and parallelism, using the techniques described previously.

After the disc electrodes are manufactured the super-dielectric matrix can be deposited onto the electrodes, also in nanometer scale exactness. A technique common in MEMs fabrication known as grayscale etching [18] can afterwards be used to etch curved surfaces into the super-dielectric matrix material, as shown in figure 38. In figure 38, these curved surfaces are partial spheres, though nearly any sag profile can be etched into the matrix material. The profiles in figure 38 are greatly exaggerated to make the concept clear. In reality, the curved surfaces are only slightly raised from the base matrix profile. This allows for a point contact between the matrix material and the secondary electrode as shown in figure 38b. The super-dielectric matrix material is often made of very hard materials such as metal oxides or ceramics, such as alumina, for example. Additionally, these ceramic or ceramic like materials often have low coefficients of friction. In this way the dielectric matrix material sets the spacing between the oppositely charged electrodes as well as providing for a rotational mechanism. The matrix material is firmly attached to the bottom electrode and the patterned point contacts come into contact with the top electrode. Additionally, a lubricating fluid such as silicone oil or fluorocarbon oils or any number of other lubricating liquids may be applied in the dead space left by the grayscale etching of the matrix material, if desired.

Alternative to the Slip Joint Fluid

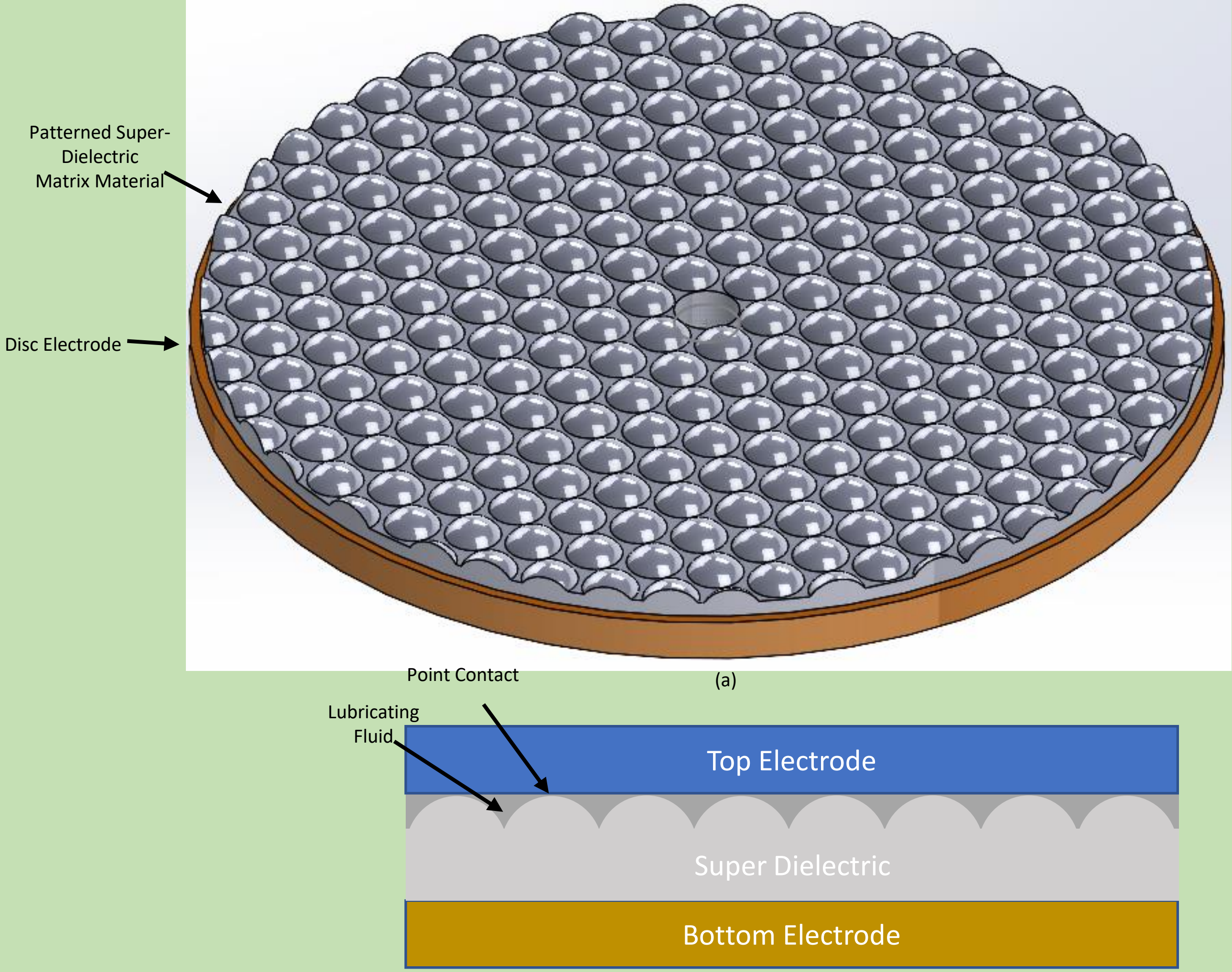

Figure 38. Schematic concept of the patterned dielectric acting as the slip joint. The point contacts slide on the top electrode providing both kinematic alignment spacing and kinematic motion for rotation.

Alternative to the Slip Joint Fluid

The disc electrodes can be counter-rotated, or singly rotated, with the point contacts providing the area of slippage between the two electrodes. Comparing at the same rotational speeds, this technique has only nominally less performance than the mercury slip joint fluid method described previously. Simulation shows up to 90% or more the performance of the mercury design is achievable, even with the assumption the mercury experiences full slip at the SD-mercury interface. Figure 39 shows an electrostatic simulation of a super-dielectric layer that has undergone patterning. Even in this exaggerated profile patterning, the charge storing ability of the patterned design is nearly 30% of the non-pattered, full layer. A 15-micron sag is shown in figure 39. However, submicron or even sub-100 nm sags are achievable with grayscale etching methods. As a reminder, the strength of the magnetic field achievable is directly proportional to the charge stored on the electrodes and the rotational speed achievable of those electrodes. Very little performance loss can be achieved with a ‘hard’ spacing, i.e., forgoing of the conductive fluid slip-joint and using the patterned super-dielectric layer-top electrode interface as the slip surface.

Alternative to the Slip Joint Fluid

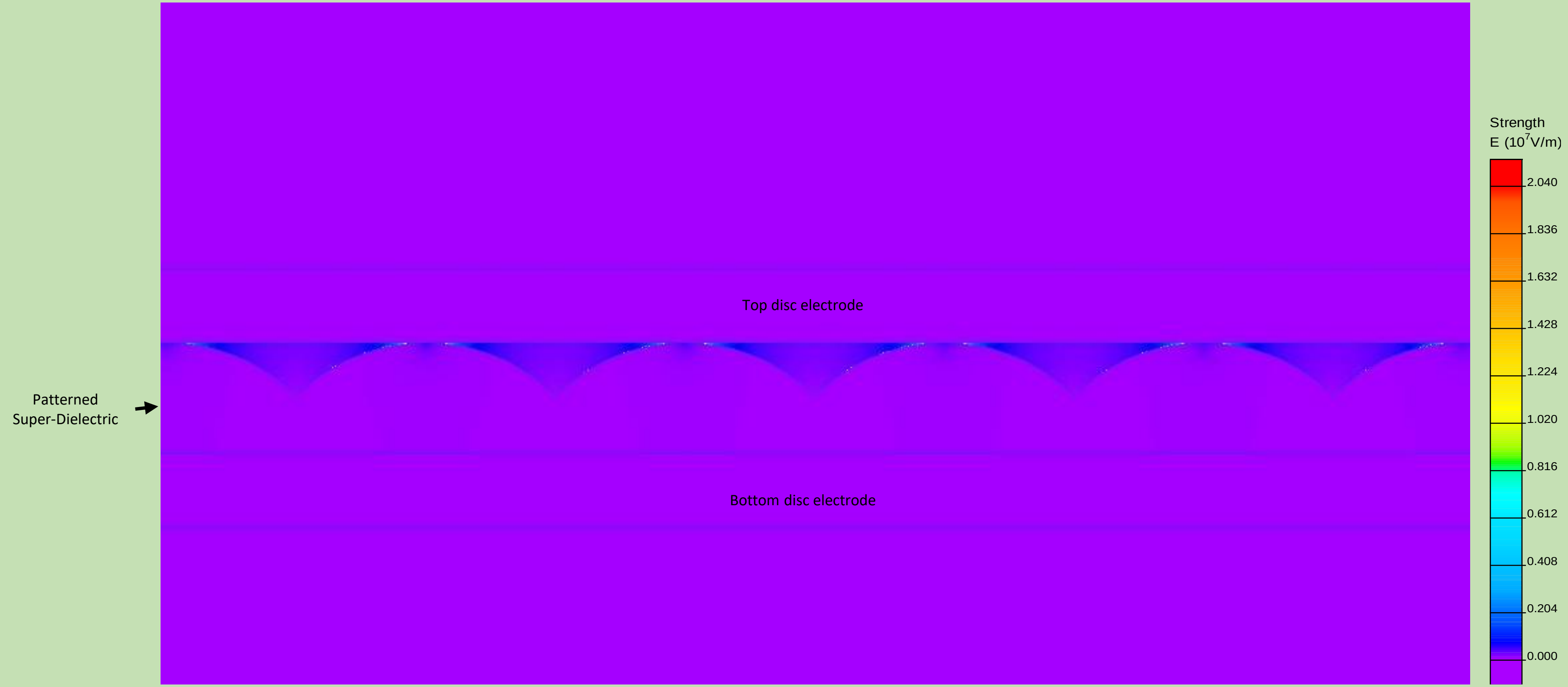

Figure 39 (continued). Electrostatic simulation of a 1.0 cm disc with a 30 micron thick dielectric patterned layer between and a 2 V potential applied between the electrodes. Equipotential lines and field strength are shown. The patterned layer (round profiles) are exaggerated so they can be clearly seen, here a 15 micron sag is shown, however sub micron sags are achievable.

Mercury-less Design

The friction between two sliding surfaces is known from Amonton’s Law of Friction to be

$F_{friction} = \mu_k N$ (14).

where μ_k is the coefficient of kinetic friction, and *N* is the normal force between the two surfaces.

The differential torque on the discs due to rotational friction can be stated as,

$$d\tau = r\, F_{friction} = r\mu_k dN = r\mu_k N(r,\varphi)\, rdrd\varphi$$

The frictional power loss may be expressed as,

$$dP_{friction} = \omega d\tau = \omega\mu_k r^2 N(r,\varphi)drd\varphi$$

$P_{friction} = \omega\mu_k \int_{\varphi_1}^{\varphi_2}\int_{R_1}^{R_2} N(r,\varphi)\, r^2\, drd\varphi$ (15)

, if N varies (non-uniform contact).

Mercury-less Design

$$P_{friction} = \frac{2\pi}{3}\omega\, \mu_k\, N(R_2^3 - R_1^3) \qquad (16)$$

, if N is uniform. ω is the relative angular velocity between the two discs, τ is the torque on the discs due to friction.

It is well known the friction force is independent of the contact area between the two surface, as is evidenced by equation 14. However, equation 14 is an approximation of the true frictional force. Friction is caused by inter-molecular forces. If the surfaces are smooth and flat, to the order of one nanometer, and in close contact, also to the order of one nanometer, the intermolecular forces may cause the two surfaces to strongly adhere to one another [17], a process known as optical contacting. The dimpling process ensures the optical contacting process does not take place. It should be understood that the super-dielectric may be flat and the converse electrode dimpled, whichever provides for easier implementation and operation. It may not always be necessary to dimple the surfaces as the super-dielectric matrix itself may provide sufficient surface roughness to prevent optical contacting, as the super-dielectric matrix contains porous structures much larger than one nanometer. The dimpling is accomplished through a MEMs fabrication process known as grayscale etching or grayscale lithography [18]. A potential method that negates the need for grayscale patterning, i.e., dimpling, will be discussed shortly, though both techniques may be used in tandem.

Stresses on the Discs

The normal force, N, in equation 14 warrants attention as this is the primary driver for the frictional force the spinning discs may experience during operation. The discs, containing large oppositely polarized electric charges, may experience a large electrostatic attraction, making N large if unmanaged. A Quickfield^{TM} FEM simulation, figure 40, of this electrostatic attraction, estimates the electrostatic pressure between the two plates with d = 2 microns, ΔV = 2 volts to be 4.4 GPa when fully charged; Analytically, the electrostatic force between two charged, flat capacitor plate electrodes is derived to be [35], ignoring fringe fields

$$F_C = \frac{k\epsilon_0 A\,(\Delta V)^2}{2d^2} = \frac{k\epsilon_0 \pi R^2 (\Delta V)^2}{2d^2} \qquad (17)$$

where A is the area of the plates, which gives an electrostatic pressure of

$$P_C = \frac{k\epsilon_0 (\Delta V)^2}{2d^2} \qquad (18).$$

Solving equation 18 for the system described also gives a result of 4.4 GPa, in exact agreement with simulation. These forces act perpendicular to the plane of the discs, i.e., pulling the discs towards one another.

Mercury-less Design

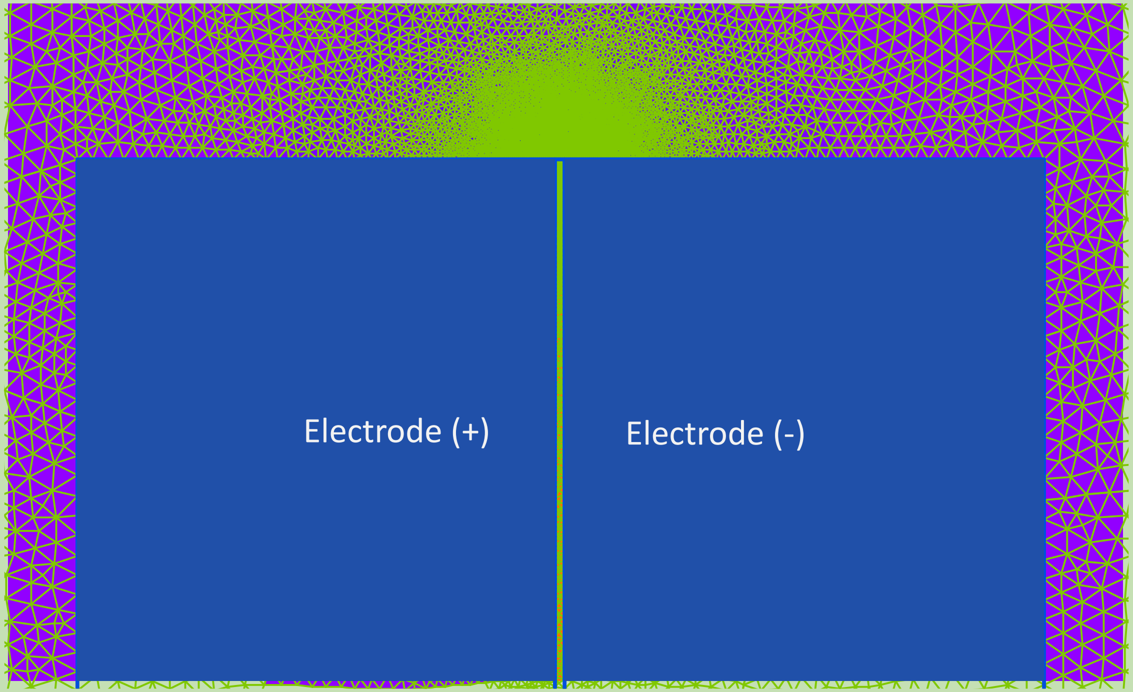

Figure 40. Quickfield^{TM} simulation of electrostatic pressure between the DSC plates; d = 2 microns, ΔV = 2 volts, R = 1 meter . Electrostatic pressure = 4.4 GPa.

Stresses on the Discs

The electromagnetic stresses at any point in the system can be calculated by the Maxwell Stress Tensor [45,46],

$$T_{ij} \equiv \epsilon\left(E_i E_j - \tfrac{1}{2}\delta_{ij}E^2\right) + \tfrac{1}{\mu}\left(B_i B_j - \tfrac{1}{2}\delta_{ij}B^2\right) \qquad (19)$$

where T_{ij} are the *i-th* and *j-th* components of the Maxwell Stress Tensor, $\overleftrightarrow{T}$. Here *i* and *j* represent the basis vectors in three-dimensional space, for cartesian coordinates $\hat{x}$ = 1, $\hat{y}$ = 2, $\hat{z}$ = 3. E_i and E_j are the components of the electric field vector in the *i*th and *j*th direction, similarly, B_i and B_j are the components of the magnetic field vector in the *i*th and *j*th direction. δ_{ij} is the Kronecker delta function.

The divergence of $\overleftrightarrow{T}$ yields the following equation [5,6];

$$\nabla \cdot \overleftrightarrow{T} = \tilde{F} + \epsilon\mu \frac{\partial \vec{S}}{\partial t} \qquad (20)$$

where $\tilde{F}$ is the force density and $\vec{S}$ is the familiar Poynting vector, $\vec{S} = \vec{E} \times \vec{H}$. It is worth noting in the analyses, it is assumed the system is running at steady-state to show the steady state performance of the system, therefore, the time derivative of the Poynting vector term on the right is not expected to contribute to the force calculation. This term would contribute on power up or power down of the system, otherwise the time derivative is zero. Taking the divergence of a tensor lowers its order by one, therefore the long vector equation version of equation can be written as, after solving for the force vector and writing purely in terms of *E* and *B*;

$$\tilde{F} = \epsilon\left[(\nabla \cdot \vec{E})\vec{E} + (\vec{E} \cdot \nabla)\vec{E}\right] + \tfrac{1}{\mu}\left[(\nabla \cdot \vec{B})\vec{B} + (\vec{B} \cdot \nabla)\vec{B}\right] - \tfrac{1}{2}\nabla\left(\epsilon E^2 + \tfrac{1}{\mu}B^2\right) - \epsilon\frac{\partial(\vec{E}\times\vec{B})}{\partial t} \qquad (21)$$

Stresses on the Discs

Similarly, the surface force density $\vec{\mathrm{F}}_s$(N/m^2) on the disc resulting from the effective current can be expressed as

$$\vec{\mathrm{F}}_s(r,\varphi) = \vec{K}(r,\varphi) \times \vec{B}_{int}(r,\varphi) \qquad (22)$$

Where $\vec{K}$ is the effective surface current density resulting from the rotating charges and $\vec{B}_{int}$ is the total magnetic field experienced by the disc, both any external fields and the fields generated by the device, i.e., the total magnetic field inside the device. A surface current density is used because in the preferred embodiment a super strong, non-conductive disc material with a thin-film metal coating is used. The electric charge is in a thin layer at the surface of the disc and not throughout the volume of the disc. In the calculation of the magnetic fields, using a current volume density vs a surface current density is inconsequential, however it is important in the case of calculating electromagnetic stresses on the discs and assembly structure that the forces are applied appropriately, being forces on the surfaces of the discs.

Additionally, the discs will experience mechanical stresses due to centrifugal forces. The centrifugal stress, σ_{cent}, on a spinning disc is given by [47]

$$\sigma_{cent} = \frac{R^2\rho}{3}\left(\frac{2\pi RPM}{60}\right)^2 \qquad (23)$$

Material Strength Considerations

Gigapascals of pressure is an immense amount of pressure which would likely crush any structure or device made of typical materials such as aluminum or steel. To this end, more exotic materials should be employed in the construction of the ultra-magnet system. Table 10 lists some candidate materials with the necessary strength and are in existence today. The list of materials is by no means complete but demonstrates materials are available that can handle the pressures and forces the ultra-magnet system may generate internally. Graphene as well as aluminum and steel are listed for reference. The 2010 Nobel Prize in Physics was awarded to Andre Geim and Konstantin Novoselov for their work with graphene. It is widely believed that graphene will be the wonder material of the 21st century, ushering in new technologies , being highly conductive and stronger than diamond. Currently, lighter, stronger, more resilient materials are being researched by combining graphene with metals, epoxies, and polymers [19-26]. The point being that while the current implementation is expected to operate with currently attainable materials, the achievable performance of the ultra-magnet system may be limited by the mechanical strength of those materials. As new materials are pioneered and material strengths are pushed into new regimes, so may the capabilities of the proposed ultra-magnet system be expanded.

Material Strength Considerations

Material	**Compressive Strength (GPa)**	**Tensile Strength (GPa)**	**Young's Modulus (GPa)**	**Bulk Modulus (GPa)**	**Poisson Ratio**	**Thermal Expansion (ppm/deg K)**
Synthetic Diamond	110	1.2	1220	548	0.2	1.1
Synthetic Sapphire	2	0.4	400	240	0.29	4.5-9.0
Alumina	5.5	0.6	413	324	0.3	4.5-10.9
Silicon Carbide	1.4	1.6	137	176	0.37	7.9-11
Tungsten Carbide	6.8	0.5	686	680	0.22	4.4-7.1
Boron Carbide	5.6	0.5	472	271	0.21	3.2-9.4
Carbon Fiber	2.5	4.9	700	500	0.27	-0.38
Nickle-Graphene Matrix	-	1.1	-	222	-	-
Pure Graphene	500-1000	130	1040	500-1000	-	-8.0
Aluminum	*0.28*	*0.3*	*88.5*	*88*	*0.36*	*16-24*
Stainless Steel (316)	*0.3*	*0.6*	*205*	*205*	*0.27*	*15-18*

Table 10. List of super strong materials and some of their properties. Aluminum and stainless steel are included for reference. Dashes indicate data has not yet been published or is unknown. Ref [27-42]. The properties of carbon fiber and graphene can vary considerably based on the manufacturing process.

Reducing Rotational Friction

Materials are typically stronger under compressive loads than tensile loads. The shafts holding the discs may experience large forces. In one potential embodiment, figure 41a, the top disc shaft passes through the bottom disc. The top disc is attracted to the bottom disc due to electrostatic attraction. The bottom disc is affixed to a rigid, fixed support structure and does not rotate. The bottom disc is attracted to the top disc through the same electrostatic attraction. The load from the attraction of the top disc to the bottom disc is transferred through the shaft. In this configuration the shaft is now under compressive stress, a stronger state for most materials. The bottom disc being rigid, and stationary can be made as structurally strong as appropriate.

Reducing Rotational Friction

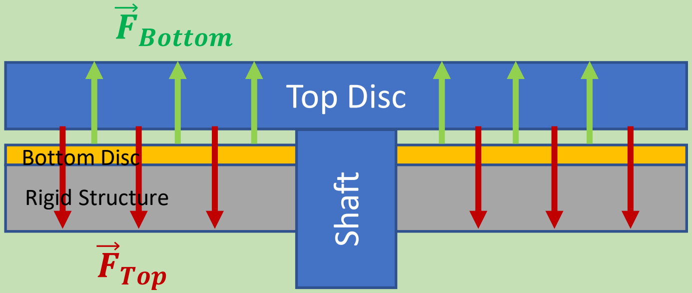

Figure 41a. Embodiment in which the shaft is put into compressive stress as opposed to tensile stress due to internal electrostatic pressure. Top disc rotates, bottom disc is stationary and attached to a rigid support structure (or the disc can be made as thick as appropriate for structural integrity).

Reducing Rotational Friction

It can be ascertained that the frictional force, equation 14, may be minimized or even eliminated by applying a force to the disc that counters the normal force, N, generated by the electromagnetic stresses. As pointed out, super strong materials may be necessary to handle such forces. In order to reduce the kinetic friction between the spinning discs, the normal force in equation 14 should be reduced. A reduction in the normal force can be additionally accomplished by applying a counter force through the shaft or shafts depending on the design of the ultra-magnet system. figure 41b shows a two-shaft system in which the shafts are in tensile stress. It should be clear that an upward force can be applied to the shaft in figure 41b to counter the attractive forces caused by the electrostatic pressure. In the latter case, the shaft is in compressive stress.

The separation forces used to reduce the frictional normal force can be very large. One potential way of producing these forces is through the use of thermal expansion/contraction. Platens at the base of the shafts, or the shafts themselves, can be made of super-strong materials, like those listed in table 10, and heated or cooled as necessary to produce expansion or contraction as appropriate. For instance, the shafts in figure 41b may be cooled in a controlled way to produce a contraction of the shafts. The shaft in figure 41a could similarly be heated to produce the appropriate expansion, assuming positive expansion coefficients. Depending on the materials used and the temperature change induced, the existing strains in the system, i.e., the strains causing the normal force, may be mitigated by exchanging deformation strain at the disc interface to axial deformation strain in the shaft; or the discs may experience a prescribed displacement if the discs are already in separation. These thermal expansions/contractions are capable of producing massive forces depending on the thermo-mechanical properties of the materials used. Another advantage of this method is the forces and displacements can be precisely controlled with accurate temperature controls.

Reducing Rotational Friction

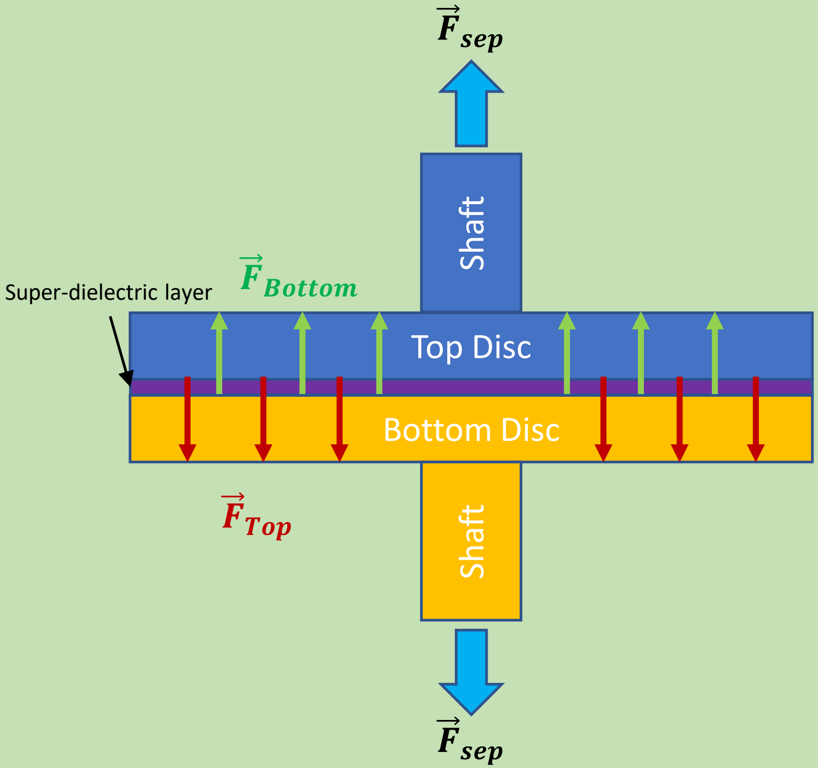

Figure 41b. Force, F_{sep}, applied to shafts to counter the normal force created by the forces, F_{Bottom} and F_{Top}, generated by the electrostatic pressure between the charged discs. One disc and shaft assembly may be fixed and a force solely exerted on the other disc and shaft assembly alternatively.

Reducing Rotational Friction

Presented are only two simple exemplary layouts, figure 41a and 41b. A great number of other configurations and mechanical designs can be realized.

It is instructive to estimate the rotational frictional losses. Equation 16 is only a rough approximation of the power loss due to rotational friction since the contact stresses throughout the discs are likely to be nonuniform. However, to get a rough approximation of the rotational friction power loss, for a 2-meter diameter disc rotating at 100,000 RPM, if the normal force can be reduced to 1000 newtons (225 lbs), and only the outer 1/3 of the discs are used for producing the magnetic field (a ring configuration), and a coefficient of kinetic friction of 0.03 is used, the rotational frictional power losses are estimated to be roughly 0.5 Megawatts. If the normal force can be reduced to 100 newtons, the power loss reduces to 50 kW. This illustrates the importance of reducing the normal force between the discs.

Since the rotational frictional power loss goes as the radius cubed, equation 16, it is worth running an approximation of the MUMs unit since it is a small diameter version of the ultra-magnet system. Due to the smaller diameter, the starting electrostatic force is 1/1,000,000th that of the MCU, if the dielectric layer thickness remains the same. If the normal force can be reduced to 100 N between each pair of discs in the MUM (the MUMs consists of a large stack of discs), the sliding frictional power loss is approximately 8 W for the whole MUMs unit described earlier. However, since the MUM's discs are small, resulting in a much smaller starting electrostatic force, and there are many discs, the force can be better distributed. It may be possible to lower the resultant normal force between disc pairs to a lower number, for instance a 10 N normal force per disc pair would result in a MUMs base unit only consuming about 0.8 watt of power to overcome rotational sliding friction losses. The choice of whether to use smaller radii MUMs or larger radii disc electrodes (e.g., MDUs) is a design choice, there are pros and cons to each.

Eliminating Sliding Friction

The reduction of the frictional normal force can be taken to the extreme; the discs can be separated. If the discs are separated beyond the range of the Van der Waals forces (~10 nm), the normal force may essentially drop to zero. This is a tricky proposition; first due to keeping such tight tolerances. Secondly, the electric circuit between the discs may be severed before disc separation takes place. If an air gap forms while the discs are still in electrical communication, i.e., part of a closed circuit, the super-capacitor may become a heterogenous capacitor with a super-dielectric layer and an air gap layer as the dielectric gap. The DSC may cease to be a supercapacitor at this point. The discs may be charged and then isolated (electrically disconnected). The discs now may retain their charge during the separation process. The charge on the discs is given by $Q = CV$. The voltage between the electrodes is $V = Q/C$. With Q now fixed, the voltage may rapidly increase as the discs are separated, since the capacitance, C, may drop rapidly as the discs are separated. The separation may be kept small, for example on the order of nanometers to tens of nanometers, or the voltage may rapidly increase to levels to which coronal discharge or field emission may take place. As a point of reference, if the super-dielectric were to be completely removed after the charge is fixed on the discs, or the discs were separated by an amount equal to the thickness of super-dielectric layer (for $k >> 1$), the voltage between the disc electrodes would increase by an amount equal to the dielectric constant of the super-dielectric, k. An air gap separation would be easier to achieve in a MUMs unit due to its smaller disc size and expected better tolerances, though still a difficult task. At the time of this writing, the exemplary super-dielectric contains ionic fluids [2, 3, 4]. In the near future, ionic fluids may not be necessary as graphene, graphene oxide, and other super-dielectric materials make progress. Without ionic fluid, the air in the formed gap may be evacuated, eliminating any potential air molecule drag on the spinning discs in the formed gap as well. Additionally, if the ionic fluid could be hermetically sealed in the matrix and its super-dielectric properties retained the air could also be evacuated, further reducing dissipative losses.

Manufacture of the Electrodes

Due to the intrinsic electromagnetic stresses of the system and the centrifugal forces of rotation, the discs may strain under operation. The discs may be premanufactured to compensate for the strain/distortion they may experience when stressed such that they may be as close to flat as possible under operation. This may help in ensuring a more uniform and controllable reduction of the normal force, N. Figure 42 shows the simulated pre-manufacture shape of the discs appropriate to compensate for the intrinsic electromagnetic forces of the system; centrifugal forces are not included here. The blue outline is the discs as they should be manufactured; exaggerated scale. The solid models are as under operation.

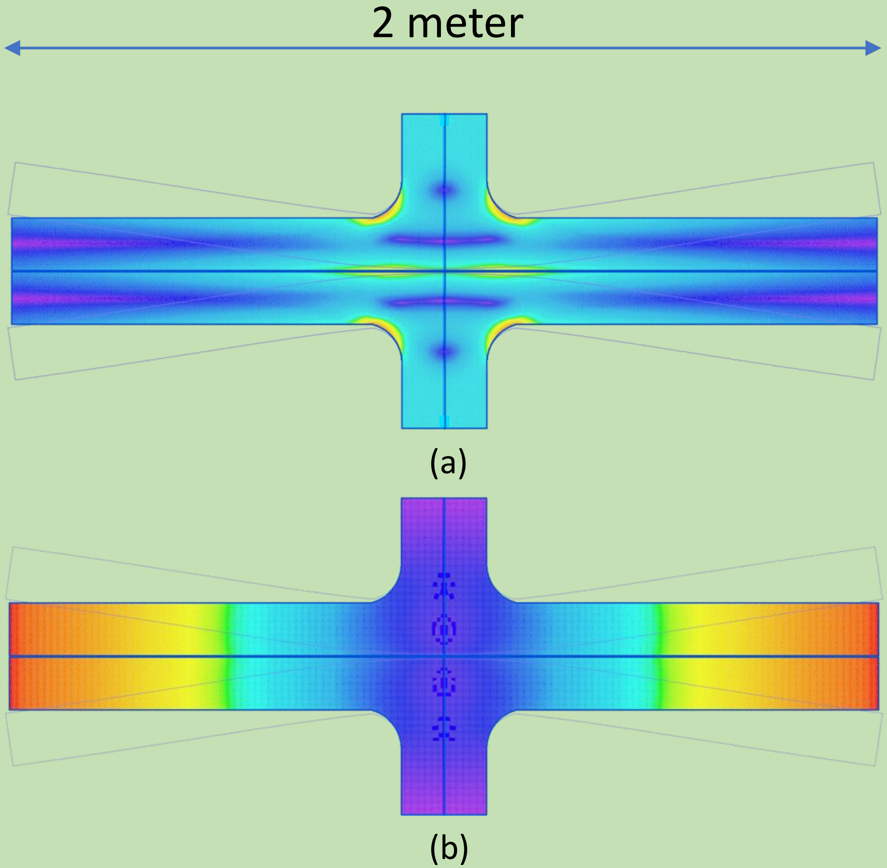

(a)

(b)

Figure 42. Discs may be premanufactured so that they are flat under operational stresses. Blue outline are profiles of how discs should be manufactured. Solid are discs' shape under operation. Not to scale. (a) stress profile (Tresca) on discs, (b) displacement from nominal profile. Electrostatic Pressure deformation only. QuickField^{TM}.

Manufacture of the Electrodes

Figure 42 shows a two-electrode system which creates a net moment arm on the electrodes due to the electromagnetic stresses which further creates a bending stress on the discs. A configuration can also be built where an electrode is charged on both sides much like that of figure 17 or the MUMs configuration previously described, figure 25. In this situation, the electrode experiences a balancing force resulting in a net zero electrostatic force from the electrostatic pressure, see figure 43. This eliminates the moment arm which previously created a bending force on the electrodes. The electrode will still experience some deformation from the electrostatic pressure as shown in figure 43 and may be premanufactured so that this deformation is accounted for such that the electrode is flat under operation and at an acceptable thickness. The area of the disc electrode close to the shaft need not be coated and or participate in the production of the magnetic field. The exclusion of this area will have minimal impact on the strength of the magnetic field produced due to fact that this deformation is close to the inner radius of the disc and the inner radius contributes little to the overall effective current, see figure 23a. The final endcap electrodes on either side of the device assembly can be made thick and rigid so as to experience minimal deformation and provide rigidity to the system, such as in figure 25 where the endcaps are much thicker than the discs themselves; with the endcaps being one millimeter in thickness and the discs being in practice tens to a hundred microns in thickness. Also, the endcaps can be made as thick as needed to provide the appropriate rigidity, see termination caps later.

Because the electrodes are largely naturally flat in this configuration, the lowering of the normal force and/or the separation of the discs previously discussed can additionally be achieved by thermal expansion or shrinkage of the discs by controlling the temperature of the discs during manufacturing and operation. As can be seen in figure 43, the electromagnetic attraction between the disc electrodes causes the disc to expand in the axial direction. In an embodiment of this configuration, the disc electrodes would start out by being close to being in physical contact, but slightly separated. The disc electrodes could then be heated, assuming a positive thermal expansion coefficient material, causing the electrodes to expand, therefore reducing the gap between electrodes. The charge flowing onto the discs may be monitored and when there is a sudden rise in the current flowing onto the discs this is an indication the system is going from a regular capacitor to a super-capacitor. This transition is an indication the discs are in extremely close proximity, sub-100 nm gap between the dielectric layer and the opposite electrode. The discs will then naturally expand towards one another due to the electric charge they now contain and the resulting electrostatic pressure; the electrodes may come into contact. If the discs come into contact or the normal force is unacceptably high, the discs can then be lowered in temperature to balance this electromagnetic expansion, thus reducing or eliminating the normal force in equation 16. This method, of course, can be used in conjunction with the thermal expansion controls discussed earlier on the shafts and/or a platen. Due to the desire to have a uniform thermal profile on the discs for this process, isotopically pure monocrystalline synthetic C^{12} diamond is an ideal material, as it has a thermal conductivity of 3320 W/m-K [43], more than eight times more thermally conductive than copper, ensuring a highly uniform thermal profile. Even isotopically impure synthetic diamond can have thermal conductivities of 2000 W/m-K [44]. Diamond is also mechanically very strong making it an ideal material for construction of the disc electrodes though other materials may be used.

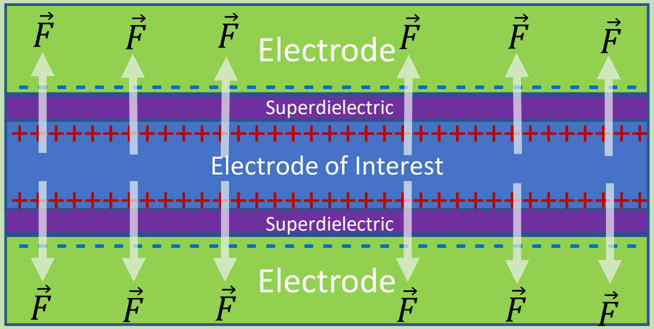

(a)

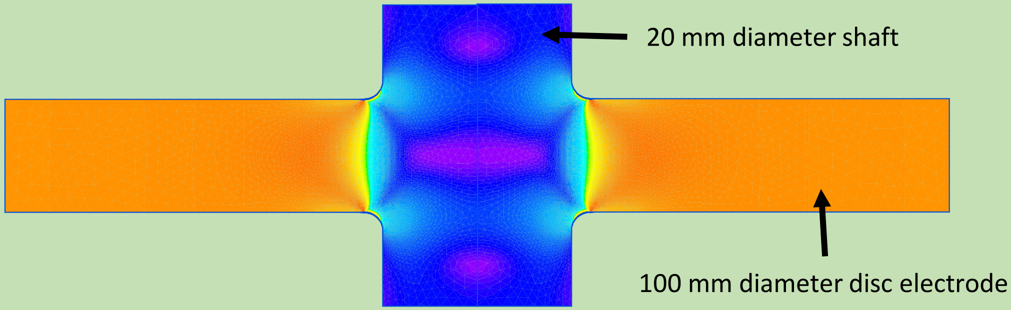

(b)

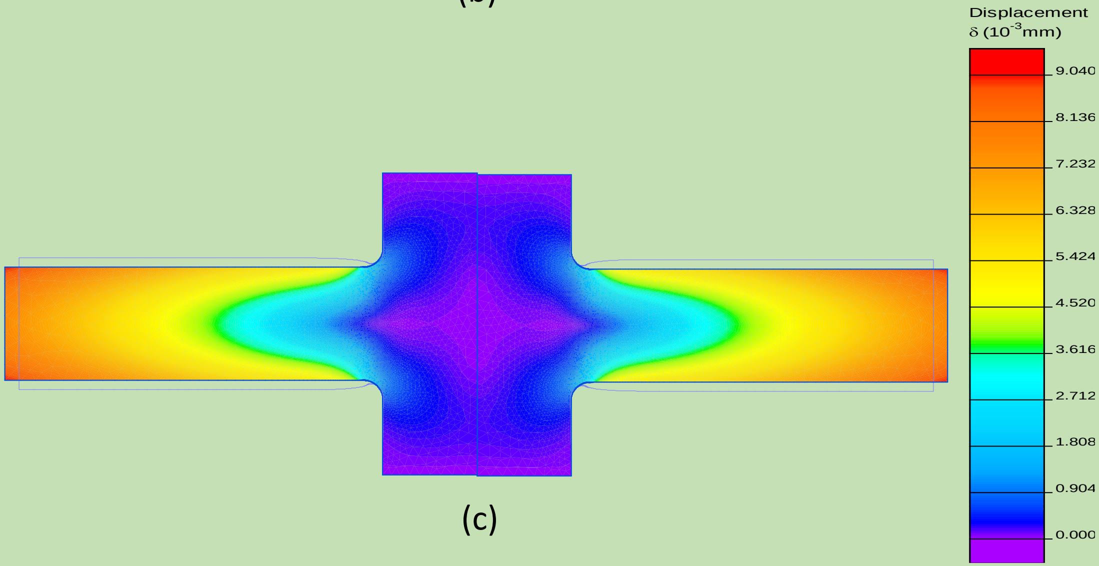

(c)

Figure 43. (a) Disc electrode is charged on both sides and is sandwiched between two oppositely charged electrodes. The electrode of interest experiences a balanced outward electromagnetic force due to the electrostatic pressure. (b) Simulated stress profile (Tresca) of the electrode of interest under operation. (c) Simulated displacement for the electrode of interest from (a) of a modified MUMs device electrode with a 2 cm inner shaft; disc and shaft constructed of synthetic diamond. The blue outline is the deformation of the disc under operation due to electrostatic pressure; not to scale. QuickField™.

Electromagnetic-Mechanical Strain of the MUMs

It is instructive to examine the electromagnetic-mechanical strain for a device described herein in more detail. A comprehensive simulation of the stresses and strain on a MUM device was undertaken. Figure 44 shows the displacement strains experienced by a MUM device similar to figure 25, but with the inner and outer shaft configuration of figure 17. The device consists of 10 mm diameter sapphire inner discs of 50-micron thickness attached to a 1 mm diameter diamond inner shaft with diamond endcaps and a sapphire outside casing, also known as the outer cylinder. The exemplary MUM operates with a $k = 1 \times 10^9$, voltage = 2 V, super-dielectric thickness = 2 microns, and rotational speed of 100,000 RPM. Simulated is a mercury-less design where the outer discs are 50 um thick diamond (not shown in figure 44). The forces simulated in figure 44 include the electrostatic pressure between discs, the internal magnetic stresses on the device (equation 22) , and the centrifugal stresses the discs experience due to rotation (equation 23). This configuration produces a magnetic field of approximately 50 Tesla. The discs are not charged until greater than two-millimeter radius; keeping electromagnetic stress deformations of the discs far from their attach point to the shaft which could result in unwanted tip/tilt distortions.

The electrostatic pressure causes the discs to grow slightly in width which causes the discs to shrink in radius. Due to the largely axial direction of the internal magnetic fields (figure 45), the magneto-mechanical forces create a radial stress on the disc (via equation 22), the centrifugal forces also create a radial force on the discs (via equation 22), both causing the discs to increase their radius slightly through radial strain.

The discs themselves experience approximately a 300-nanometer axial deformation. The approximately one-micron axial displacement shown in figure 44a is primarily due to a ~350 nanometer flexure of the inner shaft, resulting from magneto-mechanical and centrifugal forces on the discs which then act on the shaft, ultimately resulting in a slight tip of the edge discs, figure 44a.

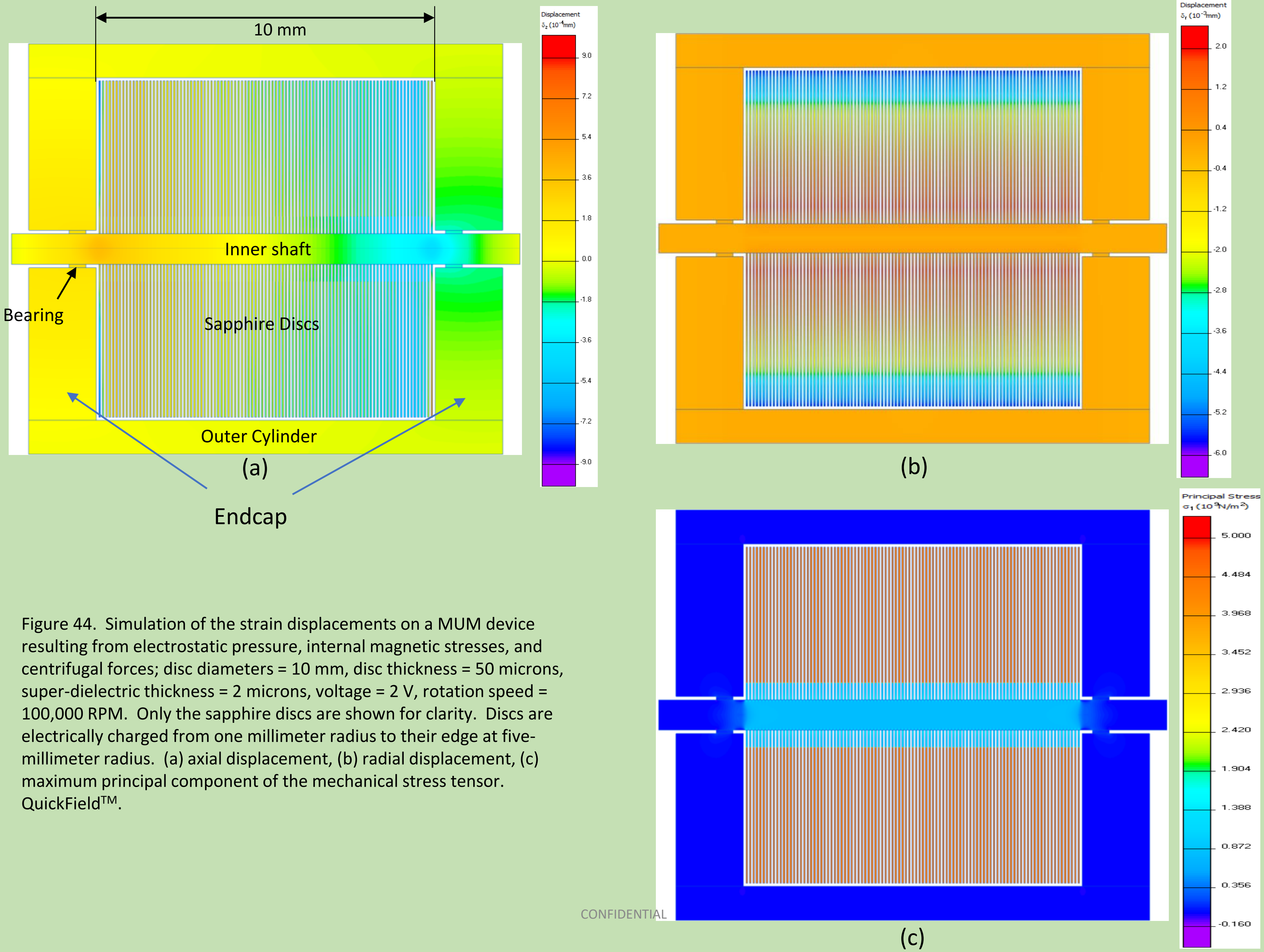

Figure 44. Simulation of the strain displacements on a MUM device resulting from electrostatic pressure, internal magnetic stresses, and centrifugal forces; disc diameters = 10 mm, disc thickness = 50 microns, super-dielectric thickness = 2 microns, voltage = 2 V, rotation speed = 100,000 RPM. Only the sapphire discs are shown for clarity. Discs are electrically charged from one millimeter radius to their edge at five-millimeter radius. (a) axial displacement, (b) radial displacement, (c) maximum principal component of the mechanical stress tensor. QuickField^{TM}.

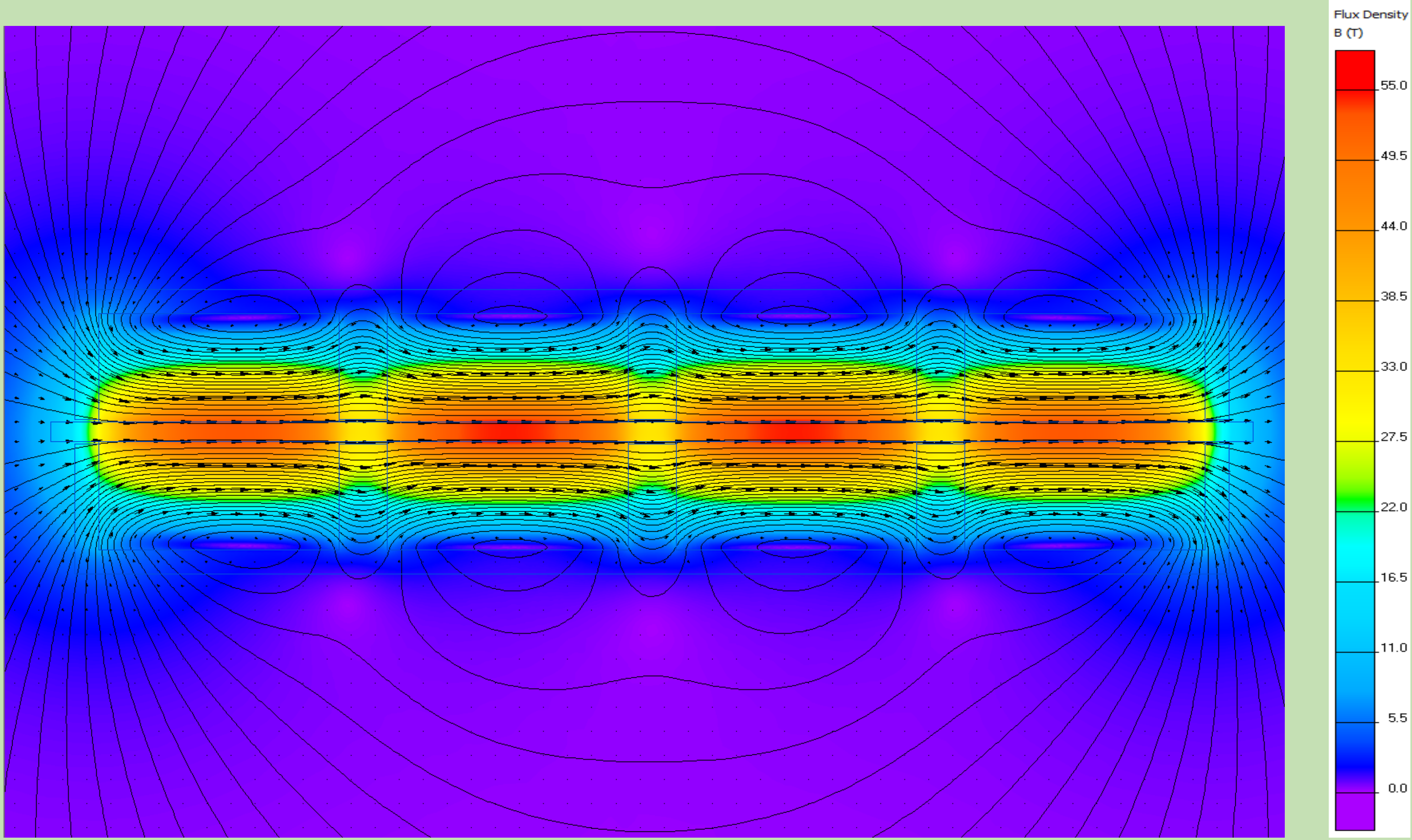

Figure 45. Four MUM units attached in series. The magnetic field inside the MUM assembly is largely axial in direction. QuickField^{TM}.

Electromagnetic-Mechanical Strain of the MUMs

In the stress/strain analysis of figure 44, the outside of the endcaps did not have a force applied to them. This was to unconfound the strains/displacements experienced by the inner discs and inner shaft from those experienced by the MUM body and outer discs. The only mechanical communication between the inner assembly, i.e., the inner shaft and the inner discs is through the bearings. The bearings are not meant to be a large load bearing member, only to keep the inner shaft centered, therefore the inner assembly and the outer assembly, i.e., endcaps, outer discs, and outer cylinder, largely act independently of one another.

Figure 46 shows the strain deformations on the outer discs, endcaps, outer shaft, and outer cylinder portion of the MUMs under operation. The discs themselves experience less than a 300 nm axial distortion and less than a two-micron radial shrinkage due to the electromagnetic stresses and centrifugal forces. The discs are forced outward due to magneto-mechanical forces and to a lesser degree centrifugal forces. These forces cause the outer cylinder to flex slightly which causes the discs close to the ends of the stack to bend inward slightly, the worst case being approximately ten microns from base to tip (figure 46). Several actions can be undertaken to mitigate the effects of the flexure of the discs. The discs, both inner and outer, can be premanufactured to account for this flexure so that the discs are flat or parallel when under operation. The only disadvantage to this method is the discs would not all be the same which makes assembly more difficult, having to keep track of which disc goes where in the stack assembly. Another mitigation includes the outer cylinder being freeform manufactured to be cylindrical when loaded; this allows the discs to all be the same. Additionally, the conductive slip joint fluid method can be employed which takes up the flexure tolerance of the discs in the fluid. The fourth alternative is to allow the discs to flex and press against their neighbors. The flexure distortion is localized to the outer discs, figure 46, and would result in a non-uniform contact in these localized areas. This non-uniform contact would result in wear in those areas and an overall higher friction but would be limited to those localized areas and its severity may be limited and acceptable.

In figure 44a, the forces largely act to balance the deformations as long as the disc is sandwiched between two other oppositely electrically charged elements. Physically, there must be two end elements that are unbalanced, i.e., only have one neighbor, which results in a large unbalanced force which may lead to large deformations in the device. In order to mitigate this effect, the outside of the endcaps can be coated and electrically charged similarly to the discs. The MUMs can then be linked in series. In this case the electrostatic pressure will force the MUMs together locking them into place. This transfers the force, due to electrostatic pressure, through the endcap to the next MUMs unit. It is not necessary for the endcaps to rotate relative to one another, in fact, it is desirable to have the endcaps of one MUMs locked to the endcap of the adjacent MUMs device; this is the function of the castellations shown in figure 25 but can be similarly accomplished by the electrostatic pressure locking the devices together. It should be apparent the castellations shown in figure 25 can also be used in conjunction with electrostatic locking as well. If there is no electric charge, then the endcaps do not electrostatically lock, and the MUMs may be separated freely in this case.

As many MUMs devices as are needed can be linked together in series in this way. The force symmetry is maintained throughout the chain until the end MUMs. The two end MUMs can then be capped with a larger structural element that is more readily able to handle the unbalanced force. This cap is named a termination cap. Figure 47 shows a deformation simulation of two MUMs in series with structural termination caps at the end. As can be seen, the caps absorb the unbalanced forces, keeping the operational core of the MUMs devices in a low distortion state.

While diamond and sapphire have been used in the construction of the analyzed device, other materials may be used such that mechanical strength requirements are met for the operational needs of the device. The diamond and sapphire order in these designs may also be inverted if in the assembly process, as described earlier, the heating and cooling of the components during assembly are reversed. Presented here is only one example of many possibilities.

The deformation strains on a MUM device have been analyzed with a fixed set of parameters (rotational speed, dielectric thickness, voltage, disc thickness and spacing, etc.). The stresses may be more or less depending on how hard the device is driven and the performance required from the device.

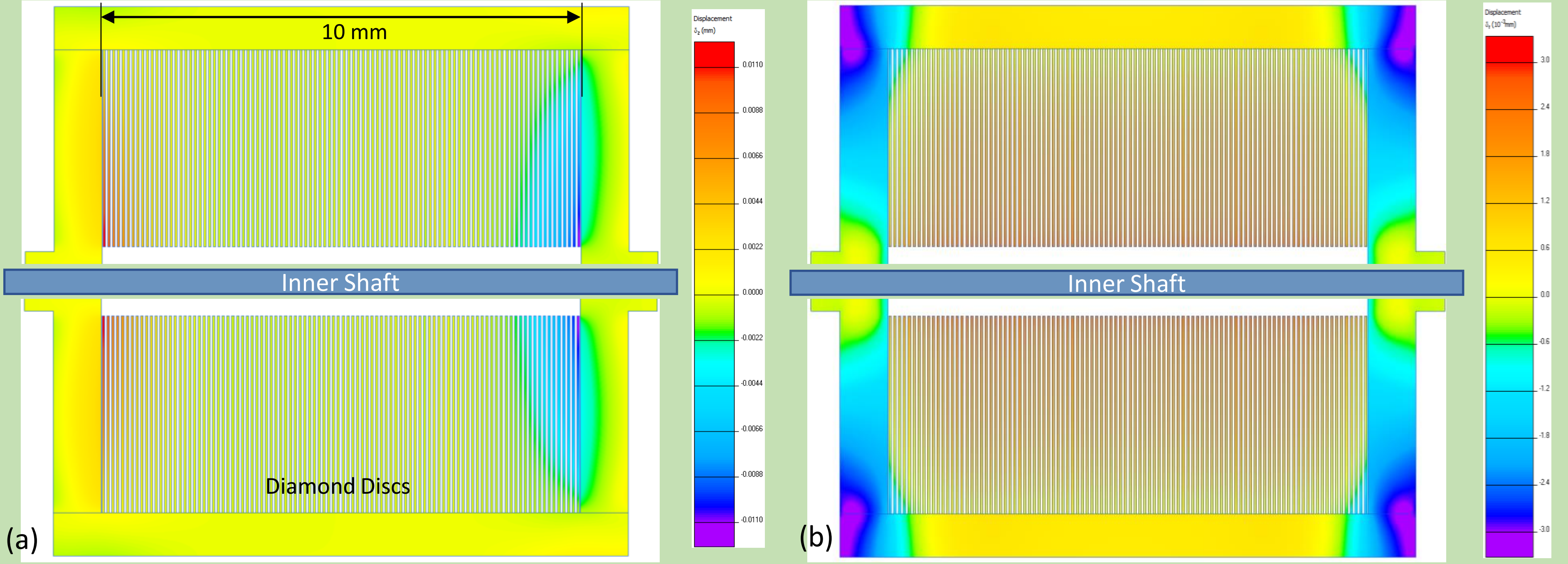

Figure 46. MUM body stress and flexure. Endcaps hold charge and are assumed to link to another MUM or a termination cap. 10 cm diameter discs, 10 cm stack of discs, dielectric spacing = 2 micron, voltage = 2 volts, rotation speed = 100,000 RPM. (a) axial displacement, (b) radial displacement, (c) (c) maximum principal component of the mechanical stress tensor. QuickField^{TM}.

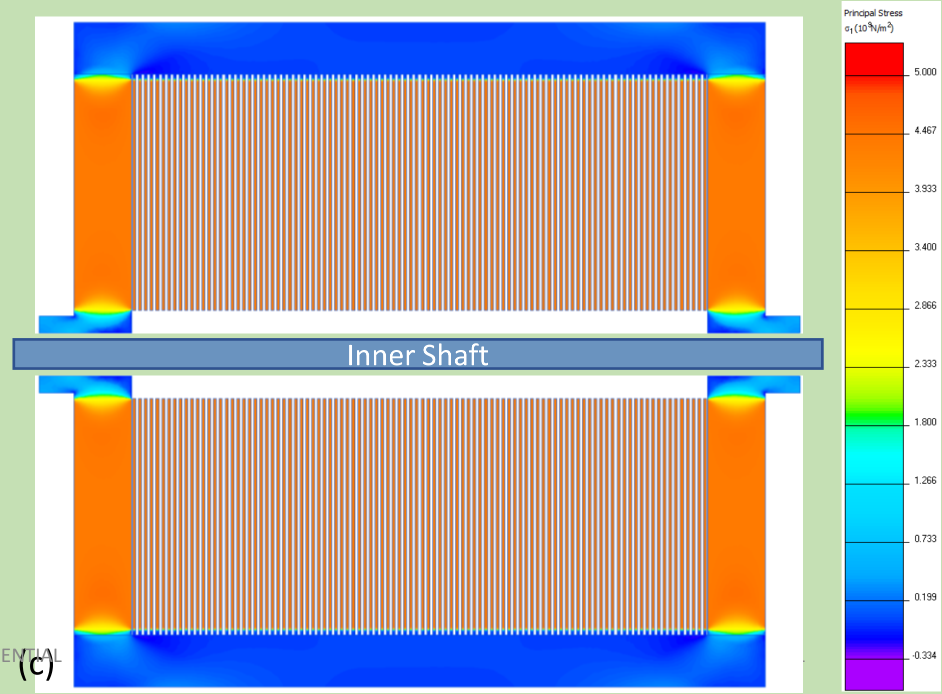

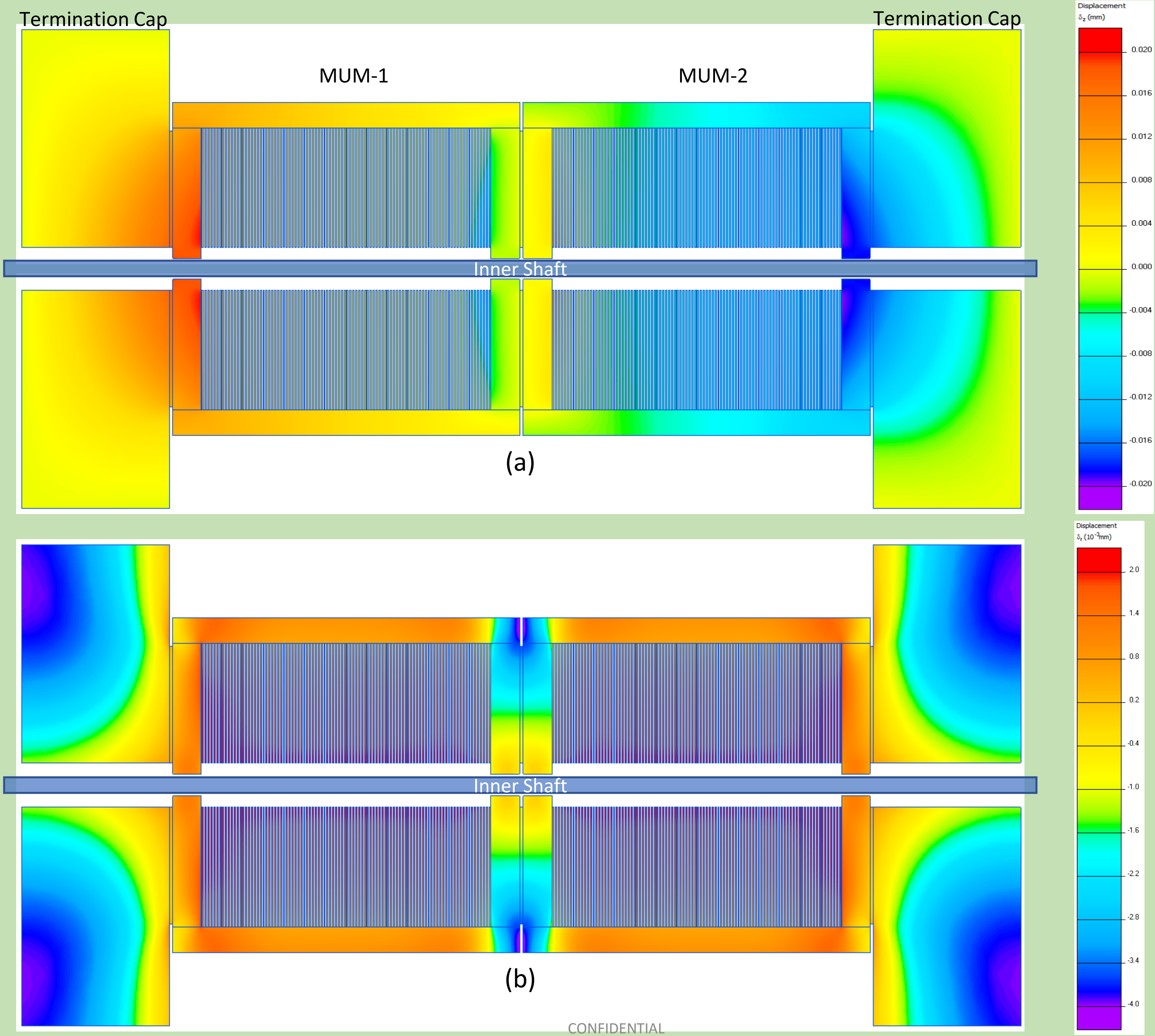

Figure 47. Operational deformation of a multi-MUM assembly with termination caps. As analyzed in figure 44 and 45. (a) axial deformation, (b) radial deformation.

Metallization Considerations

Finally, consideration must be paid to the strength of the metal adhesion to the electrodes. In most of the exemplary examples disclosed herein the electrodes are made of super strong, non-electrically conductive material. To make the electrodes capable of moving and holding electrical charge, the electrodes are coated with thin film metal coatings. In general, these metal films are captive, i.e., sandwiched between two rigid structures such as shown in figure 44a. The metal films transfer their stresses to the structures captivating them. Ideally, the electrodes would be very slightly separated in order to reduce or eliminate the normal force in equation 14 and 16 to near zero, thus reducing friction, wear, and dissipative power in the device to minimal values. In a full electrode separation case, the metal will bare the brunt of the electromagnetic stresses and the metal's adhesion becomes paramount.

Lei and Kumar [48] have shown that metal adhesion when the delamination force is normal to the thin film can be expressed as

$$\gamma = \frac{t}{2K}\sigma_f^2 \qquad (24)$$

where γ is the work of adhesion, K is the bulk modulus of the metal film material, t is the thickness of the metal film, and σ_f is the adhesion strength.

Strong adhesion can be achieved at a chemical level. Diamond is a carbon allotrope, therefore using metals that have high affinities for carbon can provide extreme adhesion strength, such as Aluminum, Copper, or Titanium. Guo, Qi, and Li have shown that titanium can have a work of adhesion to diamond up to 5.77 Joules/meter^2. With a 50 nm thick titanium film this translates into an adhesion strength of approximately 5.6 x 10^9 N/m^2. Similarly sapphire bonds well with metals that have an affinity for oxygen, such as chromium or aluminum. Since sapphire's chemical composition is Al_2O_3 which contains aluminum, it is possible to directly diffusion bond aluminum to sapphire [50, 51] which gives a bonding strength similar to that of the strength of the substrate material itself. Strong metal adhesion bonds can be obtained which allows for operation of the devices even with electrode separation.

Finally, it is worth noting that the super-dielectric layer itself does not hold free charge, but electric dipoles in its matrix, therefore the super-dielectric material experiences zero net electromagnetic forces as it has a net zero electric charge. Technically, from a Drude model perspective the dipoles will expand slightly due to the electric forces, but that expansion can be ignored due to the extremely small amount of that expansion at the molecular level, i.e., sub-angstroms, and in a lattice-less liquid as the exemplary super-dielectric is an ionic fluid.

Energy Storage Devices

It is readily apparent the devices described in the present application are capable of storing energy. Energy can be stored as electrostatic energy; as charge on the electrodes of the devices. Energy in electrostatic fields is described as

$$W_E = \frac{1}{2}CV^2 \quad , \qquad (25)$$

where W_E is the energy stored in the electrostatic field, C is the capacitance of the device, and V is the voltage applied to the device.

In addition to the electrostatic energy, energy is also stored in the magnetic fields generated by the devices. Energy stored in the magnetostatic fields is

$$W_B = \frac{1}{2}LI^2 \quad , \qquad (26)$$

where W_B is the energy stored in the magnetostatic field, L is the inductance of the device, and I is the effective current of the device. Alternatively, the magnetostatic energy density can be described as

$$U_B = \frac{B^2}{2\mu} \quad , \qquad (27)$$

where U_B is the magnetostatic energy density, B is the magnetic flux density, and μ is the magnetic permeability of the material the field exists in (in this case μ is assumed to be that of free space). The total magnetic energy stored can be calculated by integrating U_B over all space.

Energy Storage Devices

The approximate capacitances are easily calculated using the geometrical capacitances listed in figure 1. These equations ignore the fringe electric fields but are nonetheless accurate enough to give very good approximations to the energy stored as electric charge on the devices and thus the energy stored in the electric fields of the device.

The magnetic fields have been simulated and the total magnetic energy stored in the fields has been calculated using equation (10) integrated over a 100 meter diameter sphere centered on the devices in question. The magnetic field beyond this range has negligible contribution to the total energy and can be ignored.

Energy Storage Devices

MUM

Figure 48 shows the magnetic energy density plot for a 1 cm long x 1 cm diameter core MUM device with a 60 micron electrode spacing, dielectric constant k = 1 x 10^9, RPM = 100,000, super-dielectric layer thickness (SDt) = 2 microns, and voltage = 2 V. Table 10 shows the energy stored both in the electric field and magnetic field for a number of electrode spacings and dielectric thicknesses, all other parameters being same as in figure 48.

Individually, the MUM device is not overly impressive for energy storage, however, due to its compact size and stackability, a large number of MUMs can fit into a relatively small volume. For example, without the exostructure, approximately 575,000 MUMs can theoretically fit into a cube one meter on a side, the total MUM size including endcaps and outer casing, being 12 mm x 12 mm. Using the device shown in figure 48, the combined electric and magnetic field energy storage for a one cubic meter space equates to approximately 185 million joules of energy storage or about enough energy to power the average 2000 sq ft home for about 36 hours. This energy storage grows as the cube of the size of the overall device assembly, as an example a 10 meter x 10 meter x 10 meter cube of MUMs theoretically can store approximately 185 billion joules of energy or about three minutes of power output by the average nuclear power plant.

These values are for a mid-grade MUM base unit, as can be seen in Table 11, these numbers can be improved significantly by using a higher performance MUM.

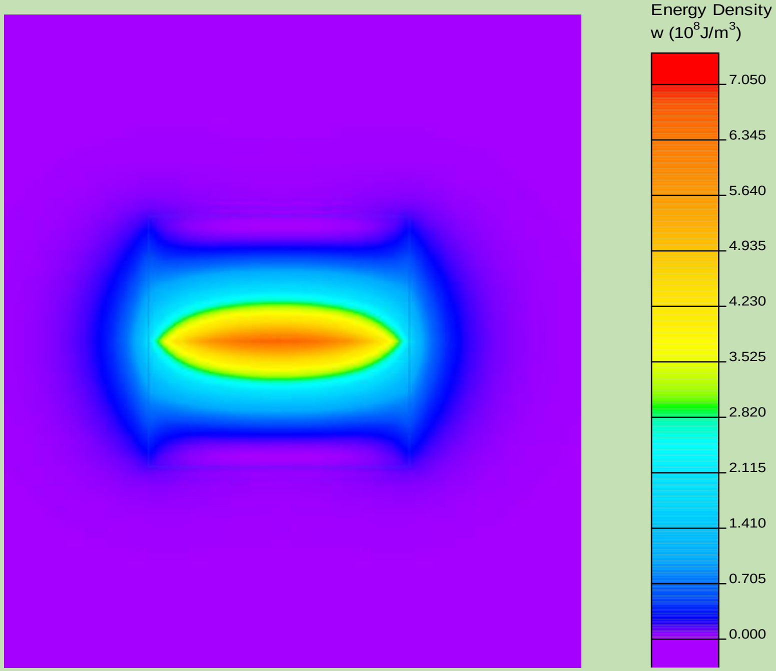

Figure 48. Magnetic Energy Density plot for a 1 cm long x 1 cm diameter MUM magnetic core. Electrode spacing = 60 microns; super-dielectric thickness (SDt) = 2 microns; RPM = 100,000; dielectric constant k = 1 x 10^9, voltage = 2 V. *Figure updated*

Electrode Spacing (um)	E-SDt (1 micron)	E-SDt (2 microns)	B-SDt (1 micron)	B-SDt (2 microns)
500	55.6	27.8	5.1	1.3
200	139.1	69.5	31.6	7.9
100	278.2	139.1	126.4	31.6
80	347.7	173.9	197.5	49.4
60	463.6	231.8	351.0	87.8
40	695.4	347.7	789.8	197.5
20	1390.8	695.4	3159.2	789.8
10	2781.6	1390.8	12637.0	3159.2

Table 11. Electric and Magnetic energy stored in MUM device (Joules). E-SDt (1 micron) is energy stored in the electric field with a 1 micron super-dielectric thickess layer, E-SDt (2 microns) is energy stored in the electric field with a 2 micron super-dielectric thickness, B-SDt (1 micron) is energy stored in the magnetic field with a 1 micron super-dielectric thickness layer, and B-SDt (2 microns) is energy stored in the magnetic field with a 2 micron super-dielectric thickness layer. The MUM unit described in the example in the text is highlighted.

Energy Storage Devices

MDU

Figure 49 shows the magnetic energy density plot for a 2 meter long x 1 meter diameter MDU device with a 1 centi-meter electrode spacing, dielectric constant k = 1 x 10^9, RPM = 100,000, super-dielectric layer thickness (SDt) = 5 microns, and voltage = 2 V. Table 12 shows the energy stored both in the electric field and magnetic field for a number of electrode spacings and dielectric thicknesses, all other parameters being the same as in figure 49.

As can be seen, due to the MDU's larger size and stronger magnetic fields (magnetic energy density goes as the magnetic field strength squared), the MDU devices can store immense energy in their magnetic fields, even more than the multi-MUM assemblies described previously. To wit, the MDU shown in figure 49 theoretically can store the energy equivalent to roughly two minutes of energy output of the average nuclear power plant despite its relatively small size. This example is for a relatively mid-tier MDU. In the extreme MDU example, a 1 micron super-dielectric layer thickness, with a 1.0 mm electrode spacing, an MDU 2 meters long x 1 meter in diameter can theoretically store 80 hours of energy output from a nuclear power plant; though there are a number of practical considerations for the construction and operation of such an extreme example.

It is also worth noting the energy stored in the magnetic fields dwarfs the energy stored in the electric fields for MDU and MCU units (with MCU units having very similar performance characteristics to the MDUs). Electric field energy storage is the most common and preferred method of energy storage today; little to no consideration has been given to using magnetic field energy storage.

The usefulness of such energy storage devices should be apparent; acting as power backup, power black out prevention, energy storage for intermittent power sources (such as wind or solar farms), and potentially remote power sources for vehicles, be they cars, trucks, ships, submarines, planes, trains, construction equipment, spacecraft, etc.).

The strength of the magnetic field is directly proportional to the rotational speed of the electrodes. Since the energy stored in the magnetic fields goes as the square of the magnetic field strength, equation 10, this implies the energy storage goes as the square of the rotational speed of the electrodes. Therefore, great attention to maximizing the rotational speed of the device electrodes is paramount. It should be obvious that relatively slow-moving turbines such as with windmills and the like can be geared to produce high rotational rates in the devices described herein.

Finally, while electrostatic energy storage devices, such as super-capacitors experience bleed off of charge over time, even when not in use, the magnetic energy storage devices presented herein will also lose energy over time due to dissipative forces such as friction of the bearings and fluid drag; or point contact friction if a design like that of figure 38 is used. These non-conservative force energy losses, i.e., frictional losses, can be made small in comparison to the amount of energy stored in the fields, thus the device can store energy for an extended period of time. The frictional forces will generate heat, this heat can be captured and turned back into rotational mechanical energy through a Stirling engine or similar heat reservoir device or devices that convert heat gradients into mechanical or electrical energy. The point being there will be some losses over time of the stored energy, however, these losses can be mitigated through clever design and energy management, thus, the useful energy storage period can be extended for any of the magnetic devices discussed herein once the original power source has been lost or removed.

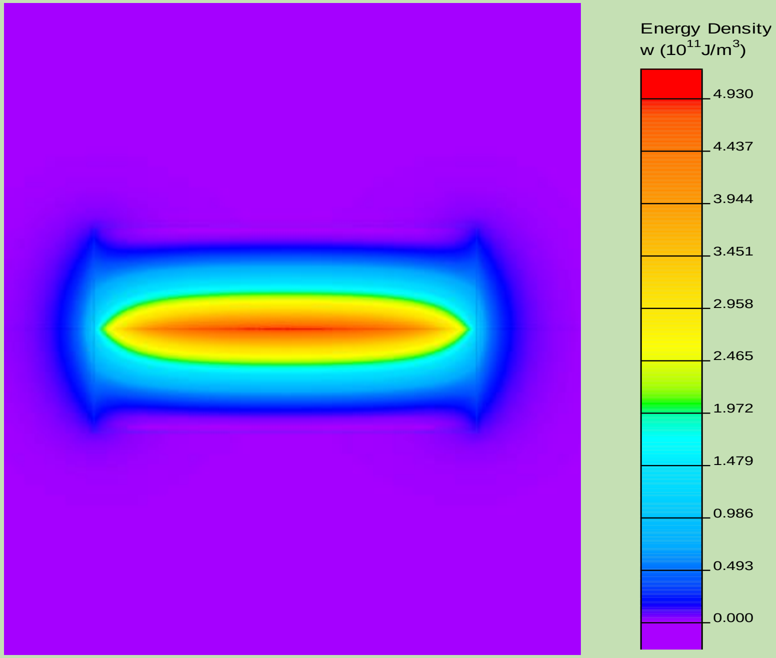

Figure 49. Magnetic Energy Density plot for a 2 meter long x 1 meter diameter MDU. Electrode spacing = 1 cm; super-dielectric thickness (SDt) = 5 microns; RPM = 100,000; dielectric constant k = 1 x 10^9, voltage = 2 V. *Figure updated*

Electrode Spacing (cm)	E-SDt (1 micron)	E-SDt (2 microns)	E-SDt (5 microns)	E-SDt (10 microns)	B-SDt (1 micron)	B-SDt (2 microns)	B-SDt (5 microns)	B-SDt (10 microns)
2	2.782E+06	1.391E+06	5.563E+05	2.782E+05	7.402E+11	1.851E+11	2.961E+10	7.402E+09
1.8	3.091E+06	1.545E+06	6.181E+05	3.091E+05	9.138E+11	2.285E+11	3.655E+10	9.138E+09
1.6	3.477E+06	1.739E+06	6.954E+05	3.477E+05	1.157E+12	2.891E+11	4.626E+10	1.157E+10
1.4	3.974E+06	1.987E+06	7.948E+05	3.974E+05	1.511E+12	3.777E+11	6.043E+10	1.511E+10
1.2	4.636E+06	2.318E+06	9.272E+05	4.636E+05	2.056E+12	5.140E+11	8.225E+10	2.056E+10
1	5.563E+06	2.782E+06	1.113E+06	5.563E+05	2.961E+12	7.402E+11	1.184E+11	2.961E+10
0.8	6.954E+06	3.477E+06	1.391E+06	6.954E+05	4.626E+12	1.157E+12	1.851E+11	4.626E+10
0.6	9.272E+06	4.636E+06	1.854E+06	9.272E+05	8.225E+12	2.056E+12	3.290E+11	8.225E+10
0.4	1.391E+07	6.954E+06	2.782E+06	1.391E+06	1.851E+13	4.626E+12	7.402E+11	1.851E+11
0.3	1.854E+07	9.272E+06	3.709E+06	1.854E+06	3.290E+13	8.225E+12	1.316E+12	3.290E+11
0.2	2.782E+07	1.391E+07	5.563E+06	2.782E+06	7.402E+13	1.851E+13	2.961E+12	7.402E+11
0.1	5.563E+07	2.782E+07	1.113E+07	5.563E+06	2.961E+14	7.402E+13	1.184E+13	2.961E+12

Table 12. Electric and Magnetic energy stored in MDU device (Joules). E-SDt represents energy stored in the electric field for the super-dielectric thickness indicated in parenthesis. B-SDt is the corresponding energy stored in the magnetic field of the device. The MDU described in the example in the text is highlighted.

Approximation of the Stated Performances

Tables 1, 2 ,3 ,4 ,5 ,6 ,8 and 9 show the peak magnetic field simulation results for a number of the designs described in the present application. Similarly, table 11 and 12 show electrostatic and magnetostatic energy storage potential of the described devices. It should be strongly pointed out that these are approximations and not exact values.

First, where magnetic fields are concerned in the data, these are magnetostatic finite-element method simulation results; which by their nature are approximations, though typically accurate depending on simulation mesh density and model convergence.

Secondly, the charge capacity, capacitance, of the electrodes was calculated using the equations from figure 1. These equations ignore the fringe electric fields that exist outside the electrode gaps, i.e., they only consider the fields between the two electrodes. This approximation was done for computational efficiency. The full charge capacity of the two oppositely polarized electrodes is given by

$$C = \frac{1}{(Voltage)^2} \iiint_V \vec{E} \cdot \vec{D} dV \qquad (28)$$

Where C is the capacitance, *Voltage* is the voltage potential between the two electrodes, $\vec{E}$ is the electric field strength and $\vec{D}$ is the electric displacement field. The dot product between $\vec{E}$ and $\vec{D}$ is integrated over all space, V. As an example of the difference, the capacitance for a MUM pair of electrodes 1.0 cm in diameter with a 10 micron super-dielectric gap with k = 1 x 10^9 is calculated to be about 0.06954 Farads using the approximate equation in figure 1, whereas when the full field is taken into account the capacitance is 0.06955 Farads. The difference is insignificant due to the vast bulk of the energy being stored in the field inside the super-dielectric between the electrodes. In fact, the small difference may just be rounding error. The equations from Figure 1 are significantly accurate and valid for the results given.

Thirdly, when using a conductive slip-joint fluid, the conductive fluid in the vicinity of the electrodes will hold a charge opposite to that the electrode. This charge will primarily be on the surface of the fluid in contact with the dielectric. While care has been taken to ensure the fluid does not stick to the electrode/super-dielectric, some momentum will inevitably be transferred to the conductive fluid at this boundary which will diminish the total effective current somewhat which in turn will diminish the net magnetic field somewhat. The super-dielectric fluid and fluid layers shown in figure 5 do not suffer this drawback, nor does the point contact slip design shown in figure 38, also known as the mercury-less design. The non-super dielectric fluid layer and point contact slip design designs may suffer from a small decreased charge capacity due to the gap between the electrodes not being fully filled with super-dielectric material. The super-dielectric fluid layer shown in figure 5 does not suffer the loss in charge capacity, however, such a fluid does not exist today, though it is likely it could be engineered. The bottom line is, the stated results are representative of what can be achieved with the present methods and devices but should be understood to be approximations.

References

The entire contents of each of the following references is incorporated by reference herein:

1. A new single/few-layered graphene oxide with a high dielectric constant of 106: contribution of defects and functional groups - RSC Advances (RSC Publishing)
2. Fromille, S.; Phillips, J. Super dielectric materials. Materials 2014, 7, 8197–8212.
3. Cortes, F.J.Q.; Phillips, J. Novel materials with effective super dielectric constants for energy storage. J. Electron. Mater. 2015, 44, 1367–1376.
4. Cortes, F.J.Q.; Phillips, Tube-Super Dielectric Materials: Electrostatic Capacitors with Energy Density Greater than 200 J cm3, Materials 2015, 8, 6208-6227.
5. Saadi, N.S., Hassan, L.B. & Karabacak, T. Metal oxide nanostructures by a simple hot water treatment. Sci Rep 7, 7158 (2017). https://doi.org/10.1038/s41598-017-07783-8
6. Bearing Super Technology:Ultra-High Speed|Products & Technology|NTN Global
7. CVD Diamond - FAQ (cvd-diamond.com)
8. HEM Sapphire Windows, Sapphire Optics & Sapphire Lenses – GTAT
9. V. Steinberg; Introduction to Micro-fluidics. SMR1670-10. The Abdus Salam International Centre for Theoretical Physics. August 2005.
10. Roman S. Voronov, Dimitrios V. Papavassiliou, and Lloyd L. Lee; Boundary slip and wetting properties of interfaces: Correlation of the contact angle with the slip length. The Journal of Chemical Physics 124, 204701 (2006); doi: 10.1063/1.2194019
11. Yingxi Zhu and Steve Granick; Rate-Dependent Slip of Newtonian Liquid at Smooth Surfaces. Physical Review Letters Volume 87, Number 9, 27 August 2001.
12. Rihard_thesis_2005_A2.pdf (utwente.nl)
13. Tungsten Disulfide (WS2) Low Friction Coating per AMS2530 (microsurfacecorp.com)
14. Polytetrafluoroethylene – Wikipedia

References

The entire contents of each of the following references is incorporated by reference herein:

27. White, Frank (2011). Fluid Mechanics. New York City, NY: McGraw-Hill. pp. 477–485.
28. Sommerfeld 1908, pp. 116–124. Sommerfeld, Arnold (1908). "Ein Beitrag zur hydrodynamischen Erkläerung der turbulenten Flüssigkeitsbewegüngen (A Contribution to Hydrodynamic Explanation of Turbulent Fluid Motions)" (PDF). International Congress of Mathematicians . 3: 116–124. Archived from the original (PDF) on 2016-11-15.
29. Optical Contacting: Changing the Interface of Optics. Chris Myatt, Nick Traggis and Kathy Li Dessau. Precision Photonics Corporation precisionphotonics.com. https://web.archive.org/web/20090331235008/http:/www.precisionphotonics.com/vitem_axpd.asp?id=16&itemtype=Technicalpapers
30. Waits, Christopher M.; Ghodssi, Reza; Dubey, Madan. Gray-Scale Lithography for MEMS Applications. Army Research Laboratory, Defense Technical Information Center. https://apps.dtic.mil/dtic/tr/fulltext/u2/a447924.pdf
31. Graphene and the Most Popular Advanced Alloys (azom.com). https://www.azom.com/article.aspx?ArticleID=18901
32. Anthony, S. (2013). Graphene used to make graphene-copper composite that’s 500 times stronger. https://www.extremetech.com/extreme/164961-graphene-used-to-make-graphene-copper-composite-thats-500-times-stronger
33. Processing of graphene/CNT-metal powder. Prashantha Kumar HG and Anthony Xavior M. Powder Technology, Alberto Adriano Cavalheiro, IntechOpen, DOI: 10.5772/intechopen.76897. https://www.intechopen.com/books/powder-technology/processing-of-graphene-cnt-metal-powder
34. First report on high entropy alloy nanoparticle decorated graphene. M. Y. Rekha, Nitin Mallik, and Chandan Srivastava. Scientific Reports 2018; 8: 8737. doi: 10.1038/s41598-018-27096-8. https://www.ncbi.nlm.nih.gov/pmc/articles/PMC5992158/
35. Bioinspired, graphene-enabled Ni composites with high strength and toughness. Yunya Zhang, Frederick M. Heim, Jamison L. Bartlett, Ningning Song, Dieter Isheim, and Xiaodong Li. Science Advances 31 May 2019: Vol. 5, no. 5, eaav5577. DOI: 10.1126/sciadv.aav5577. https://advances.sciencemag.org/content/5/5/eaav5577.full
36. Investigating aluminum alloy reinforced by graphene nanoflakes. S.J.Yan, S.L.Dai, X.Y.Zhang, C.Yang, Q.H.Hong, J.Z.Chen, and Z.M.Lin. Materials Science and Engineering. https://doi.org/10.1016/j.msea.2014.06.077. https://www.sciencedirect.com/science/article/abs/pii/S092150931400803X
37. Copper/graphene composites: a review. Paloma Hidalgo-Manrique, Xianzhang Lei, Ruoyu Xu, Mingyu Zhou, Ian A. Kinloch & Robert J. Young. Journal of Materials Science volume 54, pages12236–12289(2019). https://doi.org/10.1007/s10853-019-03703-5. https://link.springer.com/article/10.1007/s10853-019-03703-5#Sec43
38. Graphene in composites and polymers (firstgraphene.net). https://firstgraphene.net/graphene-in-composites-and-polymers/

References

The entire contents of each of the following references is incorporated by reference herein:

27. Diamond Properties (bris.ac.uk). http://www.chm.bris.ac.uk/motm/diamond/diamprop.htm
28. Sapphire Properties | Guild Optical Associates (guildoptics.com). https://www.guildoptics.com/sapphire-properties/sapphire-properties/
29. Properties: Alumina - Aluminium Oxide - Al2O3 - A Refractory Ceramic Oxide (azom.com). https://www.azom.com/properties.aspx?ArticleID=52
30. Properties: Silicon Carbide (SiC) Properties and Applications (azom.com). https://www.azom.com/properties.aspx?ArticleID=42#:~:text=Silicon%20Carbide%20%28SiC%29%20Properties%20and%20Applications%20%20,10%206%20psi%20%2023%20more%20rows%20
31. Properties: Tungsten Carbide - An Overview (azom.com). https://www.azom.com/properties.aspx?ArticleID=1203
32. Properties: Boron Carbide (B4C) - Properties and Information about Boron Carbide (azom.com). https://www.azom.com/properties.aspx?ArticleID=75
33. Bioinspired, graphene-enabled Ni composites with high strength and toughness. Yunya Zhang, Frederick M. Heim, Jamison L. Bartlett, Ningning Song, Dieter Isheim, and Xiaodong Li. Science Advances 31 May 2019: Vol. 5, no. 5, eaav5577. DOI: 10.1126/sciadv.aav5577.
34. A short review on mechanical properties of graphene reinforced metal matrix composites – ScienceDirect. https://www.sciencedirect.com/science/article/pii/S2238785419312852
35. Properties of Graphene – Graphenea. https://www.graphenea.com/pages/graphene-properties#.YJ3BjYeSmUl
36. Properties: Aluminum - Advantages and Properties of Aluminum (azom.com). https://www.azom.com/properties.aspx?ArticleID=1446#:~:text=Aluminum%20-%20Advantages%20and%20Properties%20of%20Aluminum%20,%20%2040.6106%20%2023%20more%20rows%20
37. Properties: Stainless Steel - Grade 316 (UNS S31600) (azom.com). https://www.azom.com/properties.aspx?ArticleID=863
38. Mahmood M. Shokrieh, Roham Rafiee. Prediction of Young’s modulus of graphene sheets and carbon nanotubes using nanoscale continuum mechanics approach. Materials and Design. Volume 31, Issue 2, February 2010, Pages 790-795.

References

The entire contents of each of the following references is incorporated by reference herein:

39. Duhee Yoon, Young-Woo Son, and Hyeonsik Cheong. Negative Thermal Expansion Coefficient of Graphene Measured by Raman Spectroscopy. Nano Letters 2011 11 (8), 3227-3231
40. http://nguyen.hong.hai.free.fr/EBOOKS/SCIENCE%20AND%20ENGINEERING/MECANIQUE/MATERIAUX/COMPOSITES/Carbon%20Fiber%20Composites/91697_04.pdf 91697_04.pdf (free.fr)
41. Direct measurement of the axial poisson's ratio of single carbon fibres – ScienceDirect. https://www.sciencedirect.com/science/article/abs/pii/026635389190049U#:~:text=Measurements%20on%20three%20types%20of%20carbon%20fibres%20demonstrates,ratio%20takes%20values%20in%20the%20range%200%C2%B726%E2%80%930%C2%B728.%20
42. T700SDataSheet.pdf (rockwestcomposites.com) . https://www.rockwestcomposites.com/media/wysiwyg/T700SDataSheet.pdf
43. Bray JW, Anthony TR (February 1991). "On the thermal conductivity of diamond under changes to its isotopic character". Z. Phys. B. 84 (1): 51–57. Bibcode:1991ZPhyB..84...51B. doi:10.1007/BF01453758.
44. Y.Z.Qiu, A.Witek, D.G.Onn, T.R.Anthony, W.F.Banholzer. Thermal conductivity of natural and synthetic diamonds with differing isotope contents. Thermochimica Acta. Volume 218, 3 May 1993, Pages 257-268
45. Griffiths, David. Introduction to Electromagnetics, Cambridge University Press, 2017.
46. Woodson, Herbert H., and James R. Melcher. Electromechanical Dynamics. 3 vols. (Massachusetts Institute of Technology: MIT OpenCourseWare). http://ocw.mit.edu. License: Creative Commons Attribution-NonCommercial-Share Alike.
47. https://www.engineeringtoolbox.com/stress-rotation-disc-ring-body-d_1752.html
48. (15) (PDF) Adhesion Measurement of Thin Films and Coatings: Relevance to Microelectronics. (researchgate.net). https://www.researchgate.net/publication/287246951_Adhesion_Measurement_of_Thin_Films_and_Coatings_Relevance_to_Microelectronics
49. Adhesion at Diamond /Metal Interfaces: A Density Functional Theory Study (core.ac.uk). https://core.ac.uk/download/pdf/217674361.pdf
50. I.I. GAB, V.S. ZHURAVLEV, D.I. KURKOVA, T.V. STETSYUK, Y.V. NAIDICH. METAL-TO-SAPPHIRE BRAZED AND DIFFUSION BONDED WINDOWS FOR OPTICS, ULTRA-HIGH VACUUM TECHNICS AND ELECTRONICS FOR MAINTENANCE . Institute for Problems of Materials Science of National Academy of Sciences of Ukraine 3, Krzhyzhanovsky str., 252680, Kiev – 180, Ukraine
51. Diffusion Bonding Metals to Ceramics (cjt-limited.com). https://www.cjt-limited.com/diffusion-bonding-metals-to-ceramics